

**VARIABLE DENSITY MUNITIONS BEHAVIOR AND MORPHODYNAMICS
IN THE NEARSHORE**

by

Temitope Ezekiel Idowu

A dissertation submitted to the Faculty of the University of Delaware in partial fulfillment of the requirements for the degree of Doctor of Philosophy in Civil Engineering

Winter 2025

© 2025 Temitope Ezekiel Idowu
All Rights Reserved

**VARIABLE DENSITY MUNITIONS BEHAVIOR AND MORPHODYNAMICS
IN THE NEARSHORE**

by

Temitope Ezekiel Idowu

Approved:

Jack Puleo, Ph.D.

Chair of the Department of Civil, Construction, and Environmental
Engineering

Approved:

Jamie Phillips, Ph.D.

Interim Dean of the College of Engineering

Approved:

Louis F. Rossi, Ph.D.

Vice Provost for Graduate and Professional Education and
Dean of the Graduate College

I certify that I have read this dissertation and that in my opinion it meets the academic and professional standard required by the University as a dissertation for the degree of Doctor of Philosophy.

Signed:

Jack A. Puleo, Ph.D.
Professor in charge of dissertation

I certify that I have read this dissertation and that in my opinion it meets the academic and professional standard required by the University as a dissertation for the degree of Doctor of Philosophy.

Signed:

Nobuhisa Kobayashi, Ph.D.
Member of dissertation committee

I certify that I have read this dissertation and that in my opinion it meets the academic and professional standard required by the University as a dissertation for the degree of Doctor of Philosophy.

Signed:

Tian-Jian Hsu, Ph.D.
Member of dissertation committee

I certify that I have read this dissertation and that in my opinion it meets the academic and professional standard required by the University as a dissertation for the degree of Doctor of Philosophy.

Signed:

Jacob Stolle, Ph.D.
Member of dissertation committee

ACKNOWLEDGMENTS

First and foremost, I would like to express my heartfelt gratitude to God Almighty for His infinite mercy and grace throughout this academic journey.

I extend my deepest appreciation to Jack Puleo, my Ph.D. advisor, for believing in me and providing me with the opportunity and platform to pursue my doctoral studies through this unique and impactful research project. It has been a tremendous privilege to be part of the team, creating memories that many other Ph.D. students can only dream of. Jack is not only an exceptional professor but also an extraordinary mentor. His passion, dedication, expertise, and patience with students are truly inspiring. I feel fortunate to have had him as my advisor and mentor.

I am also deeply grateful to the other members of my supervisory committee—Nobu Kobayashi, Tian-Jian (Tom) Hsu, and Jacob Stolle—for their expert guidance and valuable contributions to my academic and research development.

A special thank you goes to my two core team members on the project, Dr. Manoj Gangadharan and Emily Chapman, for their incredible synergy and team spirit throughout this journey. It was an honor to collaborate with such talented individuals.

I extend my heartfelt gratitude to all my friends and colleagues at the Center for Applied Coastal Research (CACR). The past four years would not have been as enjoyable and fulfilling without your support, camaraderie, and friendship.

I also deeply appreciate the larger University of Delaware (UD) community and the various organizations and platforms I had the privilege to be a part of, including UD-AWRA, CCEGSA, RCCGPH, Project Brainlight, ASBPA SNP,

among others. These experiences significantly enriched my Ph.D. journey and contributed to my personal and professional growth.

I extend my heartfelt gratitude to the staff and colleagues at the Environmental Hydraulics Laboratory, Institut national de la recherche scientifique, Quebec, Canada, as well as the visiting students and researchers from various universities in the USA, Canada, and Mexico for their invaluable contributions to the success of our experimental campaign in the summer of 2022. My sincere thanks also go to the Strategic Environmental Research and Development Program (SERDP) for funding this research project.

Words cannot fully express my appreciation for my wife, Adeola. She was as deeply invested in this Ph.D. journey as I was. Thank you for being an incredible wife and an amazing mother to our son, Toluwanimi.

Finally, as the African proverb says, “It takes a village to raise a child.” Indeed, I am a product of a vast and unwavering support system. To my wonderful parents and sister, thank you for your steadfast encouragement at every stage of my career and academic journey—I could not have achieved this without you. To my uncles, whose inspiration has been a constant source of motivation, and my professional mentors, who have believed in my potential and whose words have consistently propelled me forward, I am eternally grateful.

TABLE OF CONTENTS

LIST OF TABLES	ix
LIST OF FIGURES	x
ABSTRACT	xiv
Chapter	
1 INTRODUCTION	1
1.1 Research Background	1
1.2 Research Objectives	3
1.3 Significance of the Study	4
1.4 Structure of the Dissertation	5
2 LITERATURE REVIEW	7
2.1 The Nearshore Environment and Morphodynamics	7
2.2 Nearshore Morphodynamics and Munitions Behavior	9
2.3 Impacts of the Environment on Munitions Bulk Density	11
2.4 Prior Studies on Munitions Behavior and Knowledge Gaps	13
3 METHODODOLOGY	15
3.1 Introduction	15
3.2 Experimental Design	15
3.2.1 Wave flume	15
3.2.2 Beach morphology	17
3.2.3 Beach hydrodynamics	18
3.2.4 Dimensionless numbers describing the experimental set-up	21
3.3 Instrumentation	23
3.3.1 Vector (V)	24
3.3.2 Vectrino II (VECT)	25
3.3.3 Electromagnetic current meter (EMCM)	26
3.3.4 Ultrasonic Distance Meters (UDM)	27
3.3.5 The real-time kinetic global positioning system (RTK GPS)	28

3.3.6	The echosounder D710U sonar	29
3.3.7	Trimble S5 total station	30
3.4	Surrogate Munitions and Canonical Objects	31
3.4.1	Inertia Motion Units	34
3.4.2	Dimensionless parameters related to munitions/objects migration and burial.	35
3.5	Procedures and Protocols	36
3.5.1	Wave flume setup	36
3.5.2	Experimental steps.....	37
3.6	Data Collection Methods and Analysis Techniques.....	46
3.6.1	Sensors.....	46
3.6.1.1	Time series synchronization of sensors data	48
3.6.1.2	Data cleaning	49
3.6.2	Munitions migration	51
3.6.3	Munitions burial	51
3.6.4	Munitions data table	52
4	BEACH PROFILE MORPHODYNAMICS UNDER VARIED FORCING CONDITIONS.....	53
4.1	Hydrodynamics under the hydrographs.....	53
4.2	Morphological responses to the hydrodynamics under the hydrographs	57
5	MUNITIONS MIGRATION IN RESPONSE TO THE VARIED FORCING CONDITIONS.....	61
5.1	Introduction	61
5.2	Bulk description of variable density munitions migration response to the controlled forcing conditions.....	61
5.2.1	Munitions migration across the entire cross-shore	62
5.2.2	Munitions migration in the offshore zone	65
5.2.3	Munitions migration in the surf zone	68
5.2.4	Munitions migration in the swash zone.....	71
5.3	Dimensionless numbers and power-law relationships	76
5.4	Near-instantaneous migration observations in the surf zone.....	81

5.4.1	Initiation of motion.....	81
5.4.2	IMU-derived near-instantaneous munition migration	82
5.5	Influence of munitions shape and initial orientation on migration.....	89
5.5.1	Station 8 (shape)	90
5.5.2	Station 9 (Shape & orientation).....	92
5.5.3	Station 10 (Shape & initial orientation).....	94
6	MUNITIONS BURIAL IN RESPONSE TO THE VARIED FORCING CONDITIONS.....	97
6.1	Introduction	97
6.2	Bulk description of munitions burial in the nearshore in response to the controlled forcing conditions.....	98
6.3	Morphodynamics and munitions burial/exposure	101
6.4	Dimensionless numbers and empirical relationships	104
7	DISCUSSION AND CONCLUSION	106
7.1	Discussion.....	106
7.1.1	Migration	106
7.1.2	Burial	109
7.2	Limitations and future work	110
7.3	Conclusion.....	112
	REFERENCES	114
	Appendix	
A	DESCRIPTION OF TERMS IN THE AGGREGATED MUNITIONS TABLE	123

LIST OF TABLES

Table 3.1: Hydrodynamics characteristics for the different hydrographs	19
Table 3.2: Dimensionless parameters considered for describing the model	21
Table 3.3: Relevant deployed sensors in the study	24
Table 3.4: Dimensionless numbers associated with munitions behavior	36
Table 3.5: Munitions deployments by stations	39
Table 4.1: Sensors look-up table	53
Table 5.1: “No motion” and “motion” values and percentages based on the <i>SG</i> ranges.....	63
Table 5.2: “No motion” and “motion” values and percentages based on the <i>SG</i> ranges and cases (offshore).	66
Table 5.3: “No motion and “motion” values and percentages based on the (a) <i>SG</i> ranges and (b) cases (surf).....	70
Table 5.4: “No motion and “motion” values and percentages based on the <i>SG</i> ranges (swash).	74
Table 5.5: Duration of time before initiation of motion due to the wave forcing relative to $t = 0$ s, the wave maker start time.....	81
Table 5.6: Computed hydrodynamic parameters during each section of the migration.	86

LIST OF FIGURES

Figure 1.1: Chemical weapons dumping sites globally (Wilkinson, 2017)	2
Figure 2.1: Schematic of the nearshore showing the offshore, surf and swash zone regions. The swash zone is exaggerated.....	8
Figure 2.2: Time-reliant corrosion, encrustation, and biofouling processes on an aluminum cylinder, plated steel, and bare steel over 3 years. (a) Installed in Lewes, Delaware at Marine Ops on 12/13/2020; (b) retrieved on 12/08/2023.....	12
Figure 3.1: Overhead view of the INRS wave flume looking in the offshore direction from the beach face (LHE-INRS, 2024).	16
Figure 3.2: The offshore H_s , T_p and still water depth (SWD) of the six hydrographs. The markers are the discretized trials contained in each hydrograph (Case).	20
Figure 3.3: Schematic of the wave flume and the deployed sensors.....	23
Figure 3.4: Nortek Vector	25
Figure 3.5: Nortek vectrino II.....	26
Figure 3.6: The Valeport Electromagnetic current meter.....	27
Figure 3.7: The PulStar Series M-300 ultrasonic distance meter by MassaSonic	27
Figure 3.8: The Leica RTK GPS system	28
Figure 3.9: echosounder D710U sonar from EchoLogger (source: https://www.aditech-uw.com/en/shop/6491-echologger-eth-d710u.html)	29
Figure 3.10: Trimble S5 total station.....	30
Figure 3.11: Variable density munitions and canonical objects deployed, L is the object length, and '*' indicates the number of objects of a specific type deployed.	32

Figure 3.12: Distribution of the munitions deployed based on their specific gravity values.....	33
Figure 3.13: Inertia Motion Unit and a sample R81 munition showing where the IMU is inserted.....	35
Figure 3.14: Experimental steps	38
Figure 3.15: Munitions deployment layout in the wave flume	43
Figure 3.16: Measuring points of the munitions	44
Figure 3.17: Measuring munitions burial	45
Figure 4.1: Time series of the velocity sensors from the offshore zone to the beach face	54
Figure 4.2: Time series excerpts of water depth (h) and cross-shore velocity (u) for the first 100 s of the largest forcing conditions (Case03, Trial 01) in the offshore (a,b), surf (c,d), and swash (e,f) zones.	55
Figure 4.3: Cross-shore distribution of <i>Hrms</i> (a–f) and <i>Urms</i> (g–l) for all Cases..	56
Figure 4.4: The beach slope is gentler at about 1:20 from the flat section to $x = 72$ m and steeper at about 1:5 between $x = 72$ to $x = 87$ m of the scaled profile. Overall, the foreshore profile is relatively steep at about 1:14... 58	
Figure 4.5: Changes in the beach profile elevation relative to the pre-trial elevation.	59
Figure 5.1: Migration distances for munitions in the nearshore; (a) no motion; (b) motion.....	64
Figure 5.2: Migration distances for munitions in the offshore zone. The left and right are the “no motion” and “motion” data, respectively.	66
Figure 5.3: Migration distances for munitions in the offshore zone separated into cases. The top and bottom rows are the “no motion” and “motion” data for each case, respectively.	67
Figure 5.4: Migration distances for munitions in the surf zone. The left and right are the “no motion” and “motion” data, respectively.....	69

Figure 5.5: Migration distances for munitions in the surf zone separated into cases. The top and bottom rows are the “no motion” and “motion” data for each case, respectively.	71
Figure 5.6: Migration distances for munitions in the swash zone. The left and right are the “no motion” and “motion” data, respectively.....	73
Figure 5.7: Migration distances for munitions in the swash zone separated into cases. The top and bottom rows are the “no motion” and “motion” data for each case, respectively.	74
Figure 5.8: Migration as a function of Shields number for all motion observations. Positive and negative values represent onshore- and offshore-directed migrations, respectively. The symbol shapes represent the Cases. Case01 to Case06 are \circ , \square , \triangleright , \triangleleft , ∇ , Δ , respectively.	77
Figure 5.9: Power law fit of (a) $ dx $ versus θ and (b) Migration versus θm in the swash zone.....	78
Figure 5.10: Power law fit of (a) $ dx $ versus θ, SG and (b) $ dx $ versus $\theta m, SG$ in the swash zone.....	80
Figure 5.11: (a,b) The migration time history of an R81 ($SG = 2.5$) instrumented surrogate munition in the surf zone. Offshore migration is from right to left. The color changes depict the sectioning of the munition migration trajectory. The corresponding-colored circles indicate the start of each migration section. (b) The beach profile for reference. (c–j) Free surface oscillations (η) 60 s before and after the onset of the S1 to S8 centered around a local RTt = 0 s. The colors correspond with the colors used for S1 to S8 in Figure 5.11a.	84
Figure 5.12: Migration distance as a function of observation of a 81 mm projectile with $SG = 2.5$ (R81), $SG = 3.0$ (M81), and $SG = 4.18$ (S81), (a) net migration, (b) gross migration, and (c) duration of the migration expressed in (a). Color coding is relative to Figure 3.11.	88
Figure 5.13: The cross-shore locations of stations 8, 9, and 10 in the surf zone of the wave flume.	89

Figure 5.14: Munitions deployed at the three stations, Station 8) $x = 52$ m focuses on the influence of shape on migration by comparing cylinders and Rockets; Station 9) $x = 57$ m focuses on the influence of shape and initial orientation on migration by comparing cylinders and spheres; and Station 10) $x = 62$ m focuses on the influence of shape and initial orientation on migration by comparing surrogate 81 projectiles with noses, without noses, and without tails	90
Figure 5.15: The munition pairs versus their net migration at the end of each case from case01 to case06 at station 8.....	92
Figure 5.16: The munition pairs versus their net migration at the end of each case from Case01 to Case06 at station 9. SP = spanwise and ST = streamwise.	93
Figure 5.17: The munition pairs versus their net migration at the end of each case from case01 to case06 at station 10. SP = spanwise and ST = streamwise.	94
Figure 5.18: Migration dynamics of two 81 mm projectile types, (a) is the flat headed 81 mm projectile with a fin-like base and, (b) the fin-less 81 mm projectile.....	95
Figure 6.1: The BD against the number of observations. The bin sizes are 0.1.....	99
Figure 6.2: The BD against the number of observations in the (a) offshore, (b) surf, and (c) swash zones.....	100
Figure 6.3: a-c) Dimensionless relative burial depth change versus relative profile change for the offshore (a), surf (b), and swash zones (c). The symbols represent the Cases. Case01 to Case06 are $\circ, \square, \triangleright, \triangleleft, \nabla, \Delta$, respectively.....	103
Figure 6.4: Relative burial depth as a function of KC (a) and θ (b).....	105

ABSTRACT

A quantitative understanding of the migration of munitions and canonical objects in the nearshore is needed for the effective management of contaminated sites. Migrations of munitions with a density range of 2000 kg/m^3 to 5720 kg/m^3 were quantified in a large-scale wave flume. The forcing consisted of six hydrographs of varying wave heights, periods, still water depths, and durations. The cross-shore profile, typical of natural sandy beaches, was sub-divided into swash, surf, and offshore zones. The outputs of the study represent what is believed to be the largest dataset on object migration spanning simultaneously the swash, surf, and offshore zones of the nearshore.

Overall, 2228 migration measurements were recorded with 16% and 84% of the migration observations classified as “motion” (net distance $> 0.5 \text{ m}$) and “no motion” (net distance $\leq 0.5 \text{ m}$), respectively. The probability of munitions migration increased with proximity to the shoreline. There was a nearly equal probability of onshore or offshore migration in the swash zone. Migration in the surf zone tended to be offshore-directed (65%), while migration was onshore-dominant (65%) in the offshore zone. Migration in the offshore zone was preferentially onshore due to skewed waves over flat bathymetry. Less dense munitions in the offshore zone may have migrated offshore likely still related to the skewed nature of the wave profile causing transport in both directions through the majority of the wave phase. The largest migration distances occurred in the surf zone likely due to downslope gravity. Migration in the surf and swash zones is a balance between skewed/asymmetric

forcing and downslope gravity, with downslope gravity tending to be pronounced provided the forcing is sufficient to initiate motion. An exception was sometimes observed in the swash zone where onshore forcing was sufficient to transport munitions to the seaward side of the berm where they became trapped in a bathymetric depression between the dune and berm. Relating overall migration (Lagrangian) to fixed hydrodynamic measurements (Eulerian) was ineffective.

A total of 1645 burial observations were recorded. Most initially proud munitions (87%) were either partially buried or at most became fully buried just below the surface. No clear trends were observed between munitions bulk density and burial. Munitions burial in the swash and surf zones resulted from near- and far-field processes while burial in the offshore zone was governed more by near-field scour processes.

Parameters such as the Shields number, Keulegan-Carpenter number, Object mobility number, wave skewness, and wave asymmetry estimated from the closest measurement location were insufficient to predict migration and burial. The large scatter in the migration and burial data resulting from competing hydrodynamic, morphodynamic, and munitions response processes makes robust deterministic predictions with flow statistics and dimensionless numbers difficult. Hence, the probability-based approach was more efficient for quantifying munitions behavior in the nearshore.

Chapter 1

INTRODUCTION

1.1 Research Background

Munitions or Unexploded Ordnance (UXO) are ammunitions belonging to a larger family of explosives widely used by the Navy, Army, Air force, and other military organizations. After the major world wars (WWI and WWII), sea disposal of munitions became common practice up until the 1970s when international conventions agreed to end the practice (Carton & Jagusiewicz, 2009). The quantity of munitions present in the oceans remains uncertain due to limited documentation. However, conservative estimates from known records suggest that at least 1.6 million tons of chemical weapons munitions were disposed of in the oceans (Figure 1.1; Wilkinson, 2017). The aftermath of ocean disposal of munitions is a global concern currently impacting over 40 countries (Carton & Jagusiewicz, 2009).



Figure 1.1: Chemical weapons dumping sites globally (Wilkinson, 2017)

In the United States alone, more than 70 chemical weapons and munitions disposal events occurred in coastal waters between 1918 and 1970 (SERDP, 2010). There are more than 10 million acres across over 400 designated sites possibly containing munitions in underwater environments within the Formerly Used Defense Sites program alone (SERDP, 2010; US Army RDECOM, 2001). The reappearance of underwater munitions has occurred in the Gulf of Mexico and along the coastlines of at least 16 states (Randall, 2015). Accounts of UXO appearance in the nearshore after decades underwater (Macdonald et al., 2004) cause public and environmental concern (Parry, 2018).

Early modeling studies on UXO mobility indicate that high energy waves and currents could cause offshore located UXO to experience onshore migration and

exposure (NAVFAC, 2013). Hence, extreme forcings conditions could be major causes of the migration and exposure of UXO in the nearshore. More importantly, quantification of the migration and exposure of the munitions in the nearshore is still poorly understood especially when the densities of the munitions vary. Quantifying the behavior of variable density munitions under near-prototype conditions would help provide further insights into the stochastic behavior of variable density munitions in the nearshore, in the face of the uncertainty in the extremity and frequency of forcing conditions required to cause mobility, burial, and exposure.

1.2 Research Objectives

The objectives of the study were to create more detailed insights into the complex interplay between the bulk density variation, hydrodynamics, and morphodynamics in the mobility and burial of munitions in the nearshore. Most prior studies focused on the deep underwater regions before shoaling begins to occur. Yet, munitions appear on the beach face either by being transported from the offshore regions, exhumed via sediment erosion, or brought onshore as dredged material through the surf and the swash regions to the beach face. Hence, more studies are required to quantify the fate of munitions in the nearshore environment.

The behaviors of variable density munitions under six controlled forcing conditions at different water levels were quantified to address the following:

1. To what extent do hydrodynamics and bulk density impact munitions migration across the offshore, surf, and swash zones? What are the probabilistic migration and burial tendencies of munitions across the three zones?

2. Does hydrodynamics play or more dominant role than munitions bulk density on migration and burial?
3. Does shape play a significant role on munitions migration in the nearshore?
4. Are there quantifiable trends between morphodynamics and munitions burial?

Addressing the above questions involved conducting experiments with surrogate munitions and canonical objects under a near-prototype scale condition. Quantifications from the experiments were used to create bulk statistics between pre- and post-trial measurements to quantify the migration and relative burial of munitions and establish parameterizations that describe the munitions behaviors based on dimensionless numbers. Near-instantaneous measurements were used to establish the initiation of motion of the munitions and their migration tendencies based on their variable density and shapes.

1.3 Significance of the Study

Predicting munitions MBE is difficult due to complex, interrelated processes of hydrodynamics, morphodynamics, grain-scale processes, and the munitions characteristics (Puleo & Calantoni, 2023) Aspects of the complex interactions and force balance on a submerged object have been described mathematically (Chu, 2023; Cristaudo et al., 2023; Rennie et al., 2017; Traykovski & Austin, 2017) but are generally related to the initiation of motion rather than migration distance. Lacking

proper deterministic relationships, empirical and other models have been used to improve Munitions Burial and Exposure (MBE) prediction. However, due to the highly stochastic nature of munitions behavior, comprehensive experimental data are needed for creating data-driven predictions and for validation of coupled probabilistic or computational models (Chu, 2023; Hsu et al., 2020; Liu & Qiu, 2019; Rennie, 2017). The Underwater Munitions Expert System (UnMES; Rennie, 2017), a Bayesian expert system requires a broad data set for training and testing. Limited validation of UnMES has been completed on many processes based on available data but predictive skill was moderate with existing migration distance data especially closer to the shoreline (Palmsten & Penko, 2020; Rennie et al., 2019). The Munitions Response Library (MRL) is a robust community standard repository that aggregates information related to munitions behavior and uses UnMES in a predictive approach (Penko, 2021; Puleo & Calantoni, 2023) currently focusing on depths outside the shoaling zone. More robust data from the shoaling zone landward are needed to train UnMES and enhance the MRL. Ultimately, the data-driven frameworks and repository will form an integral part of the munitions mobility and burial reference manual that aims to translate the science of munitions phenomenology into real-world munitions response site management (Puleo and Calantoni, 2023).

1.4 Structure of the Dissertation

This dissertation uses an experimental approach to quantify the behavior of variable density munitions across three zones in the nearshore from the offshore region over a flat bathymetry to the beach face. Chapter 2 provides a detailed literature review of munitions highlighting past studies, findings and gaps yet to be filled. In Chapter 3 the methodology is described. The methodology consists of the description

of the experimental design and conditions including instrumentations, the overview of the surrogate munitions and canonical objects deployed, experimental procedures and protocol, and the data collection and analysis approach. Chapter 4 describes the data analysis procedures and the results of the hydrodynamics and the beach profile morphodynamics in response to the controlled forcings., Chapters 5 and 6 describe the quantifications of the migration and burial observations, respectively, and their interrelationships with hydrodynamics, morphodynamics, dimensionless numbers, and power-law relationships. The overarching discussions of the findings, limitations, conclusions, and future work are presented in Chapter 7.

As a whole, this dissertation advances the understanding of munitions behavior in the shallower regions of the nearshore namely the surf and swash zones as well as compare the observations in these regions with the deeper offshore region. The findings will ultimately contribute to the broader efforts of sustainably managing the public and environmental impacts of disposed munitions in marine environments.

Chapter 2

LITERATURE REVIEW

2.1 The Nearshore Environment and Morphodynamics

The nearshore is broadly considered as the region extending from the shoreline to a location offshore of the breaking zone (Bralower et al., 2021) and comprises parts of the offshore zone, the swash and surf zones (Figure 2). The offshore zone is loosely described as the seaward region outside of the surf zone, where the wave-induced sediment transport is negligible (Figure 1). The surf and swash zones are distinct zones in the nearshore but are sometimes combined. For instance, Nielsen, (2009) broadly classifies the surf zone into three: 1) outer surf zone, 2) inner surf zone, and 3) swash zone. However, several other studies separate the swash from the surf zones (Elfrink & Baldock, 2002; Masselink & Puleo, 2006; Puleo et al., 2003). The schematic representation of the swash and surf zones (Figure 2) illustrates a simple demarcation between the swash and surf zones in nearshore environments.

The surf zone is distinctly the region extending from the point where the waves break to the edge of the swash zone and is the most dynamic nearshore region (USACE, 2003). The waves tend to be skewed outside the surf zone and asymmetric or skewed asymmetric inside the surf zone (Battjes, 1988). Within the zone, the wave surface profiles possess a relatively steep front and a much gently sloping rear side (Svendsen et al., 1978). The hydrodynamics of the surf zone are governed by the high-frequency wave transformation processes, flow transformation from irrotational motion during wave overturning, steepening, and jet formation into a rotational flow

and into a turbulent bore (Battjes, 1988; Svendsen et al., 1978). The entire process leads to wave energy dissipation accompanied by a decrease in total convective momentum flux (Battjes, 1988).

A general understanding of the swash zone is that it is the temporal region extending from the maximum uprush limit on the beach to the point of bore collapse (Hughes & Turner, 1999). The swash zone is also the region in the nearshore where there is an intermittent wetting and receding of waves at the beach face or where the beach face is intermittently uncovered by water possibly over short and long timescales (Elfrink & Baldock, 2002; Masselink & Puleo, 2006). However, some researchers believe this general understanding of the swash zone is too simplistic and the swash zone is rather the region extending from the intermittently wet and dry portion of the beach face to the point where turbulence starts to impact the seabed (Puleo et al., 2000). Here the swash zone is depicted as the region extending from the edge of the surf zone to the uprush limit on the beach (Figure 2.1).

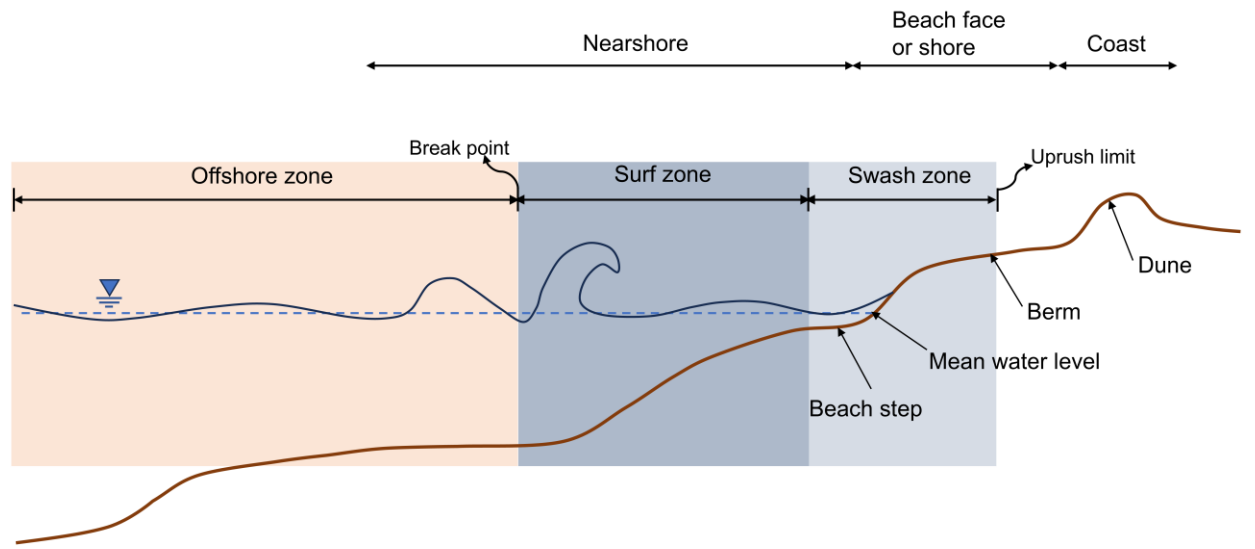


Figure 2.1: Schematic of the nearshore showing the offshore, surf and swash zone regions. The swash zone is exaggerated.

2.2 Nearshore Morphodynamics and Munitions Behavior

Skewed waves from the offshore zone propagate towards the shoreline and shoal until breaking occurs. Following the collapse of the bore in the landward region of the surf zone, uprush motion is influenced by gravity and bed friction, with these two processes acting in opposition to the flow direction. The leading edge of the uprush motion eventually slows to a halt on the beach face. Subsequently, the fluid accelerates downslope during the backwash phase, where flow is once again governed by gravity and friction, both working against each other. Ultimately, the backwash flow decelerates as the fluid thins significantly, with friction surpassing gravitational forces.

Flows within the swash zone do not follow strict oscillatory patterns. Rather, they comprise distinct phases of onshore-directed and offshore-directed flows. Velocity magnitudes may reach values exceeding 3 m/s when transitioning from shallow or nonexistent depths to depths of over 1 m (Chardón-maldonado et al., 2016). Hydrodynamics acting on a mobile bed result in sediment transport when the initiation of motion criterion is surpassed. Bed shear stresses and pressure gradients within the surf and swash zones frequently reach levels that are adequate to initiate the movement of sediment (Masselink & Puleo, 2006). Gradients in sediment transport, both cross-shore and alongshore, result in bed elevation changes through sediment continuity.. On beaches, the most evident expressions of morphodynamics are the appearance and disappearance of sandbars and berms. The sandbars and berms are dynamic, as they can quickly erode or accrete and migrate either toward or away from the shore (Wright & Short, 1984). The phenomenon demonstrates the complex interplay between hydrodynamics and morphodynamics where the wave conditions impact the bed, and the changes in the bed levels impact wave transformation.

Objects within coastal regions can be categorized as large or small, depending on the diffraction parameter (ka) defined as the ratio of the relative size, commonly quantified by cross-sectional diameter (D), of the object to the wavelength (Chakrabarti, 1998). When the value of ka is greater than 0.5, the incident waves on the object experience diffraction and fluid flow is modified (Chakrabarti, 1998). Hence, the hydrodynamic forcing acting on large objects is inertia-dominated and they modify the far-field flow field. Conversely, objects are considered small when ($ka < 0.5$) and therefore do not cause wave diffraction on the surface or modify far-field flow (Chakrabarti, 1998). Hence, inertia is negligible and drag is dominant in small objects. Cobbles, cylinders, conical frusta, and munitions (in the range of $D = 20$ mm – 155 mm) under typical coastal forcing are all considered small objects.

Morphodynamics are relevant to Munitions Burial and Exposure (MBE) studies because energetic conditions can lead to the burial or, more critically, the exposure of solid objects, subjecting the previously buried ones to active hydrodynamics. Like sediments, munitions also have specific initiation of motion criteria (Rennie et al., 2017) and physical/empirical relationships that should govern their migration and burial (Cristaldo et al., 2023; Friedrichs et al., 2016). However, these criteria and laws are not fully defined, thereby posing challenges in developing munitions predictive models and tools for site managers.

Morphodynamics can cause the munitions to advance either offshore or onshore and hence may be transported to the beach/shoreline. Over relatively large temporal scales, or under shoreward-driven extreme events, munitions may experience relatively large onshore net migration and become exposed on the shoreline/beach from deeper underwater environments. For instance, munitions have appeared after

storm events or were brought onshore as dredged material: outer banks of North Carolina after Hurricane Maria (Breslin, 2017; Geib, 2018), Mantoloking beach during beach nourishment to reverse the damage caused by Hurricane Sandy more than five years later (Parry, 2018). Bed characteristics around the objects, the physical properties of the object (such as bulk density, dimensions, shape, surface roughness), the object's relative orientation to the flow direction, and the surrounding flow characteristics impact the migration and burial of the objects. The complex interactions and force balance on the objects are well described in the literature in deeper underwater environments (Rennie et al., 2017) and in swash environments where objects are intermittently submerged (Cristaldo et al., 2023).

2.3 Impacts of the Environment on Munitions Bulk Density

Variation in bulk density may be caused by diverse reasons such as numerous iterations of the same munition type (MR-2320), corrosion, perforation, biofouling (Steinhurst et al., 2017), and encrustation (George et al., 2015) processes. The corrosion processes can remove 0.18 - 0.58 mm/yr of material (Melchers and Jeffrey, 2005; Porte, 1967; Sugiyama et al., 2004). These processes impacting the bulk density of munitions (except the numerous iterations of the same munition type) are time-dependent environmental processes that can occur to munitions situated in marine environments. They can also alter the geometry and the surface roughness characteristics of the munitions over time.

The authors demonstrated the time-dependent environmental impacts on munitions bulk density through the deployment of a cluster of aluminum cylinders, bare steel, and plated steel at three levels in the water column in a marine basin site. The three levels in the water column were the seabed, the mid-water column, and just

below the water surface. Figure 3 depicts the corrosion and biofouling processes that occur on munitions in underwater marine environments over time. Although seasonal changes were observed to impact the changes with more biofouling experienced in the summer months, an upward trend was observed in the mass increase of the munitions. As high as 113%, 92%, and 40% increase in mass due to biofouling were observed in plated steel, aluminum, and bare steel, respectively, in the mid-water column where biological activity was greatest. At the seabed, 55% and 14% increase in mass were observed in the aluminum and plated steel likely due to biofouling and encrustation, and a 9% decrease in bare steel due to corrosion.



Figure 2.2: Time-reliant corrosion, encrustation, and biofouling processes on an aluminum cylinder, plated steel, and bare steel over 3 years. (a) Installed in Lewes, Delaware at Marine Ops on 12/13/2020; (b) retrieved on 12/08/2023.

The bulk density values of the munitions have been observed to be a determining driver of the dominant process between munitions burial and/or migration i.e., above certain threshold bulk density values, the munitions tend to bury rather than migrate (Calantoni, 2018). However, this threshold for burial/migration dominance requires further study.

2.4 Prior Studies on Munitions Behavior and Knowledge Gaps

Prior studies have shown that local forcing and bulk density are primary parameters in determining the mobility and burial characteristics of munitions (Catano-Lopera and Garcia, 2006; Friedrichs et al., 2016; Rennie et al., 2017). However, bulk density of the existing studies on objects migration and burial/exposure in the nearshore focused on deeper underwater environments (Calantoni et al., 2014; Garcia & Landry, 2018; Rennie et al., 2017), energetic surf zones, and shoaling zones (Bruder et al., 2018; Traykovski & Austin, 2017; Voropayev et al., 2003b) and few studies have focused on the beach face where swash processes occur (Cristaldo & Puleo, 2020; Luccio et al., 1998). The cross-shore displacement of cobbles with varying sizes, shapes, and bulk densities has been quantified by studying the motion of cobbles in the swash zone under dam-break laboratory conditions (Luccio et al., 1998). Similar and more recent dam-break studies of object migration are; the observations of the migration of spherical munitions in the swash zone of a permeable mobile bed (Gross, 2019), a double dam-break study on the swash observations of migration, exposure and burial of tapered munitions under mixed grain (sand, gravel, and cobble) bed (Wengrove & Garcia-Medina, 2022) and a double dam break study on tapered variable density munitions where the variations in density were assumed to be due to biofouling and encrustation processes (Idowu et al., 2022). The dam-break

studies highlight and provide quantifications on the impacts of tsunami-like extreme solitary wave-forcing conditions on munitions migration and burial in the swash zone. However, the number of objects/munitions studies focused on the surf and swash zone under random waves and/or currents are still relatively few due to the complexities associated with the intermittent submergence of the beach on time scales of seconds to hours experienced in these zones. The intermittency exacerbates sampling difficulties, especially considering the potential for rapid morphological change and munitions mobility, exposure, and burial. Few studies have quantified objects tracking in the swash and surf zone; gravel and microplastics (Laksanalamai & Kobayashi, 2023), cobbles in the swash zone (Luccio et al., 1998), munitions in energetic surf zones (Traykovski & Jaffre, 2020) and munitions in the surf and swash zones (Cristaldo & Puleo, 2020). Yet, there is a need for studies on the burial and mobility of munition in these surf and swash regions (Calantoni, 2014) to help fill the knowledge gaps in the parameter space in the region.

Hence, the overarching objective of this study is to investigate the role of bulk density variations in munitions and how the different cross-shore zones and the associated morphodynamics impact munitions' cross-shore migration and burial in the nearshore.

Chapter 3

METHODOLOGY

3.1 Introduction

This study involved a series of experiments conducted in a near-prototype scale wave flume which captured morphodynamics, the munitions migration, and burial/exposure measurements under different forcing conditions. Chapter 3 focuses on the adopted methodology, encompassing the experimental design, the materials and instrumentations, the experimental procedures and protocols, and the data collection methods and analysis techniques.

3.2 Experimental Design

The experiment was conducted in a large-scale wave flume (Figure 3.1) with a beach profile typical of natural sandy beaches.

3.2.1 Wave flume

The large-scale wave flume is 120 m long, 5 m deep, and 5 m wide, managed by the Environmental Hydraulics Laboratory, *Institut National de la Recherche Scientifique* (INRS), Quebec, Canada (Figure 3.1). The piston-type wave paddle with active absorption has a maximum stroke length of 4 m and 4 m/s maximum velocity. Wave flume water depth and wave period ranges of 2.5 – 3.5 m and 3 – 10 s, respectively, are possible (LHE, 2021). The wave flume has a water transfer system connected to a reservoir with a capacity of 3500 m³.



Figure 3.1: Overhead view of the INRS wave flume looking in the offshore direction from the beach face (LHE-INRS, 2024).

The cross-shore coordinate (x) in the wave flume increases onshore starting at $x = 0$ at the at-rest position of the wave paddle located at the far end in the building as shown in Figure 3.1. The spanwise coordinate (y) increases from $y = 0$ at the right wall for an observer looking onshore (a right-handed coordinate system). The vertical coordinate (z) increases from the $z = 0$ at the bottom of the flume. Along the right wall from $x = 32$ m to $x = 97$ m, are stations spaced 5 m apart equipped with vertical pipes for placement of sensors measuring different aspects of the hydrodynamics and morphodynamics.

3.2.2 Beach morphology

Important aspects of the beach morphology are the beach profile and the sediment grain sizes. The beach profile often experiences temporal changes both in the cross-shore and alongshore directions on the same beach system. An equilibrium beach profile is often used to create a representative beach profile for a particular coastal location but even that changes with the seasons (Bosboom & Stive, 2021). The initial beach profile used for this study is a near-prototype scale beach profile of Mantoloking Beach located in Ocean County, New Jersey USA pre–Hurricane Sandy (Pontiki et al., 2023; Tsai et al., 2024). A scale of 2.31 based on Froude scaling presented in (Van Rijn et al., 2011) was applied to obtain the flume-scale beach profile. The beach profile was chosen because it is representative of typical sandy beach profiles.

The typical median grain size (d_{50}) of sandy beaches ranges between 0.2 mm and 2.0 mm, depending on a variety of factors including the sediment source, wave energy, and coastal geomorphology like slope (Komar, 1998). The d_{50} values on sandy beaches vary along the cross-shore zone, with d_{50} values decreasing from the breaking zone to the backshore with the sediment on the foreshore and backshore being better sorted than those further offshore in the breaker zone (Edwards, 2001). The progressive decrease in d_{50} can be attributed to a reduction in swash intensity towards the shoreline and the widest sediment grading is observed where energy dissipation occurs the most (Osborne, 2019). Based on availability and feasibility, the sediment with a median grain size (d_{50}) of 0.28 mm obtained from a nearby quarry was used for the experiment which falls within the between 0.2 mm and 2.0 mm typical range for sandy beaches. The other properties of the sediment include a

specific gravity value of 2.65, and the sorting, skewness, and kurtosis values of 1.65, 0.23, and 1.30, respectively.

The scaled beach profile was constructed in the wave flume (Figure 3.3). The $x = 7$ m to $x = 52$ m is the region characterized by a relatively flat bathymetry of 0.5 m depth of sand for a smoother transition from the concrete flume bottom to the mobile bed of the actual profile. The 60 m region from $x = 52$ m to $x = 112$ m comprised the nearshore region with varying local slopes towards the dune. The beach slope is gentler at about 1:20 from the flat section to $x = 72$ m and steeper at about 1:5 between $x = 77$ and $x = 87$ m of the scaled profile. Overall, the foreshore profile is relatively steep at about 1:14 (Figure 3.3).

3.2.3 Beach hydrodynamics

The experiment aimed to create forcing conditions that provided the greatest chance for munitions migration. Hence, different forcing combinations were designed based on unique characteristics and the capacity of the wave flume. A segment of the Hurricane Sandy event from October 29 - 30, 2012 was used as a guide. The peak significant wave height (H_s) and peak wave period (T_p) of the event segment were 2.74 m and 12.49 s, respectively, obtained from WAVEWATCH III (NOAA, 2019; WW3DG, 2016 at 40.12° N, 74.00° W. It is noted that the aim was not to reproduce Hurricane forcing. Instead, nearshore wave data following the event were used to provide forcing estimates rather than selecting forcing conditions without real-world context.

The experiment consisted of six hydrographs (cases) discretized into 5 trials each except for Case05 which contained 10 trials. The durations, still water depths, peak wave periods (T_p), and significant wave heights (H_s) of the hydrographs (cases)

are presented in Table 3.1. The discretization was such that the hydrodynamic conditions (durations, H_s , T_p , still water depth) of each hydrograph were ramped up from the first to the last trial. The minimum and maximum values of H_s , T_p , and still water depths were 0.21–1.4 m, 2.5–12 s, and 2.1–3.3 m, respectively. Three hundred irregular waves were forced in each trial using a TMA spectrum (Hughes, 1984).

Table 3.1: Hydrodynamics characteristics for the different hydrographs.

Case Number	Number of Trials	Still Water Depth (m)	Significant Wave Height H_s (m)	Wave Period T_p (s)	Duration (hr)
01	5	2.1	0.72	7.11	0.59
02	5	2.87	1.1	6	0.50
03	5	3.3	1.4	6	0.50
04	5	2.23–2.87 Increment: 0.15–0.17	0.21–1.1 Increment: 0.22–0.23	2.54–5.99 Increment: 0.84–0.86	0.21–0.50 Increment: 0.07–0.08
05	10	2.24–2.87 Increment: 0.6	0.21–1.1 Increment: 0.09–0.1	2.54–5.99 Increment: 0.38–0.39	0.21–0.50 Increment: 0.03–0.04
06	5	2.23–2.87 Increment: 0.15–0.17	0.6	8–12 Increment: 1	0.67–1.00 Increment: 0.08–0.09

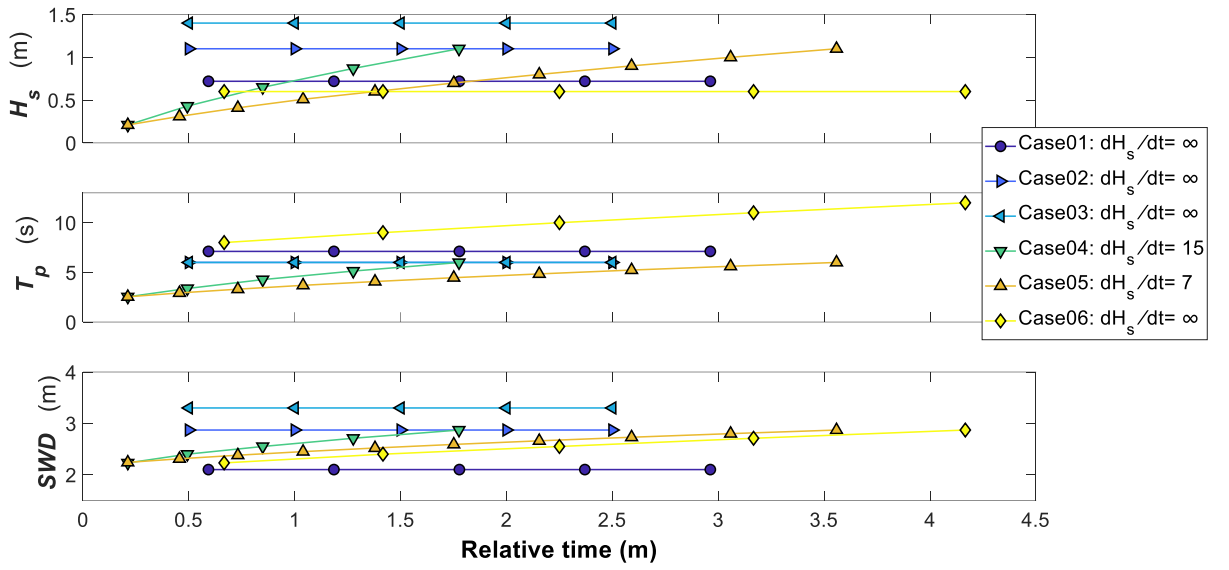


Figure 3.2: The offshore H_s , T_p and still water depth (SWD) of the six hydrographs.

The markers are the discretized trials contained in each hydrograph (Case).

Case01 to Case03 had increasing still water depths and H_s , and a wave onset $dH_s/dt = \infty$; where dt is the time increment between the H_s values of two successive trials, meaning the largest waves were forced from the first trial on. Case04 and Case05 maximized H_s as still water depths increased with each trial. However, Case04 had a faster wave onset, $dH_s/dt = 15$ with 5 trials to reach the maximum H_s , while Case05 had a slower wave onset with $dH_s/dt = 7$ over 10 trials. Case06 focused on maximizing the wave period while maintaining a still water depth increase similar to Case04 but with a $dH_s/dt = \infty$.

3.2.4 Dimensionless numbers describing the experimental set-up

The experiment is designed to model morphodynamics under energetic conditions and the motion and burial of objects on a mobile bed. The physics of such models can be characterized by several dimensionless parameters (Kamphuis, 2018; Dean and Dalrymple, 2010; Grasso et al., 2009): Froude (Fr), Dean (Ω), Iribarren (ξ), Rouse (Rou), Shields (θ), and Reynolds numbers (Re). Table 3.2 provides a brief description of the dimensionless numbers, the equations, and values obtained for the experimental condition. The Dimensionless numbers were computed using the peak hydrodynamic values described in section 3.2.3, scaled using the 2.31 scale parameter applied for the morphology in section 3.2.2.

Table 3.2: Dimensionless parameters considered for describing the model.

Dimensionless Parameter	Brief Description	Equation	Values
Froude (Fr)	The ratio of inertial to gravitational forces. Determines if a flow is super or subcritical	$Fr = \frac{H_s \sigma_p}{2\sqrt{gh}}$ where $\sigma_p = \frac{2\pi}{T_p}$ is the angular frequency.	0.1
Dean (Ω)	Suspension parameter. Describes wave-breaking conditions in the surf zone	$\Omega = \frac{H_s}{T_p w_s}$ where w_s is the fall velocity.	2.6
Iribarren (ξ)	Surf similarity parameter.	$\xi = \frac{\tan \beta}{\sqrt{\frac{H_s}{L_\infty}}}$ where $\tan \beta$ is the local beach slope, L_∞ is the deep-water wavelength.	0.38
Rouse (Rou)	The ratio of a turbulent timescale to a settling time scale. Identifies the mode of sediment transport.	$Rou = \frac{w_s}{u'}$ where $u' = \kappa \sqrt{f_w/2} A \sigma_p$, $\kappa = 0.4$ (Von Karman constant), and f_w is a wave friction factor	2.45
Shields (θ)	Determines the transport regime (bedload, suspension, sheet flow) and incipient motion.	$\theta = \frac{\tau_b}{(\rho_s - \rho_w) g d_{50}}$ where bed shear stress $\tau_b = \frac{1}{2} \rho_w f u^2$ and f = friction factor.	0.82
Reynolds (Re)	The ratio of inertial to viscous forces.	$Re = \frac{A \sigma_p h}{v}$	1.81×10^6

	where $A = \frac{H_{rms}}{2\sinh \sinh kh}$, $H_{rms} = H_s / \sqrt{2}$ and ν is the kinematic viscosity.	
--	--	--

The Fr is the primary requirement for wave-driven physical models (Dean and Dalrymple, 2010). The Ω is widely known as an important parameter for the modal classification of cross-shore beach profiles into dissipative, intermediate, or reflective beaches (Grasso et al., 2009). The ξ which is the ratio of the local beach slope and the deep-water steepness is needed for understanding the breaker type while the Rou characterizes the sediment transport in turbulent flows like those observed in the outer surf and breaking zones. The θ measures the impact of hydrodynamics on the incipient sediment motion. Sediment transport similitude with natural conditions is achieved by adopting θ and Rou . Re defines the level of turbulence and nearshore lab experiments are generally in the fully turbulent regime even if exact similitude is not achieved.

The use of only one or two of the parameters for describing the system creates a limitation where certain important nearshore processes may be ignored. For instance, Dean and Dalrymple (2010) suggest that Fr and Ω are sufficient for morphodynamic models with sand, thereby ignoring important processes like sediment transport mode and surf similarity. Using all parameters overcomes the limitations and provides more context to the system conditions. The computed Fr and ξ values were 0.1 and 0.38 (Table 3.2), respectively indicating similarity with sandy beaches of similar scales and predominantly spilling breaker conditions (Grasso et al., 2009). The computed Ω values (2.60) imply an intermediate beach type (Dean & Dalrymple, 2010). The computed θ (Crosby and Whipple, 2004) and Rou values (0.82, 2.45) suggest the

sediment transport mode is bedload driven (Crosby & Whipple, 2004). Finally, the Re values of 1.81×10^6 indicate a fully turbulent flow field.

3.3 Instrumentation

Approximately 80 sensors were deployed in the wave flume during the experiment, but only the sensors used in this dissertation are described. A total of 25 sensors comprising 2 Nortek Vectors (V), 3 Nortek Vectrino II Acoustic Doppler Profiling Velocimeters (VECT), 8 Valeport model 802 Electromagnetic Current Meters (EMCM), and 12 MassaSonic PulseStar M-300 Ultrasonic Distance Meters (UDM) are described. The pre-and post-trial surveys of the munitions locations and beach profile elevations were achieved using the Leica Global Navigation Satellite System (GNSS) real-time kinetic global positioning system (RTK GPS), the echosounder D710U sonar, and the Trimble S5 total station.

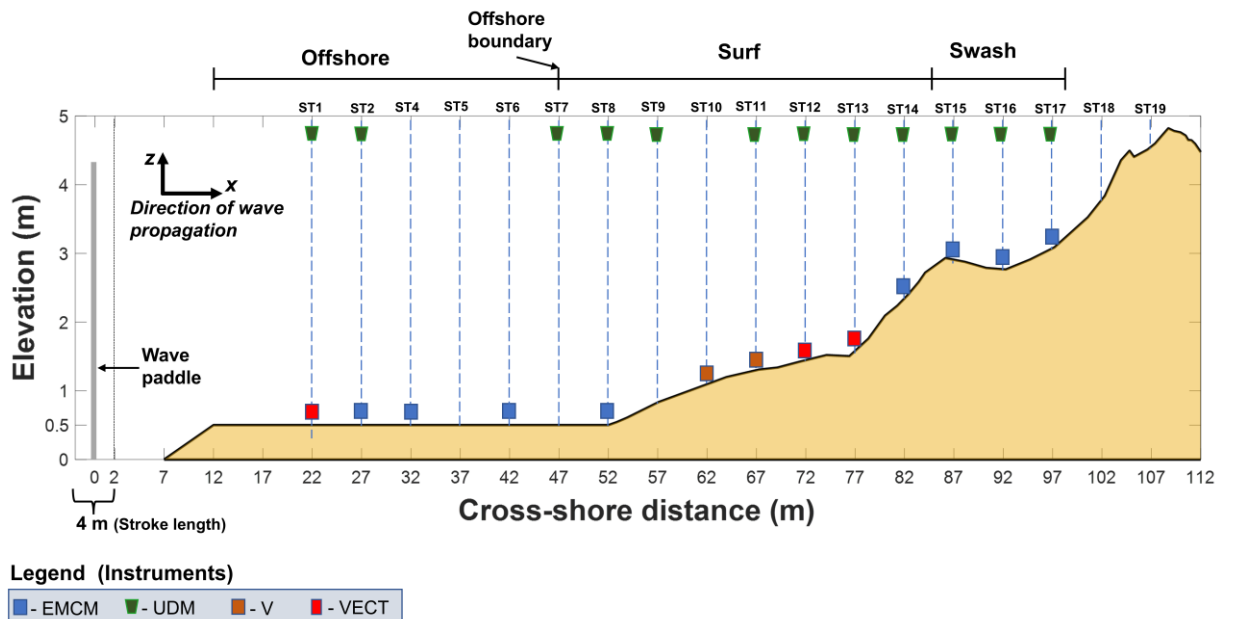


Figure 3.3: Schematic of the wave flume and the deployed sensors

Table 3.3: Relevant deployed sensors in the study

Sensor	Number	Logging Rate (Hz)	What it does
V (Vector)	2	64	Measures water level and the 3 velocity components (u, v, w) at a single elevation 15 cm below the transducer
VECT (ADPV)	3	100	Measures the 3 velocity components (u, v, w) over a 0.03 m profile at 1 mm increments
EMCM	8	16	Measures the horizontal velocity (u, v) at a single elevation above the bed.
UDM	12	6500	Measures water depth by using sonar technology
Leica RTK GPS	1	1	Used to survey munition position and subaerial or drained beach profiles.
D710U sonar	1	1	Used to survey beach profiles in the underwater portions of the wave flume
Trimble S5 total station.	1	1	Used to survey munition position and subaerial or drained beach profiles.

3.3.1 Vector (V)

The Vector (V) also known as Acoustic Doppler Velocimeter is a 3-D velocity sensor based doppler shift effect, consisting of a transmitter and three receivers by Nortek Inc (SedExpNet, 2024). The vector can record precise velocity measurements at high sample rates from small sampling volumes of water (Nortek, 2024a). One vector each, recording at 64 Hz, were placed at stations 10 and 11 in the surf zone section of the wave flume (Figure 3.4) at 0.25 m above the bed. The V measures the three velocity components (u, v , and w) at a single elevation 0.15 m below the transducer (Table 3.3).



Figure 3.4: Nortek Vector

3.3.2 Vectrino II (VECT)

The Vectrino II (VECT) or ADPV is a high-resolution velocimeter that is also based on acoustics from Nortek Inc. It is capable of measuring 3D velocity fluctuations at sampling rates of up to 200 Hz, collecting data of a 30 mm profile of water at 1 mm intervals (Nortek, 2024b). Three VECTs were placed in station one in the offshore zone and one each at stations 12 and 13 in the surf zone. The *vect* measures the three velocity components (u , v , and w) over a 30 mm profile at 1 mm increments with the first bin beginning 0.04 m below the transducer. The VECTs recording at 100 Hz were placed at station 1 at 0.2 m above the bed and at stations 12 and 13 in the surf zone at 0.06 m above the bed (Figure 3.5).

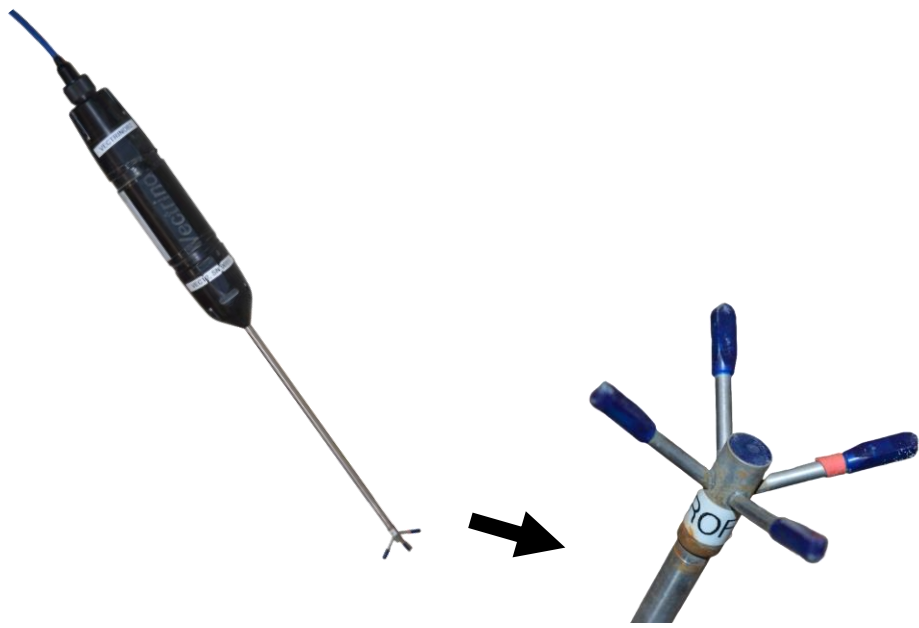


Figure 3.5: Nortek vectrino II

3.3.3 Electromagnetic current meter (EMCM)

The EMCM is a model 802 paired 3.2 discus sensor 2-axis electromagnetic current meter system that measures the velocities of flow in two orthogonal axes based on the Faraday principle from Valeport (Valeport, 2024). The EMCM measures the horizontal velocity (u, v) at a single elevation above the bed. The eight EMCMs recording at 16 Hz were placed at stations 2, 4, 6, 8 14, 15, 16, and 17 (Figure 3.3, 3.6). EMCMS were placed at 0.1 m (offshore) and 0.06 m (surf and swash zone) above the bed.



Figure 3.6: The Valeport Electromagnetic current meter

3.3.4 Ultrasonic Distance Meters (UDM)

The UDM records the vertical distance from its position to the free surface or the bed using sonar technology. The models of the 12 UDMs deployed were the PulStar Series M-300 by MassaSonic. Data were recorded at a high sample rate of 6500 Hz and resampled to 50 Hz at the pre-data processing stage. The UDMs were located at 12 of the 18 stations (Figure 3.7).



Figure 3.7: The PulStar Series M-300 ultrasonic distance meter by MassaSonic

3.3.5 The real-time kinetic global positioning system (RTK GPS)

The RTK GPS by the Leica Global Navigation Satellite System (GNSS) works by reducing the accuracy margin of standard GNSS systems from within several meters to centimeter-level precision using corrections from a network of stations or a reference station (Figure 3.8). The data obtained in MTM Zone 7 translates to UTM Zone 19- horizontal NAD83, vertical NAVD88. A Matlab function was used to convert the MTM coordinates into the local coordinates of the wave flume.



Figure 3.8: The Leica RTK GPS system

3.3.6 The echosounder D710U sonar

The echosounder D710U sonar from EchoLogger (Figure 3.9) is a high precision hydrographic instrument for measuring underwater depth and seabed profiling. It pairs seamlessly with the Leica Global Navigation Satellite System (GNSS) RTK GPS and was particularly helpful during post-trial surveys where the wave flume was not drained. The Sonar was used to capture the beach profiles in the underwater portions of the wave flume during such surveys. The sonar can operate on a wide range of frequencies and depths. The vertical accuracy is within $\pm 0.01\text{--}0.05$ m depending on system calibration and environmental conditions. The sonar was mounted on framing profiles attached to a cart that allowed the sonar to be moved from one end of the wave flume to the other in the cross-shore.



Figure 3.9: echosounder D710U sonar from EchoLogger (source:
<https://www.aditech-uw.com/en/shop/6491-echologger-eth-d710u.html>)

3.3.7 Trimble S5 total station

The Trimble S5 total station (Figure 3.10), a high-precision surveying equipment, is part of Trimble's ensemble of total stations designed to for accuracy, ease of use and reliability (Trimble Geospatial, 2024). It is based on Trimble *MagDrive* electromagnetic technology, which ensures fewer moving parts, *SurePoint* technology which ensures accurate measurement and pointing, and the *DR Plus EDM* with an accuracy of 1 mm + 2 ppm which enhances direct reflex performance and ensures fewer steps in instrument set-up (Trimble Geospatial, 2024). The measurement range can be up to 5500 m under clear conditions (Trimble Geospatial, 2024).



Figure 3.10: Trimble S5 total station

3.4 Surrogate Munitions and Canonical Objects

Munitions span a range of shapes, sizes, and bulk densities. Numerous studies employed basic cylindrical shapes and varying-sized conical frusta of various bulk densities as munition surrogates (Calantoni et al., 2014; Friedrichs et al., 2016, 2018; Garcia & Landry, 2018; Rennie et al., 2017; Voropayev et al., 2003b)

The munition sizes of interest for this effort are tapered, cylindrical, or spherical munitions or objects with cross-sectional diameters in the range of 20 mm to 155 mm (Calantoni, 2014).

An overview of the various munitions-related studies and the physical characteristics of the objects used (diameter, length, and bulk density, ρ_m) can be found in (Friedrichs et al., 2018). Here, munitions ranging from 40 mm to 155 mm diameter (D) were deployed. Canonical objects (spheres and cylinders) were also used for simplicity in modifying bulk density. Recent prior studies developed replicas with similar shapes, sizes, geometrical characteristics, and bulk densities as real munitions within an acceptable absolute error of $< 20\%$ (Bruder et al., 2018; Cristaudo & Puleo, 2020). In this study, canonical objects were fabricated using iron shavings mixed with leveling cement (spheres) or Quikrete concrete mix (cylinders; within aluminum tubes) to obtain desired densities. The target densities of the spheres were 2500 kg/m^3 , 3000 kg/m^3 , 3500 kg/m^3 , and 4000 kg/m^3 , while the target densities of cylinders were 2000 kg/m^3 , 2500 kg/m^3 , 3000 kg/m^3 , and 3500 kg/m^3 . The percent errors between the fabricated canonical objects and the target densities were within 7%. A total of 152 surrogate munitions and canonical objects were used (Figure 3.11).

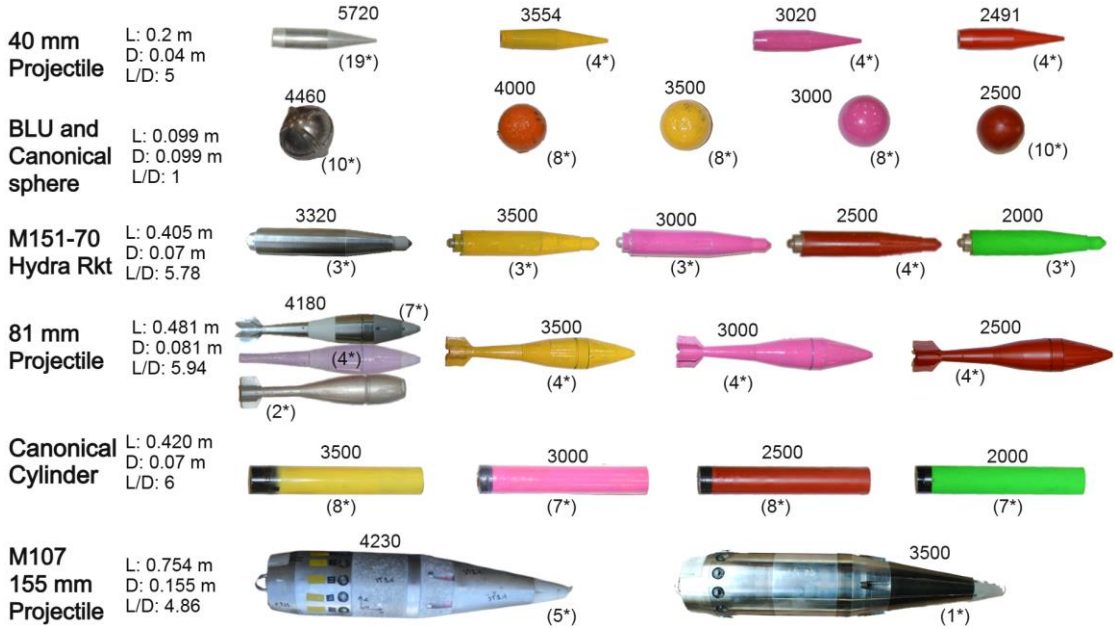


Figure 3.11: Variable density munitions and canonical objects deployed, L is the object length, and '*' indicates the number of objects of a specific type deployed.

Figure 3.11 highlights the munitions and canonical objects deployed in the study and the density range using color coding where green, red, magenta, and yellow were near 2000 kg/m^3 , 2500 kg/m^3 , 3000 kg/m^3 , and 3500 kg/m^3 , respectively. Gray/silver-colored objects retain their typical bulk density as identified by the SERDP standardized repository or military manuals (Bruder et al., 2018). When appropriate, these color codings are retained in the presentation of the results for direct correspondence. Munitions are named using the following nomenclature (Figure 3.11): Color – Munitions type – Station number – Munition number (If there are multiple munitions of the same type in the same location). For example, "YSPH_2C" is Yellow – Sphere – Station 2 – C where C means the third YSPH munition at Station 2.

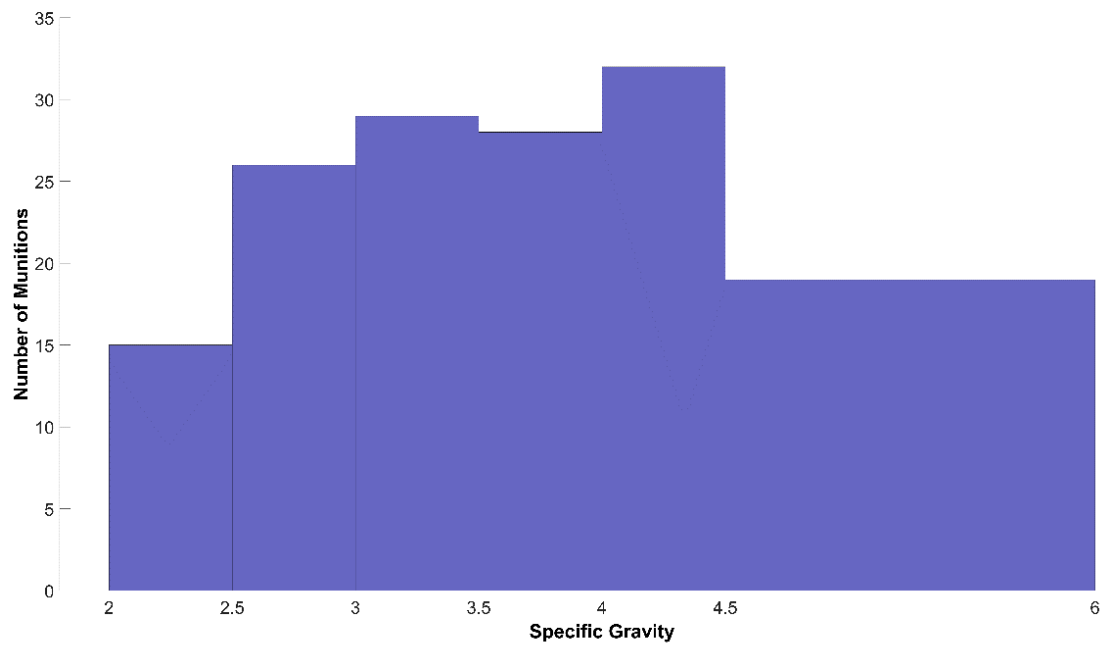


Figure 3.12: Distribution of the munitions deployed based on their specific gravity values.

An overview of the specific gravity of the munitions deployed (Figure 3.12) shows that a wide range of munitions bulk densities was deployed in the experiment. The total number of unique munitions bulk densities used within the specific gravity ranges from 2 to 6 was 13, although the total bulk density variations across all objects was 25 (Figure 3.11). To the authors' knowledge, this study comprises the largest collection and range of bulk-density munitions/objects deployed in a single study for quantifying munitions migration in the near-shore.

3.4.1 Inertia Motion Units

Three 81 mm projectiles with bulk densities of 2500 kg/m^3 , 3000 kg/m^3 , and 4180 kg/m^3 housed an x-IO inertia motion unit (IMU). The x-IO IMUs are low-cost compact sensors equipped with the Gyroscope, Accelerometer, and Magnetometer whose combined measurements provide a 9-degree-of-freedom system. The 9 degrees of freedom include triple-axis angular velocity, acceleration, Euler and quaternion angles, and rotation. The 81 mm surrogate projectiles contained watertight IMU compartments (Figure 3.13) which add enough space for external batteries for the IMUs all housed inside the munitions for data collection over an extended period. The instrumented 81 mm surrogate projectile munitions were deployed in the surf zone.

Instrumenting munitions with IMUs provided Lagrangian observations of munitions response to varied forcing conditions. The IMUs were inserted into and retrieved from the munitions before and after the Cases. IMUs were set to sleep/wake mode, extending battery life by entering sleep after 60 s of inactivity. The trigger for wake-up was set to “high sensitivity” with a sample rate of 256 Hz. The principal measurements of the IMU are roll, angular velocity, and yaw. The roll measurements were converted into translational distance and by extension, the munition trajectories within the wave flume coordinates using a cumulative sum technique (Cristaudo & Puleo, 2020; Frank et al., 2016).



Figure 3.13: Inertia Motion Unit and a sample R81 munition showing where the IMU is inserted

3.4.2 Dimensionless parameters related to munitions/objects migration and burial.

Dimensionless numbers associated with small solid structures like vertical cylinders, pipelines, and mines are the Keulegan-Carpenter number and Object mobility number (Voropayev et al., 2003a). The maximum force on small objects is simply a function of KC number and the Reynolds number (Chakrabarti, 1998). The Shields number widely applied in sediment transport for determining the initiation of motion (incipient motion) has also been found applicable for larger-sized objects due to local scour impacts. Hence, several studies have applied the shields number along with the earlier stated dimensionless numbers for quantifying the behavior of solid objects in underwater and nearshore environments e.g. Cylinders (Friedrichs et al., 2016), mines (Friedrichs, 2007), and surrogate munitions (Cristaudo & Puleo, 2020;

Puleo & Cristaudo, 2020; Rennie et al., 2017). Table 3.4 describes the dimensionless numbers and the associated equations.

Table 3.4: Dimensionless numbers associated with munitions behavior.

Dimensionless Parameter	Brief Description	Equation
Keulegan-Carpenter number (KC),	the ratio between drag and inertia forces	$KC = \frac{u_m T_s}{D}$ Where u_m is the maximum near-bed wave plus current velocity, T_s is wave period, D is the munitions diameter
Shields number (θ)	ratio between destabilizing and stabilizing forces	$\theta = \frac{\tau_b}{(\rho_s - \rho_w) g d_{50}}$ Where Bed shear stress $\tau_b = \frac{1}{2} \rho_w f u^2$ and f = friction factor
Object mobility (θ_m)	Initiation of motion and identifying the threshold for motion/no motion	$\theta_m = \frac{u^2}{\left(\frac{\rho_m}{\rho_w} - 1\right) g D}$

3.5 Procedures and Protocols

3.5.1 Wave flume setup

The steps in the wave flume setup were: 1) marking the scaled profile elevations on the flume sidewalls, 2) adding sediment using a bucket loader, 3) spreading and compacting the sediment to match the marked profile elevations, 4) installing galvanized pipes and scaffold frames at the different cross-shore stations for sensor installation, 5) routing sensor cables into the control trailer, 6) placing munitions at the different cross-shore stations, 7) conducting the experiments according to the prescribed hydrodynamic conditions, 8) periodic flume draining for profiling and munitions surveying, and 9) resetting the beach profile for the next set of

hydrodynamic conditions. Steps 1, 2 and 3 were conducted before the start of each Case. It involved the use of the bucket loader, skid steer and minimal physical labor for an even spread of the sediment in the y-axis.

Fourteen stations equipped with vertical pipes for placement of sensors originally existed from $x = 32$ m to $x = 97$ m spaced 5 m apart in the wave flume. Four more stations were created at $x = 22, 27, 102$, and 107 making a total of 18 stations. The scaffolding for the sensors consisted of steel pipes for the frames and aluminum pipes for holding the sensors. Aluminum pipes were used for holding the sensors rather than steel because steel causes interference with the electromagnetic field around the probes of the sensors, thereby creating noises in the signals. All sensors were connected to recording laptop computers or computer-controlled data loggers. Computers were on a local network receiving clock updates every second via a Garmin GPS antenna and Tac32 and Dimension4 v5.3 software.

3.5.2 Experimental steps

Some major steps after creating the beach profile in the wave flume are depicted in Figure 3.14. The sorting of the munitions involved arranging the munitions according to their station numbers (Figure 3.15, Table 3.5). The munitions were deployed strategically at the stations to achieve the objectives of the study. Stations 1(offshore), 7 (offshore/surf interface), and 18 (swash), focused on munitions with similar shapes, bulk densities and initial orientation at the same cross-shore location. Stations 2 (offshore), 11 and 12 (surf) and 17 (swash) had munitions of similar shapes and initial orientations but different bulk densities at the respective cross-shore locations (Figure 3.15). However, the munitions in station 2 were all spherical objects, and therefore initial orientation was inconsequential.



Figure 3.14: Experimental steps

The largest munitions (155 mm) were deployed spanwise at stations 1, 7, and 11 all with similar bulk density values except for station 11. The deployments at stations 2 (offshore) and 15 (swash or surf/swash interface) were spherical munitions of similar diameter with varying bulk density values emphasizing bulk density variation. At stations 4 (offshore), 8 (surf), and 13 (surf or surf/swash interface), two munition types of relatively similar lengths (CYLs and RKTs) but with varying bulk density values were deployed emphasizing variation in shape and initial orientation. At stations 5 (offshore), and 10 (surf), munitions were of similar shapes but with multiple pairs of munitions having similar bulk densities. Each munition pair had a spanwise and streamwise-oriented munition respectively, emphasizing initial orientation. Station 6 (offshore) contained two different types of tapered munitions and bulk density values all initially oriented in the same spanwise direction. At station

16 (swash or surf/swash boundary or swash), two munition types (81s and CYLs) with four bulk density variations were deployed. One of the two munition types with similar bulk densities was paired, forming pairs of different munitions with similar bulk density values (except for M81 which had no CYL pairing) and all had a spanwise initial orientation. Variable density 40 mm munitions were deployed spanwise at stations 12 and 17 while station 18 contained similar density 40 mm munitions and a pair of 81 mm projectiles all deployed spanwise to provide the best chance for migration. Finally, stations 9 and 14 (surf) both had a range of munition types of two or more different bulk densities and initial orientations represented. Munitions were mostly deployed proud, and the tapered munitions were either placed spanwise (perpendicular to the flow) or streamwise (parallel to the flow). All munitions were deployed side-by-side in the alongshore position to minimize possible interference or collision with each other during wave propagation (Figure 3.15).

Table 3.5: Munitions deployments by stations

Stations	Munitions	Specific Gravity	Orientation	Diameter (D)
1 ($x = 22 \text{ m}$)	155_1A	4.23	Spanwise	0.155
	155_1B	4.23	Spanwise	0.155
	YSPH_2C	3.5	NA	0.099
	BLU_2A	4.46	NA	0.099
	RSPH_2A	2.59	NA	0.099
	MSPH_2C	3	NA	0.099
	BLU_2B	4.46	NA	0.099
	OSPH_2B	4	NA	0.099
	RSPH_2B	2.5	NA	0.099
	RSPH_2C	2.5	NA	0.099
2 ($x = 27 \text{ m}$)	OSPH_2A	4	NA	0.099
	MSPH_2A	3	NA	0.099
	YSPH_2A	3.5	NA	0.099
	OSPH_2C	4	NA	0.099

	YSPH_2B	3.5	NA	0.099
	BLU_2C	4.46	NA	0.099
	MSPH_2B	3	NA	0.099
4 ($x = 32$ m)	MRKT_4	3	Streamwise	0.07
	YCYL_4	3.5	Spanwise	0.07
	RRKT_4	2.5	Streamwise	0.07
	MCYL_4	3	Spanwise	0.07
	GRKT_4	2	Streamwise	0.07
	RCYL_4	2.5	Spanwise	0.07
	YRKT_4	3.5	Streamwise	0.07
	GCYL_4	2	Spanwise	0.07
5 ($x = 37$ m)	MCYL_5B	3	Streamwise	0.07
	RCYL_5B	2.5	Spanwise	0.07
	RCYL_5A	2.5	Streamwise	0.07
	YCYL_5B	3.5	Spanwise	0.07
	GCYL_5A	2	Streamwise	0.07
	GCYL_5B	2	Spanwise	0.07
	YCYL_5A	3.5	Streamwise	0.07
	MCYL_5A	3	Spanwise	0.07
6 ($x = 42$ m)	S40_6A	5.72	Spanwise	0.04
	P81_6B	4.18	Spanwise	0.081
	S40_6C	5.72	Spanwise	0.04
	P81_6A	4.18	Spanwise	0.081
	S40_6B	5.72	Spanwise	0.04
7 ($x = 47$ m)	S155_3A	4.23	Spanwise	0.155
	S155_3B	4.23	Spanwise	0.155
8 ($x = 52$ m)	MCYL_8	3	Spanwise	0.07
	SRKT_8	3.32	Streamwise	0.07
	RCYL_8	2.5	Spanwise	0.07
	GCYL_8	2	Streamwise	0.07
	YCYL_8	3.5	Spanwise	0.07
	YRKT_8	3.5	Streamwise	0.07
	RRKT_8	2.5	Spanwise	0.07
	GRKT_8	2	Streamwise	0.07
9 ($x = 57$ m)	MRKT_8	3	Spanwise	0.07
	BLU_9	4.46	Spanwise	0.099
	GCYL_9B	2	Streamwise	0.07
	YCYL_9A	3.5	Spanwise	0.07
	RSPH_9	2.5	NA	0.099
	MCYL_9A	3	Streamwise	0.07
	GCYL_9A	2	Spanwise	0.07
	MSPH_9	3	NA	0.099
	MCYL_9B	3	Spanwise	0.07

	OSPH_9	4	NA	0.099
	YCYL_9B	3.5	Spanwise	0.07
	YSPH_9	3.5	NA	0.099
	RCYL_9B	2.5	Streamwise	0.07
	RCYL_9A	2.5	Spanwise	0.07
10 ($x = 62$ m)	M81_10B	3	Spanwise	0.081
	S81_10A	4.18	Spanwise	0.081
	M81_10A	3	Streamwise	0.081
	Y81_10A	3.5	Spanwise	0.081
	FLAT_10B	4.18	Streamwise	0.07
	R81_10B	2.5	Spanwise	0.081
	P81_10B	4.18	Streamwise	0.081
	FLAT_10A	4.18	Spanwise	0.07
	Y81_10B	3.5	Streamwise	0.081
	S81_10B	4.18	Spanwise	0.081
	R81_10A	2.5	Streamwise	0.081
	P81_10A	4.18	Spanwise	0.081
11 ($x = 67$ m)	155_11A	4.23	Spanwise	0.155
	155_11B	3.5	Spanwise	0.155
12 ($x = 72$ m)	S40_12C	5.72	Spanwise	0.04
	Y40_12B	3.554	Spanwise	0.04
	S40_12A	5.72	Spanwise	0.04
	M40_12A	3.02	Spanwise	0.04
	Y40_12A	3.554	Spanwise	0.04
	S40_12B	5.72	Spanwise	0.04
	M40_12B	3.02	Spanwise	0.04
	R40_12A	2.491	Spanwise	0.04
	R40_12B	2.491	Spanwise	0.04
13 ($x = 77$ m)	RCYL_13	2.5	Spanwise	0.07
	RRKT_13	2.5	Streamwise	0.07
	GCYL_13	2	Spanwise	0.07
	GRKT_13	2	Streamwise	0.07
	SRKT_13	3.32	Streamwise	0.07
	YRKT_13	3.5	Streamwise	0.07
	YCYL_13	3.5	Spanwise	0.07
	MRKT_13	3	Streamwise	0.07
	MCYL_13	3	Spanwise	0.07
14 ($x = 82$ m)	S40_14	5.72	Spanwise	0.04
	BLU_14B	4.46	NA	0.099
	Y81_16A	3.5	Spanwise	0.081
	RRKT_14	2.5	Streamwise	0.07
	RSPH_14B	2.5	NA	0.099
	R81_16	2.5	Spanwise	0.07

	BLU_14A	4.46	NA	0.099
	S81_16A	4.18	Streamwise	0.081
	R40_14	2.491	Spanwise	0.04
	SRKT_14	3.32	Streamwise	0.07
	RSPH_14A	2.5	NA	0.099
	M81_16A	3	Spanwise	0.081
	BLU_15C	4.46	NA	0.099
	MSPH_15A	3	NA	0.099
	RSPH_15A	2.5	NA	0.099
	YSPH_15A	3.5	NA	0.099
	OSPH_15D	4	NA	0.099
	RSPH_15D	2.5	NA	0.099
	BLU_15A	4.46	NA	0.099
	RSPH_15C	2.5	NA	0.099
	MSPH_15C	3	NA	0.099
15 ($x = 87$ m)	YSPH_15C	3.5	NA	0.099
	RSPH_15B	2.5	NA	0.099
	OSPH_15A	4	NA	0.099
	BLU_15D	4.46	NA	0.099
	MSPH_15D	3	NA	0.099
	OSPH_15C	4	NA	0.099
	YSPH_15D	3.5	NA	0.099
	OSPH_15B	4	NA	0.099
	BLU_15B	4.46	NA	0.099
	MSPH_15B	3	NA	0.099
	YSPH_15B	3.5	NA	0.099
	S81_16B	4.18	Spanwise	0.081
	Y81_16B	3.5	Streamwise	0.081
	M81_16B	3	Spanwise	0.081
16 ($x = 92$ m)	YCYL_14	3.5	Streamwise	0.07
	R81_14	2.5	Spanwise	0.081
	S81_14	4.18	Spanwise	0.081
	RCYL_14	2.5	Spanwise	0.07
	M40_17B	3.02	Spanwise	0.04
	S40_17B	5.72	Spanwise	0.04
	M40_17A	3.02	Spanwise	0.04
17 ($x = 97$ m)	Y40_17B	3.554	Spanwise	0.04
	S40_17A	5.72	Spanwise	0.04
	Y40_17A	3.554	Spanwise	0.04
	R40_17	2.491	Spanwise	0.04
	S40_18A	5.72	Spanwise	0.04
18 ($x = 102$ m)	S40_18B	5.72	Spanwise	0.04
	S40_18C	5.72	Spanwise	0.04

S81_18A	4.18	Spanwise	0.04
S40_18D	5.72	Spanwise	0.04
S40_18E	5.72	Spanwise	0.04
S40_18I	5.72	Spanwise	0.04
S40_18F	5.72	Spanwise	0.04
S40_18G	5.72	Spanwise	0.04
S81_18B	4.18	Spanwise	0.081
S40_18H	5.72	Spanwise	0.04
S40_18J	5.72	Spanwise	0.04

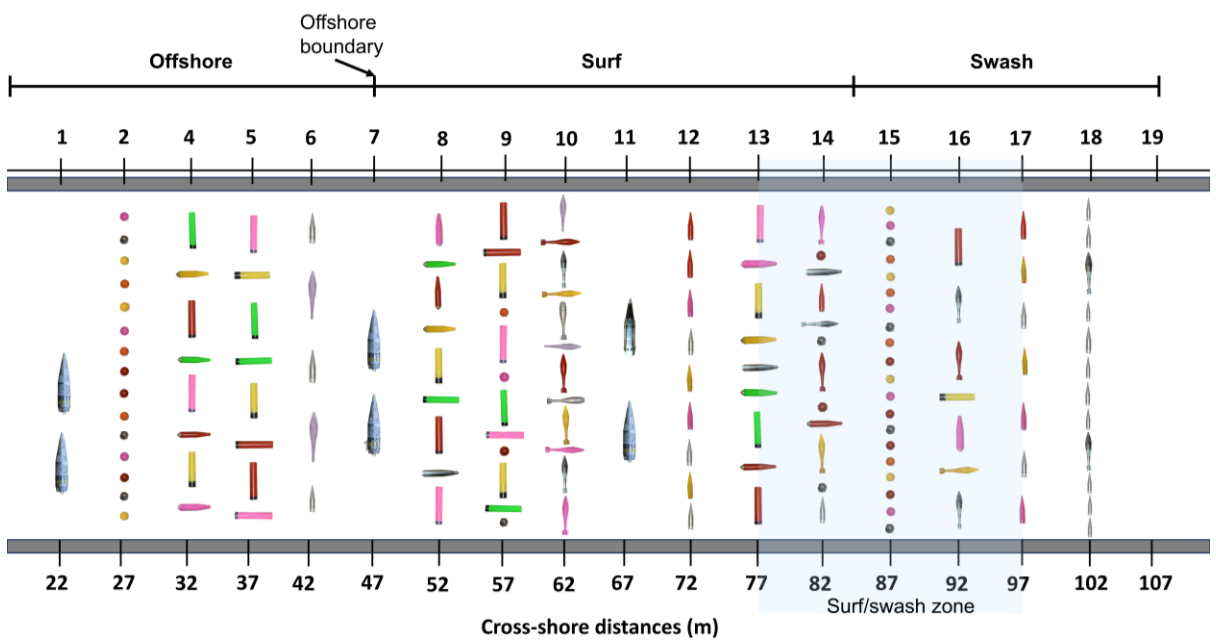


Figure 3.15: Munitions deployment layout in the wave flume

Munitions were surveyed before the first trial and generally, after every other trial when the wave flume was drained. Generally, full surveys were achieved after Trials 02, 04, and 05 in cases containing 5 trials, and in Case 05 containing 10 trials, full surveys were achieved after Trials 02, 04, 06, 08, and 10. Only partial surveys spanning the swash and shallow parts of the surf zone were achieved after the other trials.

After the munition deployments, setup of the sensors at the stations (Figure 3.3; Table 3.3; section 3.5.1) and initial surveys, the wave flume is filled up slowly to the desired still water depth based on the hydrodynamic conditions highlighted in Table 3.1 of section 3.2.3. The waves were generated and run based on the hydrographs (Figure 3.2).

The surveys involved the use of the RTK GPS or the Trimble Total Station to measure the coordinates of the munitions and the beach profiles pre- and post-trials during full surveys. Three ground control points were surveyed at the beginning of each experiment for confirmation that the GPS was recording at the correct antenna height and accuracy level.

During partial surveys, the sonar was used to survey the underwater portions of the beach profile while the RTK GPS was to survey the dry portions and the munitions. The spherical munitions (BLUs and SPHs) were measured at their tips while the tapered munitions were measured at the tip, and the base (Figure 3.16).

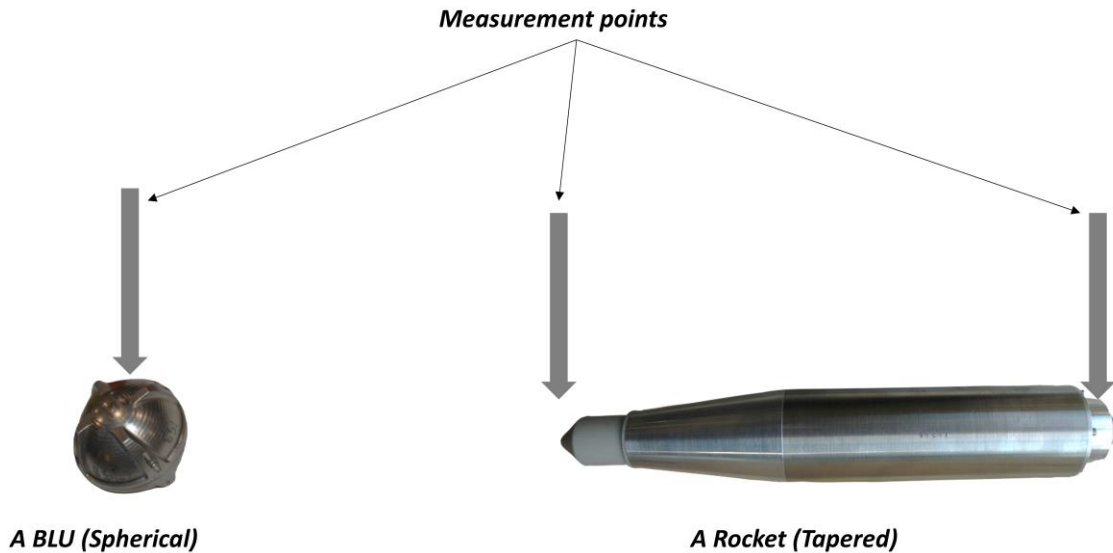
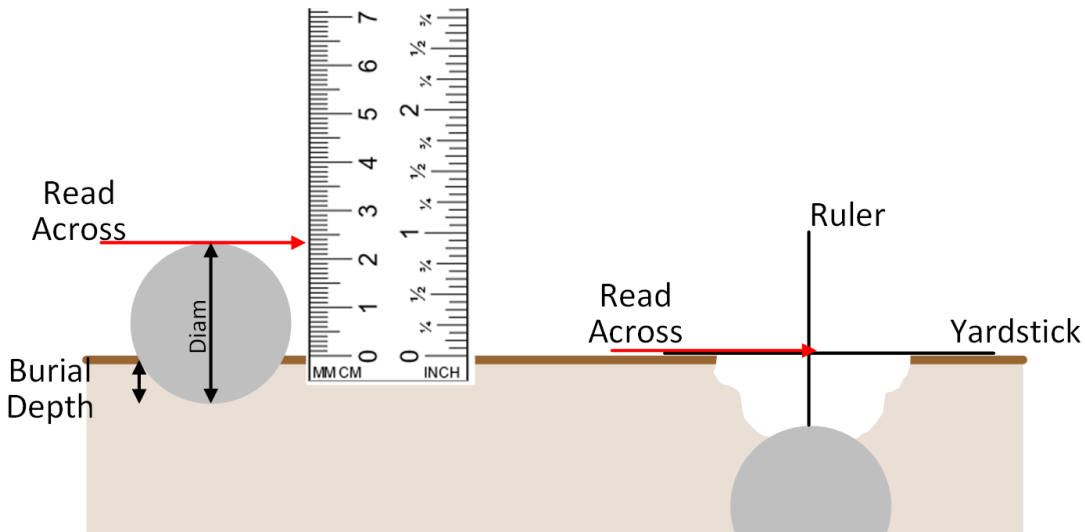


Figure 3.16: Measuring points of the munitions

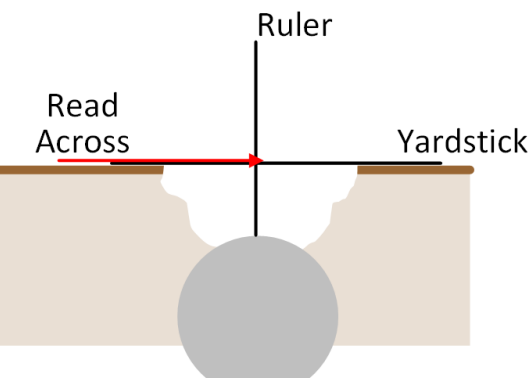
Munitions burial depths relative to the near-field profile elevation were measured either as partial or full burials. Burial depths of partially buried munitions were recorded as the depth above the bed using a ruler placed against the undisturbed bed level (Figure 3.17). Fully buried munitions were identified with metal detectors, excavated, and a yardstick or longer ruler was placed on undisturbed bed from one end of the excavation to the other, a ruler is then lowered into the opening until contact is made with the munition. The height record on the ruler from the contact to the intersection with the horizontal ruler or yardstick.

Side View: Partially Buried



Record values as NEGATIVE
e.g. -2.4 cm telling us that
diam-2.4 cm is the amount
below the sand level

Side View: Buried



Record values as POSITIVE
e.g. 1.7 cm telling us that the
munition is fully buried 1.7
cm below the sand level

Figure 3.17: Measuring munitions burial

Some munitions went missing during the experiments due to excessive burial far below the magnetic reach of the metal detectors. Others were not found because they migrated too close to the reinforced concrete side walls, and interference between the reinforced steel in the walls and the metal detectors made it difficult to locate them. However, any lost munition later found was repositioned to the last known location and re-surveyed before the next trial run. At the end of each case (hydrograph), all munitions and sensors were removed from the wave flume, and the beach profile was reset in preparation for the next case. The wave flume set-up and experimental steps are then repeated.

3.6 Data Collection Methods and Analysis Techniques

3.6.1 Sensors

The vector (V) sensor was connected to the VE Graphical User Interface (GUI) which provided the options of input settings such as the velocity range, and sampling rate. The velocity range of 0 – 5 volts which translated to 0.3 m/s to 1 m/s set at a sampling rate of 64 Hz (Table 3.3). Data were recorded in .vec format and subsequently converted into .dat and other formats.

The Vectrino II data was sampled at the highest possible sampling rate of 100 Hz, and a baud rate of 19200. The *Vectrino Profiler* (version 1.3.2) a Nortek multi-instrument data acquisition system which runs based on the latest pre-installed Java7u9 was the GUI for setting up the data collection and export of the Vectrino data. All connected Vests were grouped in the *Vectrino Profiler* software before recording to ensure they all started and stopped recording at the same time.

The EMCM and few other sensors not covered in this dissertation were routed into the NI6225 data logger by National Instruments. The *DAQExpress* 5.1 was the GUI for setting preferences and recording data. The voltage input of the EMCM was -5 to 5 volts and the terminal configuration for the EMCM was “Referenced Single Ended”. The EMCM data were recorded at 16 Hz sampling rate (Table 3.3) and exported in both .csv and .tdms formats. The micro-seconds were not captured in the csv files but were captured in the tdms files. Hence, the time stamps were obtained from the tdms files. The EMCM time series data was adjusted for a time delay of 5/16 of a second (0.3125 s) across all the files. There was a direct 1:1 ratio between the voltages recorded as outputs and actual flow velocities, hence there was no need to apply any correlation co-efficient for converting into u (m/s).

The different computers being used for recording data from the sensors were all connected to a local network receiving clock updates and hence, a central time for all computers. The central time was achieved by connecting all the computers to a laptop with a Tac32 from CNS Systems. The central time was obtained from a network of satellites via a Garmin GPS antenna. Tac32 automatically sets a computer’s internal clock at an accuracy level 10 – 25 milliseconds. The time display updates synchronously with the GPS signal and corrects for time delays in the instrumentation and the cables (CNS Systems, 2024). Each connected computer grabbed and interacted with central time using the Dimension 4 v5.3 software installed on the operating system.

The UDM data were recorded on a different server using the NI cRIO-9025 CompactRIO controller by National Instruments. The NI cRIO-9025 is a CompactRIO controller manufactured by National Instruments, essentially acting as a real-time

embedded controller used for advanced control and monitoring applications in industrial settings. An LED and an extra UDM were jointly connected to the NI cRIO-9025 on which all the UDMs were mounted and the NI6225 on which the EMCMS were mounted using a channel splitter. The time series of both signals were harmonized by obtaining the time offsets between the two signals using an xcorrelation (xcorr in Matlab) approach and applying the time offset to the UDM data to synchronize with the EMCM data. The time offset was applied to the UDM datasets and not the EMCM datasets because the EMCM datasets are connected to the central time linked to all other sensors. The UDM data was originally recorded at 6500 Hz but resampled to 50 Hz .parquet files which had also incorporated the correlation coefficient between the voltages and actual depths recorded. The .parquet files were the formats used for the harmonization process using the time offsets.

3.6.1.1 Time series synchronization of sensors data

The time series of all sensor data were synchronized with the first Vectrino II datasets for all experimental runs. The Vectrino II was chosen because it has the highest sampling rate (100 Hz) of all the sensors and it was located farthest offshore in the wave flume. The first step was to synchronize all other *vect* time series data whose timestamps had earlier been converted into the Matlab time using an in-house code called epoch2Matlab in a loop. Secondly, an initial cleaning was performed on all the vectrino data using the following cutoffs/filters; dbcut = -40, corrcut = 60, and badbeams = 2 where dbcut, corrcut, and badbeams are the amplitude cutoffs, correlation cutoff, and the minimum number of bad beams before data is “NaNed”.

Each sensor's data was then iteratively time-synchronized with vect1 data by interpolation. The sensors include the other vects, vector, EMCM and UDM.

3.6.1.2 Data cleaning

The data cleaning was done separately for each sensor.

UDM

The UDM data cleaning was done first because it provides the depth data used as a cutoff during the data cleaning of sensors close to the shoreline that experienced intermittent wetness and dryness. During the cleaning process, the parts of the data outside of the period between the start and end times of each experiment were cut off. The original UDM data captured the distance from the elevation of the UDM to the water level. Series of codes were written to obtain the actual water elevations from the bottom up using a back-calculation process. The water depths were obtained from the elevations by subtracting the profile depth from the water elevation at the same x-location. This was a straightforward process for the UDMs located in the underwater portions, but more complications were introduced in the UDMs located in the surf/swash zones where there was intermittent wetting and exposure of the beach profile. The datasets captured both water elevation during wetness phase and the beach profile elevation during dryness phase and the beach profile elevation was constantly changing due to erosion/accretion processes. A code was used to obtain the time-series of the changing beach profile elevation at the UDM's location using a moving window approach. The obtained changing beach profile elevation was then subtracted from the water elevation data to obtain the water depth. After a series of painstaking iterative process, a lowpass filter with an $f_{cut} = 0.8$ was found to be the sweet spot for

eliminating most of the noises in the signal without losing too much good data and this was applied to the time series data of the water elevations and depths.

EMCMs

The parts of the data outside of the period between the start and end times of each experiment were first “NaNed”. A built-in 1-D median filtering function in Matlab called “medfilt1” was used for cleaning the data. The medfilt1 is a nonlinear technique which applies a sliding window to a sequence and replaces the center value in the window with the median value of all datapoints in the window (Pratt, 1991). The $n = 51$ was found to be the optimal number, where n is the nth-order 1D median filter to the timeseries data, and it was applied to all the EMCM datasets. Additionally, a water depth cutoff of 0.02 m (20 cm) was applied to the EMCMs located in the surf/swash zones. The cutoff implied that any part of the timeseries where the water depth was less than 2 cm, was classified as dry and therefore, no velocity datapoint.

VECTORS (V)

A similar process to the EMCM was conducted on the vector data. The portion of the timeseries between the start and the end of the experiment was retained for each dataset. Then the medfilt1 with $n = 51$ was applied to the dataset to obtain the cleaned v data.

VECTRINO II (VECT)

The *vect* data is unique in that it measures the velocity profile over 3 cm at 1 mm intervals. The elevations of the *vect* sensor were mostly above the bed for all the experiments, and therefore the mean of the u component of the 3 cm velocity profiles

to obtain a representative 1 dimension time series data i.e. a velocity profile containing 30 bins of velocity time series were converted into one velocity time series. After obtaining the 1D velocity time series, the process applied to the vector data was applied to obtain the cleaned *vect* data.

Additionally, an absolute velocity threshold of 3 m/s was applied to all the velocity datasets (*vect*, *v* and *emcm*) and spikes with values larger than the threshold were removed.

3.6.2 Munitions migration

The munitions location data obtained using the RTK GPS, total station and manually were aggregated for all cases and trials and organized into .mat files. An in-house MTM2INRS Matlab code was used to convert the location data from the MTM zone 7 coordinates into the flume coordinates. The organized data contained the x, y, z components measures at the tip and base/mid portions of the tapered munitions and in the tip of the spherical munitions as described in Figure 3.15. Final tables of the location data were created and saved in .mat formats. The expected measurement error O is (0.05 m).

3.6.3 Munitions burial

The raw manually collected munitions burial data were transferred into excel spreadsheets. The measured burial depths were adjusted by subtracting the munitions

diameter from the measured burial to obtain the actual burial values of the munitions. Errors in naming and obvious measurement errors were checked and corrected. The munitions naming scheme was made consistent with the naming scheme for the location data. The data were subsequently organized into a giant struct file containing the burial data for all cases and trials. The expected measurement errors O is also (0.05 m).

3.6.4 Munitions data table

The aggregated munitions data brings together all elements of the project into an overall output that contains information on munitions deployed, the associated migration and burial of each munition, the local hydrodynamics and morphodynamics associated with each munition across all cases and trials.

A code for obtaining the bulk statistics of all the velocity data was written to accept the velocity time-series data (*vects*, v and *emcm*) as inputs and calculate u_{rms} , $u_{2\%}$, and u_{mean} , of the full-time series data and others like the offshore, onshore, and wet components of the velocity time series data. The data was organized into tables according to cases and trials.

A giant MATLAB code that accepts the disparate burial, location, bulk statistics, profile elevation, and wave characteristics (H_s , H_{rms}) datasets was developed. In the code, 58 different variables were developed all describing different components of the munition's behavior including the associated dimensionless number values associated with each munition. See Appendix A for full details and description of the table and its components.

Chapter 4

BEACH PROFILE MORPHODYNAMICS UNDER VARIED FORCING CONDITIONS

The hydrodynamics and beach profile morphology play a pivotal role in the extent of migration and burial of the munitions. In this chapter, the results of hydrodynamics and the beach profile responses are presented.

4.1 Hydrodynamics under the hydrographs

The velocity and water depth measurements captured by the different sensors were organized systematically from the offshore to the beach face (Table 4.1). Table 4.1 serves as a quick look-up of the sensors at each station. During the experiments, some sensors malfunctioned, and the bad data were excluded from the analysis.

Table 4.1: Sensors look-up table

STATION	X (m)	Velocity sensors	Nominal height above the bed (m)	UDM is defined by number
1	22	"VECT"	0.25	1
2	27	"EM1"	0.10	-
4	32	"EM2"	0.10	2
6	42	"EM3"	0.10	-
7	47	-	-	3
8	52	"EM4"	0.10	4
9	57	-	-	5
10	62	"V1"	0.25	-
11	67	"V2"	0.25	6
12	72	"VECT4"	0.06	7
13	77	"VECT5"	0.10	8
14	82	"EM5"	0.03	9
15	87	"EM6"	0.03	10
16	92	"EM7"	0.03	11
17	97	"EM8"	0.03	12

As an example, the velocity time series across the entire cross-shore for the largest forcing condition, Case03Trial01, is depicted in Figure 4.1.

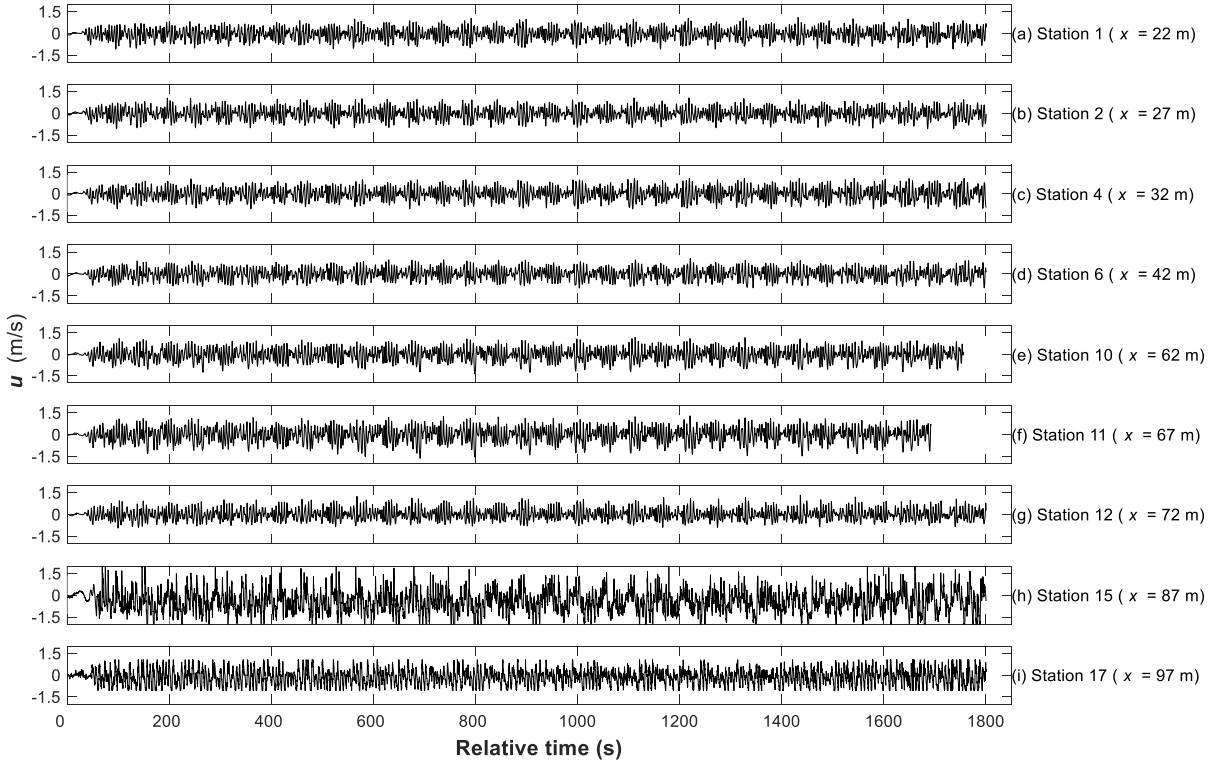


Figure 4.1: Time series of the velocity sensors from the offshore zone to the beach face

The fluid velocity was generally greatest at station 15, the point after which most of the wave breaking occurred in this case (Figure 4.1). However, the time series shown is too long to see obvious trends. Hence, the hydrodynamics of stations 1, 12, and 17 representing the offshore, surf, and swash zones respectively, and containing both UDMs and velocity sensors are further examined by zooming in on the first 100 s

of the experimental run. The velocity (u) and depths (h) of the respective stations are plotted side-by-side (Figure 4.2).

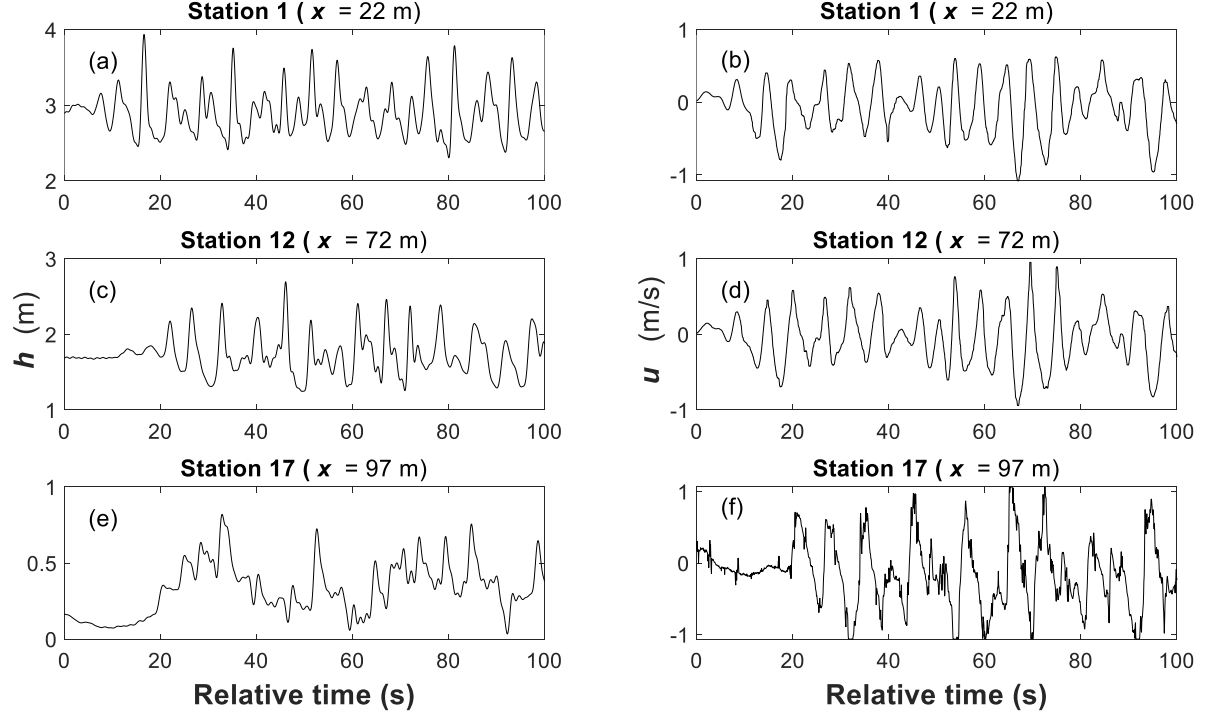


Figure 4.2: Time series excerpts of water depth (h) and cross-shore velocity (u) for the first 100 s of the largest forcing conditions (Case03, Trial 01) in the offshore (a,b), surf (c,d), and swash (e,f) zones.

The time series shows a progressive decrease in h as waves propagate from the offshore to the swash zone (Figure 4.2). Breaking processes and bore capture led to fewer waves observed near the beach face compared to offshore (Figure 4.2). There is a transition to more skewed/asymmetric waves with a decrease in water depth (Figure 4.1 b,d,f). Swash data are more sawtooth-shaped, as expected (Baldock, 2019). The profile contained a long flat section providing space for waves coming off the paddle to adjust to local water depth before shoaling on the actual profile. Still, the accommodation space may have been insufficient, causing alterations to the wave

shape relative to expectations for the actual depth. Also, the UDM sensors had limited capability for capturing the peaks of steep wave crests. It is believed these alterations are insignificant for the study of migration given the deployment of munitions across the profile.

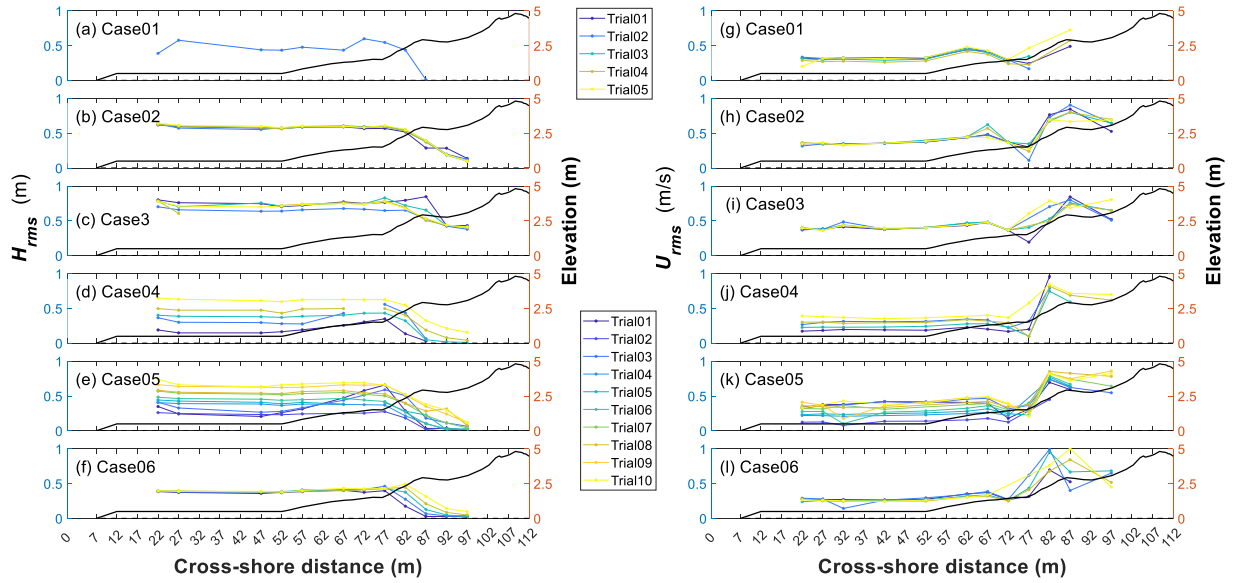


Figure 4.3: Cross-shore distribution of H_{rms} (a–f) and U_{rms} (g–l) for all Cases.

The bulk hydrodynamics across the entire cross-shore for all the cases were examined using H_{rms} and U_{rms} values. Variations in the H_{rms} and U_{rms} from the UDMs and velocity meters for all cases and trials are presented in Figure 4.3 (where rms is the root mean square). The H_{rms} was calculated assuming a Rayleigh distribution as a direct relationship with H_s as $H_{rms}=H_s/\sqrt{2}$, and H_s is estimated from the UDM data using the relationship $H_s=4*\sigma_h$, where σ_h is the standard deviation of the free surface oscillation. H_{rms} values tend to show a gradual progression with slight

shoaling followed by breaking. Case04 and Case05 showed the widest variations in H_{rms} due to the progressive increase in H_s from 0.21 m to 1.1 m in both Cases. Breaking typically occurred near $x = 77$ m with variations depending on forcing conditions. Waves then dissipated across the remainder of the profile into the swash zone.

The U_{rms} were computed by obtaining the root mean square of the velocity time series. The U_{rms} values (Figure 5g–l) followed similar patterns with the H_{rms} observations. Velocities for Case01, Case02, and Case03 were nearly constant at around 0.4 m/s across the flat section; indicative of the wave field having adjusted to the local water depth. The similarity also suggests that for these trials, the wave height variability did not cause large variability in U_{rms} , likely due to a corresponding increase in still water depth. Case04 and Case05 did show a consistent increase in U_{rms} with respect to trial number as the wave height and period increased with the increasing still water depth. Case06 had the longest wave periods and fixed wave heights. Little variability in U_{rms} was observed in the flat section, and magnitudes were smaller than for the first three Cases. For all Cases, U_{rms} were greatest following breaking and into the swash zone. These observations imply that erosion/accretion processes and near-bed forcing were more prominent in the inner surf and swash zones. Thus, migration processes may also be more prominent in these regions.

4.2 Morphological responses to the hydrodynamics under the hydrographs

Temporal variability in beach profiles for Case03, as an example, shows the locations of erosion and accretion and variability in local beach slopes (Figure 4.4). The berm between $x = 82$ m and $x = 90$ m eroded offshore, causing accretion and sand

bar formation between $x = 76$ m and $x = 82$ m (Figure 4.4). The sand bar shifted offshore as the trial sequence progressed and this motion was observed for many of the Cases.

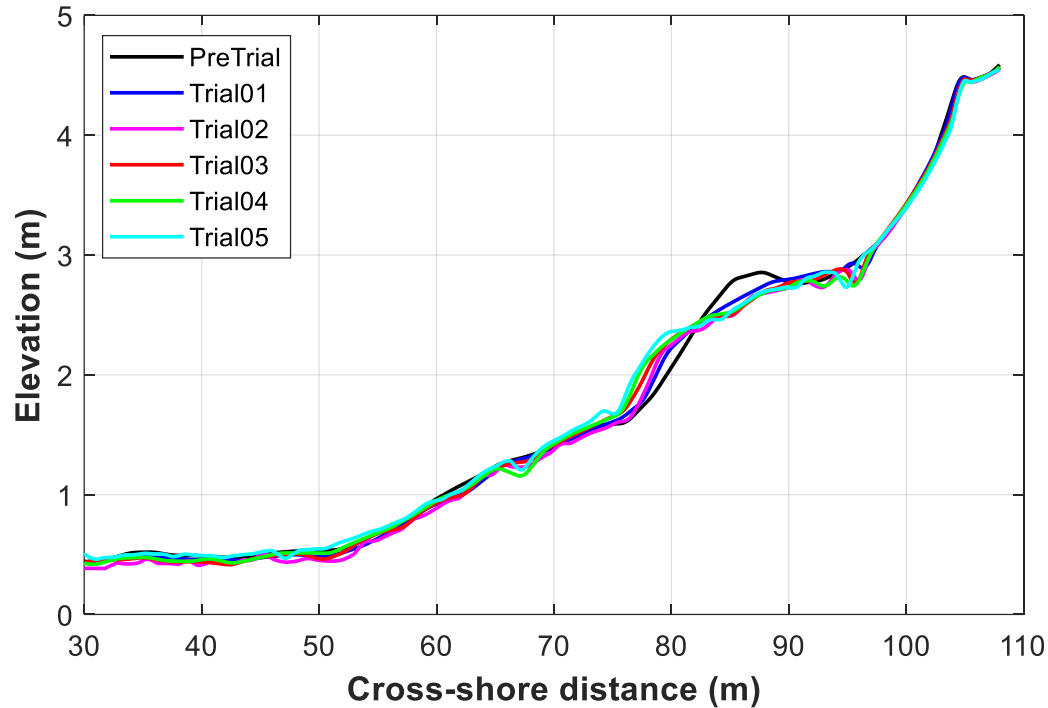


Figure 4.4: The beach slope is gentler at about 1:20 from the flat section to $x = 72$ m and steeper at about 1:5 between $x = 72$ to $x = 87$ m of the scaled profile. Overall, the foreshore profile is relatively steep at about 1:14.

The morphodynamics for all cases were analyzed by subtracting the beach profile measurements after each trial from the pre-trial measurements (Figure 4.5). Positive and negative values imply accretion and erosion, respectively. Across all Cases, minimal bed level changes (within the range of ± 0.1 m) were observed in the offshore zone to roughly $x = 70$ m. The small changes are likely due to sensor accuracy, weak sediment transport gradients, and variations in three-dimensional ripple formation and migration captured using a single cross-shore profile. From $x =$

70 m to $x = 100$ m, more substantial erosion/accretion to a magnitude of 0.4 m was observed (Figure 4.5). The region from $x = 75$ m to $x = 90$ m, where wave breaking was concentrated and with the steepest slope (1:5), experienced the most noticeable bed level changes.

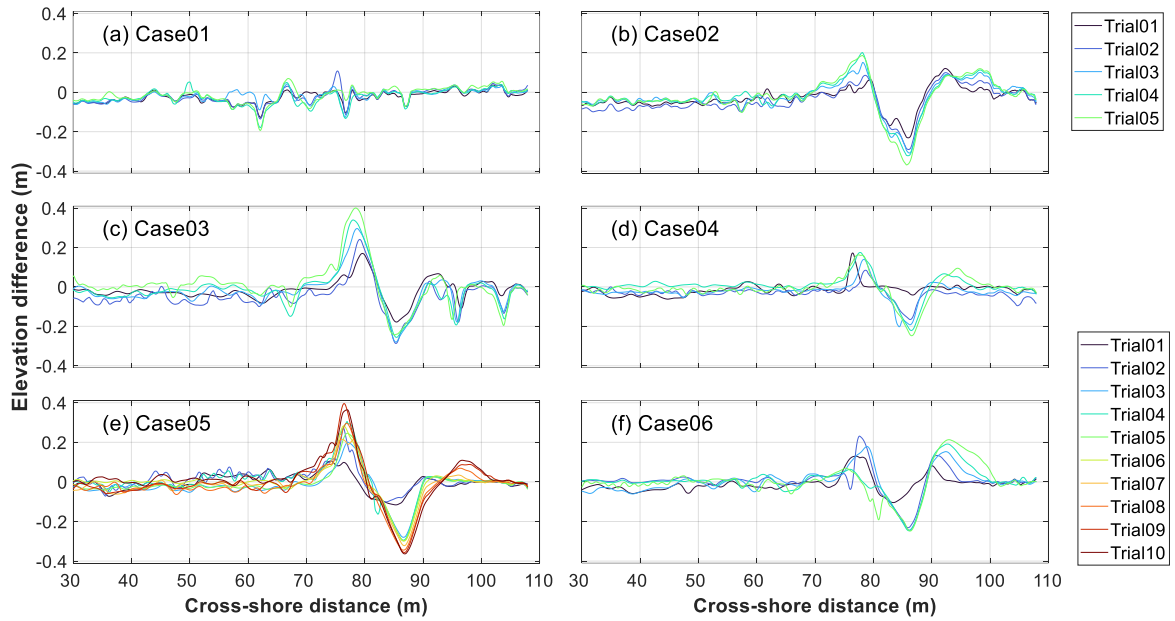


Figure 4.5: Changes in the beach profile elevation relative to the pre-trial elevation.

The bed level changes and morphodynamics observed across the cases vary from least to most severe as Case01, Case04, Case06, Case02, Case03, and Case05. Case01 had the smallest still water depth, and H_s , values of 2.1 m and 0.72 m, respectively (Table 3.1), and was also one of the shortest hydrographs (Figure 3.2). Bed level changes were less than ± 0.2 m even in the region between $x = 70$ m and $x = 90$ m, indicating little variability in the berm. Case04 had conditions of still water depth and H_s of 2.23 – 2.87 m and 0.21 – 1.1 m, respectively. Berm erosion and sand

bar formation occurred between $x = 80$ m to $x = 90$ m and $x = 75$ m to $x = 80$ m, respectively. Case06 had a still water depth range of 2.23 – 2.87 m similar to Case04, but with a constant H_s of 0.6 m and longer wave periods. Unlike Case04, greater accretion occurred offshore of the erosion point between $x = 75$ m and $x = 80$ m and onshore between the $x = 90$ m and $x = 100$ m region coinciding with the dune toe. Case02 had a still water depth of 2.87 m and $H_s=1.1$ m values, leading to weaker accretion and greater erosion from $x = 75$ m to $x = 80$ m and $x = 80$ m to $x = 90$ m, respectively, than in Case06. Case03 had the largest still water depth and wave height combinations (3.3 m and $H_s= 1.4$ m), resulting in extensive accretion and sand bar formation from $x = 75$ m to $x = 80$ m and corresponding erosion of the berm and dune toe. Although Case03 had the strongest forcing conditions, Case05 had the most substantial morphodynamics, likely due to the longer duration. Case05 is the longest hydrograph (Figure 3.2), and the forcing ran over the course of 10 trials. The longer duration led to a greater magnitude of erosion and accretion relative to Case04, a similar Case to Case05 except for the longer duration as well as Case03.

Chapter 5

MUNITIONS MIGRATION IN RESPONSE TO THE VARIED FORCING CONDITIONS

5.1 Introduction

The understanding of munitions migration dynamics in the nearshore remains limited. Empirical attempts at describing the phenomenon have proven difficult and unreliable. This study leverages on the volume of migration observations in using a probabilistic approach to create quantifiable insights into the migration tendencies of the munitions in the nearshore and shallow water regions. Results presented in this chapter attempts to provide a deeper understanding of the migration tendencies of munitions given their bulk-densities, shape and initial orientation. The migration tendencies were explored through bulk observations of migrations and a limited analysis of the instantaneous observations of munitions migration.

5.2 Bulk description of variable density munitions migration response to the controlled forcing conditions

Three migration types were calculated. The first is the actual migration where the pre-trial munitions location (location before) were subtracted from the post-trial munitions location after each trial (location after). In instances where pre-trial location measurement was absent either because the munition was not found at the pre-trial stage or the munition was underwater, the last available location was used as the location before. The second was the trial-to-trial migration where munitions location were pre-trial measurement was subtracted from the post-trial location measurement,

regardless. The challenge with trial-to-trial migration dataset is that it only takes the pre-trial location or post-trial location to be absent for no data to exist and this was fairly common due to the large number of munitions deployed. The third migration type computed was the cumulative migration where the initial locations of the munition prior to the start of each experimental case were subtracted from the post-trial munition location as the case progressed from one trial to the next. Henceforth, migration in the rest of this chapter and generally in the dissertation refers to the first description of migration unless otherwise stated. Migration distances were subdivided into two categories: “no motion” for cross-shore migration magnitudes less than or equal to 0.5 m, and “motion” for cross-shore migration magnitudes exceeding 0.5 m. This threshold value was chosen based on roughly the longest dimension of the munitions that often-experienced motion (mortars and rockets) and a desire to exceed expected measurement errors (0.05 m) by an order of magnitude.

5.2.1 Munitions migration across the entire cross-shore

The entire cross-shore comprises the offshore zone characterized by a relatively flat bathymetry at the bed, the surf zone where wave breaking occurred and water depth progressively decreased due to the changing slope and the swash zone characterized by intermittent uprush and backwash on the beach face. Of the total 152 munitions deployed, 40 munitions (26%) were initially deployed in the offshore zone. The munitions deployed in the surf zone and swash zones varied from 42 to 55% and 19 to 32%, respectively. Munitions were surveyed before the first trial and generally, after every other trial when the wave flume was drained. Munitions that were landward of the maximum runup and experiencing no hydrodynamic forcing were

excluded from the data set. A total of 2228 migration measurements were obtained encompassing all cases and trials.

Data are presented in tabular form and as histograms (Table 5.1, Figure 5.1) with the color-coding separating munitions by specific gravity (SG) and matching the munitions colors provided in Figure 3.11. Negative and positive migration values imply offshore and onshore migration, respectively. The “motion” and “no motion” migration observations were 349, and 1879, respectively, implying that 84% of the deployed munitions did not migrate beyond 0.5 m of their initial location. The percentages of the “no motion” munitions (Figure 5.1) with SG ranges of $2 \leq SG < 2.5$, $2.5 \leq SG < 3$, $3 \leq SG < 3.5$, $3.5 \leq SG < 4$, $4 \leq SG < 4.5$, and $4.5 \leq SG < 5.8$ were 8% (152), 17% (317), 19% (357), 21% (391), 27% (517), and 8% (145), respectively (Table 5.1). Munitions in the SG range of $2.5 \leq SG < 3$ (17%) were two times more likely to migrate ≤ 0.5 m compared to munitions with $SG < 2.5$ (8%) given similar forcing conditions. Migration percentages for the same SG values for “motion” munitions were 16% (57), 31% (108), 17% (61), 14% (47), 19% (65), and 3% (11). These percentages spread across the SG ranges, implying that SG may be less important for net migration provided the forcing is sufficient to exceed initiation of motion. Overall, 58% (202 of 349) of the net migration events were offshore directed. Wave non-linearity, the existence of an undertow, and local bed slope are factors that may relate to offshore migration.

Table 5.1: “No motion” and “motion” values and percentages based on the SG ranges.

SG Ranges	$2 \leq SG < 2.5$	$2.5 \leq SG < 3$	$3 \leq SG < 3.5$	$3.5 \leq SG < 4$	$4 \leq SG < 4.5$	$4.5 \leq SG < 5.8$	Total
No motion	8% (152)	17% (317)	19% (357)	21% (391)	27% (517)	8% (145)	1879
Motion	16% (57)	31% (108)	17% (61)	14% (47)	19% (65)	3% (11)	349

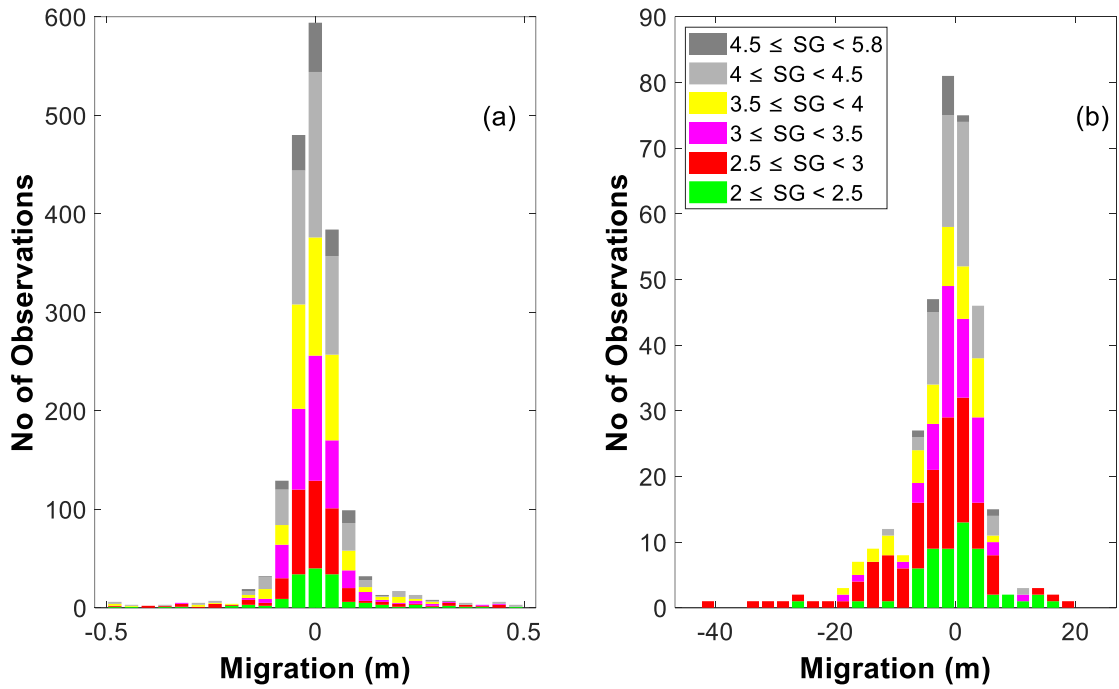


Figure 5.1: Migration distances for munitions in the nearshore; (a) no motion; (b) motion.

A net offshore or onshore migration distance magnitude exceeding 5 m was considered major and comprised 100 of 349 (29%) munitions. Of those 100 munitions, 67% (67) had SG of < 3 , implying that although SG values may be less important for “motion” migration provided the forcing is sufficient to exceed initiation of motion, the SG may become a dominant factor for long-distance migration.

5.2.2 Munitions migration in the offshore zone

The offshore zone is the region from $x = 0$ m to $x = 47$ m. It is characterized by flat bathymetry, continuous submergence of munitions, non-breaking waves, and minimal changes in the overall morphology. A total of 812 munition data points were obtained comprising 94% (764 of 812) and 6% (48 of 812) “no motion” and “motion” migrations, respectively (Table 5.2; Figure 5.2). There was a higher percentage (705 of 764; 92%) of the “no motion” munitions with $SG \geq 2.5$ (Figure 5.2). The corresponding “motion” (48; 6%) (Table 5.2a) implies that 60% (29) had $SG < 2.5$, while 83% (40) had $SG < 3$. In total, 31 of the 48 “motion” migrations had net onshore migration implying that more munitions (65%) migrated onshore in the offshore zone. The onshore migration tendency in the zone is also evident in the “motion” histogram which is overwhelmingly skewed to the right (Figure 5.2). Only 6 of 48 (13%) of the “motion” munitions traveled more than the 5 m cutoff for what is considered a major migration, and their SG values were all in the $SG \leq 2.5$ range. These observations suggest that in the offshore zone over flatter bathymetry, the munitions bulk density and wave skewness are important for net migration.

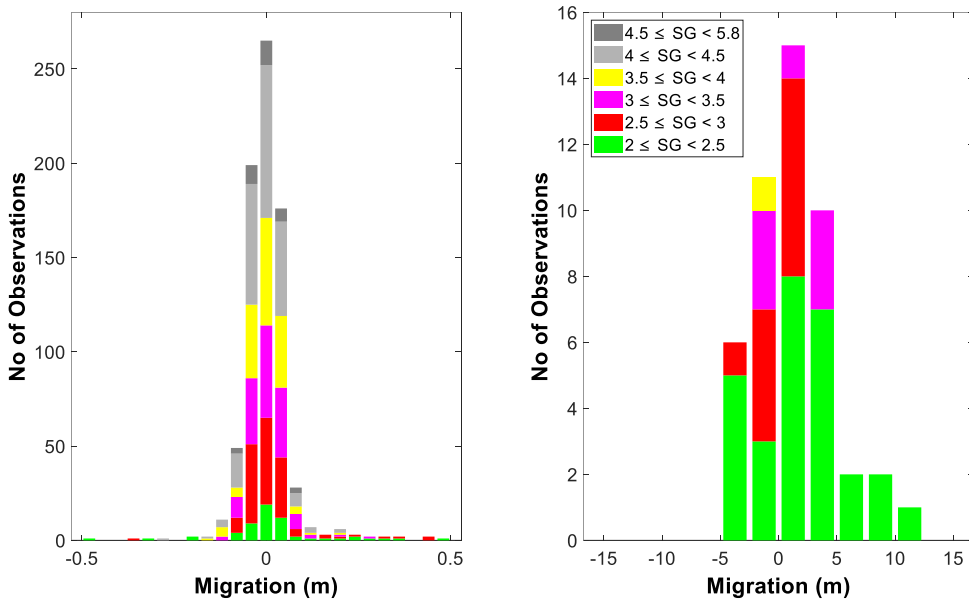


Figure 5.2: Migration distances for munitions in the offshore zone. The left and right are the “no motion” and “motion” data, respectively.

Table 5.2: “No motion” and “motion” values and percentages based on the SG ranges and cases (offshore).

(a) SG Ranges	$2 \leq SG < 2.5$	$2.5 \leq SG < 3$	$3 \leq SG < 3.5$	$3.5 \leq SG < 4$	$4 \leq SG < 4.5$	$4.5 \leq SG < 5.8$	Total
No motion	8% (59)	18% (141)	19% (146)	20% (151)	30% (231)	5% (36)	764
Motion	60% (29)	23% (11)	15% (7)	2% (1)	0%	0%	48
(b) Cases	Case01	Case02	Case03	Case04	Case05	Case06	Total
No motion	95% (112)	89% (131)	88% (99)	96% (139)	96% (178)	97% (105)	764
Motion	2% (2)	11% (16)	12% (13)	4% (6)	4% (8)	3% (3)	48
Total	114	147	112	145	186	108	812

The percentages in each case were calculated as a function of the total number of migration datapoints in the case (Table 5.2b). Case05 had the largest number of data points (186) because it contained more trials (10 trials) than the other cases (5 trials). Unsurprisingly, Case03, with the largest forcing combinations (Table 3.1), produced the largest percentage value for “motion” migration (12%) of all the cases

(Table 5.2b). Case04 and Case05, produced nearly identical migration behavior for both “no motion” and “motion” migrations both at (96%, 4%), respectively (Table 5.2b). The histograms of the migrations in the offshore zone were separated into the cases (Figure 5.3). The “no motion” migrations across all the cases follow a nearly normal distribution or are skewed towards onshore migration. The “motion” migrations across all cases also skewed more towards the onshore (Figure 5.3). Expectedly, the SG values of the “motion” migrations were mostly in the $2 \leq SG < 2.5$ and $2.5 \leq SG < 3$ ranges, regardless of the case. Few “motion” munitions in the $3 \leq SG < 3.5$ range (e.g., Figure 5.3, Case01, Case02, and Case03) migrated beyond 5 m, further emphasizing the importance of bulk density on munitions long-distance migration. As discussed in Section 4.2, the offshore zone experienced relatively weaker nearbed forcing due to the water depth (Figure 4.4).

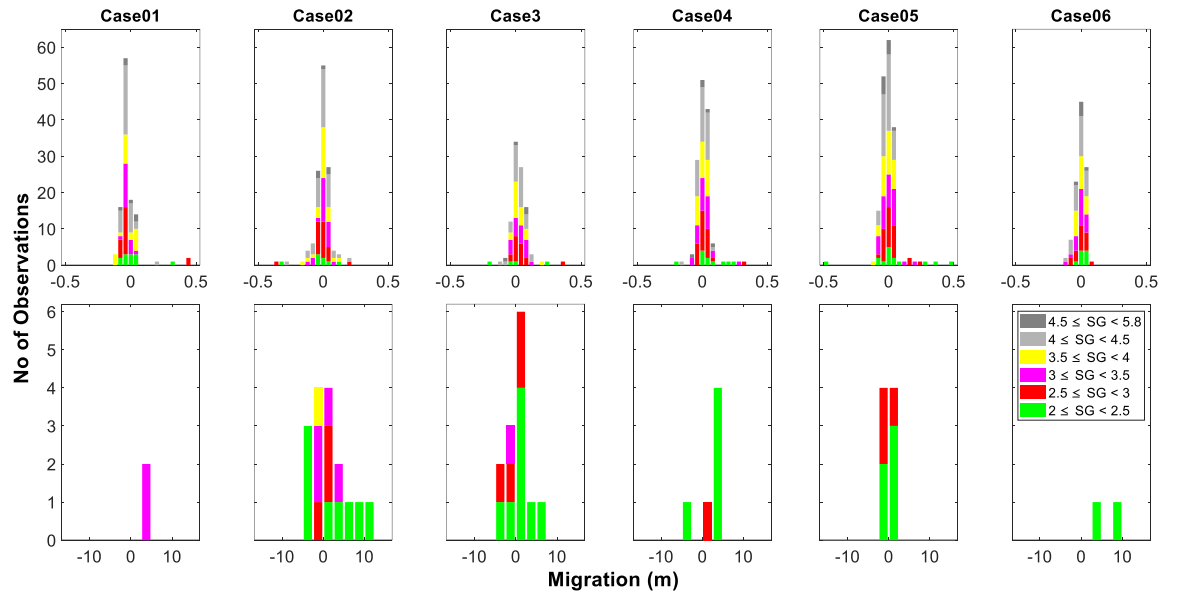


Figure 5.3: Migration distances for munitions in the offshore zone separated into cases. The top and bottom rows are the “no motion” and “motion” data for each case, respectively.

5.2.3 Munitions migration in the surf zone

The surf zone typically extended shoreward from $x = 47$ m to the surf/swash boundary between $x = 77$ m and $x = 97$ m, depending on the water depth and wave characteristics. This region was characterized by relatively steep slopes (1:20 – 1:5) with increasing steep-ness shoreward. Munitions in the surf zone accounted for 42–55% of the total munitions deployed and the migration observations in the surf zone account for 51% of the total migration data points. A total of 1212 surf zone observations from were made comprising (241; 20%) and (971; 80%) data points for the “motion” and “no motion” net migrations, respectively (Figure 5.4; Table 5.3a).

The 80% (971 of 1212) “no motion” net migrations observed in the surf zone were comparatively smaller than that of the offshore zone observations (94%). About 73% (713 of 971) of the munitions with “no motion” had $SG \geq 3$, implying that similar to the offshore zone, the “no motion” munitions tended to have higher density. The greatest net migration distances during the experiment were recorded in the surf zone with a maximum net migration distance of 40 m offshore (Figure 5.4).

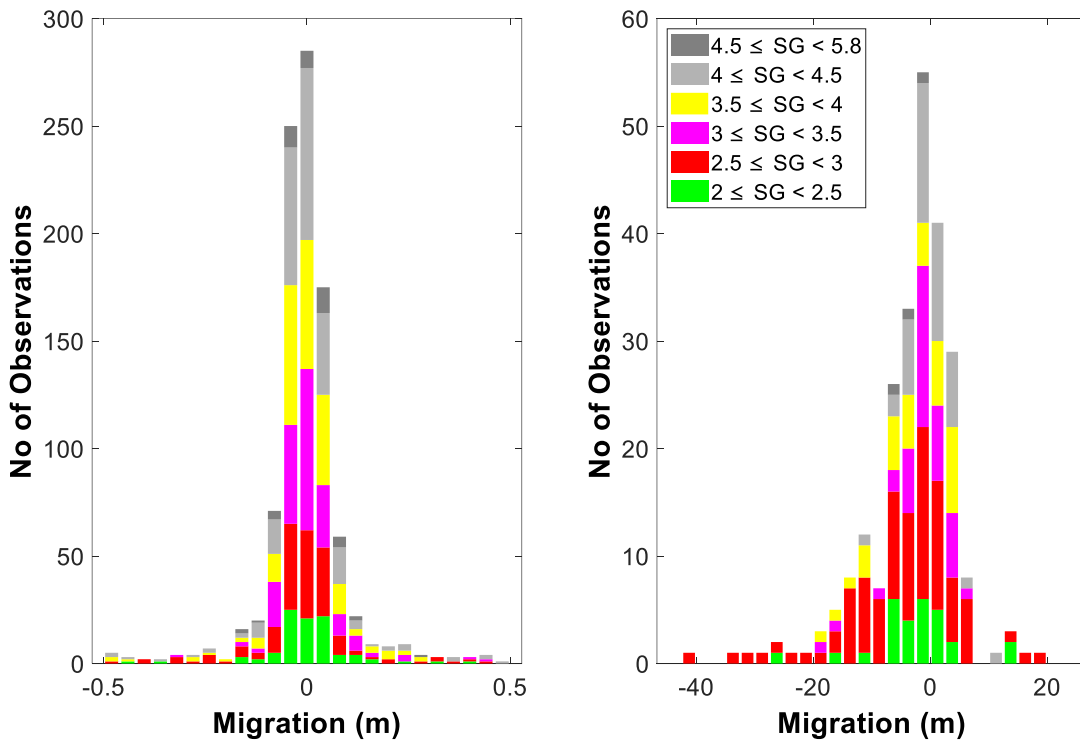


Figure 5.4: Migration distances for munitions in the surf zone. The left and right are the “no motion” and “motion” data, respectively.

About 50% (120 of 241) of the “motion” munitions had $SG < 3$, as compared to the offshore zone, which had a value of 83%. About 34% (83 of 241) of the “motion” net migrations were greater than the 5 m cutoff for what was considered a major migration. Thirteen percent (11 of 83) and 49% (51 of 83) of the major migration observations were in the $2 \leq SG < 2.5$ and $2.5 \leq SG < 3$ ranges, jointly accounting for 60% of the munitions with net migrations greater than 5 m. Net migration in the surf zone was predominantly offshore-directed 65% (157 of 241) as also shown in Figure 5.4 where the ‘motion’ migration histogram is left-skewed. This trend is in contrast with the offshore zone where net munitions migration was largely

onshore-directed and may suggest the importance of gravity (slope) on munitions migration.

Table 5.3: “No motion and “motion” values and percentages based on the (a) SG ranges and (b) cases (surf).

(a) SG Ranges	$2 \leq SG < 2.5$	$2.5 \leq SG < 3$	$3 \leq SG < 3.5$	$3.5 \leq SG < 4$	$4 \leq SG < 4.5$	$4.5 \leq SG < 5.8$	Total
No motion	10% (93)	17% (165)	21% (200)	23% (222)	25% (246)	4% (45)	971
Motion	12% (28)	39% (93)	17% (40)	14% (34)	18% (43)	1% (3)	241

(b) Cases	Case01	Case02	Case03	Case04	Case05	Case06	Total
No motion	88% (144)	71% (174)	70% (106)	86% (171)	86% (221)	79% (155)	971
Motion	12% (19)	29% (72)	30% (46)	14% (27)	14% (35)	21% (42)	241
Total	163	246	152	198	256	197	1212

The case-based migrations in the surf zone (Figure 5.5) had the “no motion” net migration following a nearly normal distribution and the “motion” net migrations left-skewed in favor of offshore migration. The “motion” exceptions are Case02, Case04, and Case06 with distributions more normal. The trend observed in the offshore zone persists in the surf zone, where Case03 had the relatively largest percentage of “motion” migration at 30% and the same migration pattern of (86%, 14%) for “no motion” and “motion” was observed for Case04 and Case05 (Table 5.3b). The largest migration distance of -40 m in the entire experiment also occurred during case03. The SGs of the “no motion” net migrations span the entire SG range from 2 to 5.8. A similar observation is made in the “motion” net migration, suggesting that hydrodynamics plays a more dominant role than munitions bulk density on migration in the surf zone, provided conditions are sufficient for migration to occur.

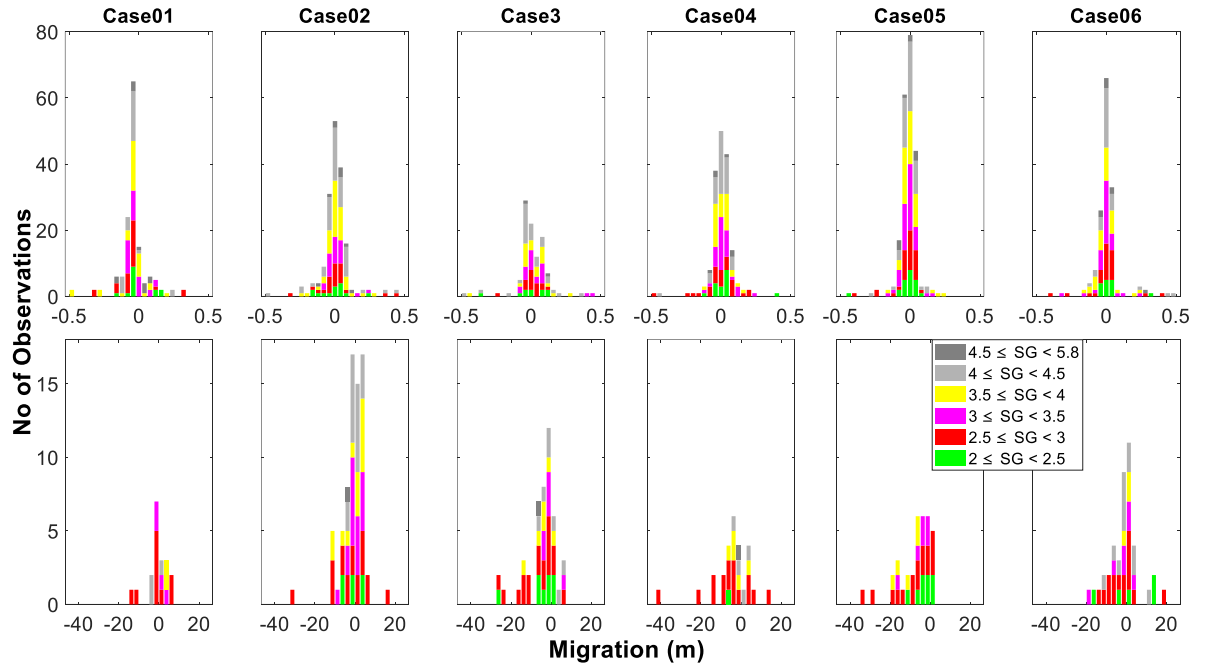


Figure 5.5: Migration distances for munitions in the surf zone separated into cases.
 The top and bottom rows are the “no motion” and “motion” data for each case, respectively.

5.2.4 Munitions migration in the swash zone

The swash zone extended from the farthest runup edge on the beach face to the surf/swash boundary. The boundary varied with trial from $x = 77$ m to $x = 97$ m due to the changing forcing conditions. The swash zone spans the shortest cross-shore distance of all three zones. The number of munitions initially deployed in the swash zone varied from 30 to 50 (19–32%) depending on the surf/swash boundary location. In addition to the exclusion of munitions that experienced no hydrodynamic forcing

from the dataset, some munitions with significant offshore migration distances initially deployed in the swash zone ended up in the surf zone in subsequent trials. Such datasets were subsequently considered as part of the surf zone categorization.

There were 204 total observations in the swash zone which comprised 144 (71%) and 60 (29%) observations for “motion” and “no motion”, respectively (Figure 5.6; Table 5.4a). Ninety-three percent (56 of 60) of the “motion” munitions had $SG \geq 3$, suggesting that hydrodynamics and morphodynamics may play a more dominant role than density on munitions migration in the swash zone for energetic conditions. The maximum net onshore and net offshore migration distances were 12 m and 17 m, respectively (Figure 5.6; Figure 5.7, Case06). The percentages of the munitions migrations in either direction were similar with 47% (28 of 60) migrating offshore and 53% (32 of 60) migrating onshore. These swash zone observations for the “motion” munitions suggest a nearly equal probability of munitions migration in either direction, but the offshore-directed migrations are likely to migrate farther distances (Figure 5.6, Case06). The spread of the migration percentages and no observable trends between net migration distance and the SG for the “motion” munitions suggest that SG plays a lesser role in the “motion” munitions migration when forcing conditions are sufficient to cause migration.

The “no motion” munitions accounted for about 71% (144 of 204) of the swash zone observations (Table 5.4; Figure 5.6). The increase in percentages with increasing SG indicates that denser munitions tend to experience “no motion” likely under weaker swash zone forcing. Approximately 92% of the “no motion” munitions had $SG \geq 3$, with the least dense munitions ($2 \leq SG < 2.5$) in the swash zone always migrating

beyond 0.5 m. The $SG \geq 3$ munitions accounting for 92% of the “no motion” observations suggest that the threshold SG for motion/no-motion in the swash zone may be within the range of 2 to 3.

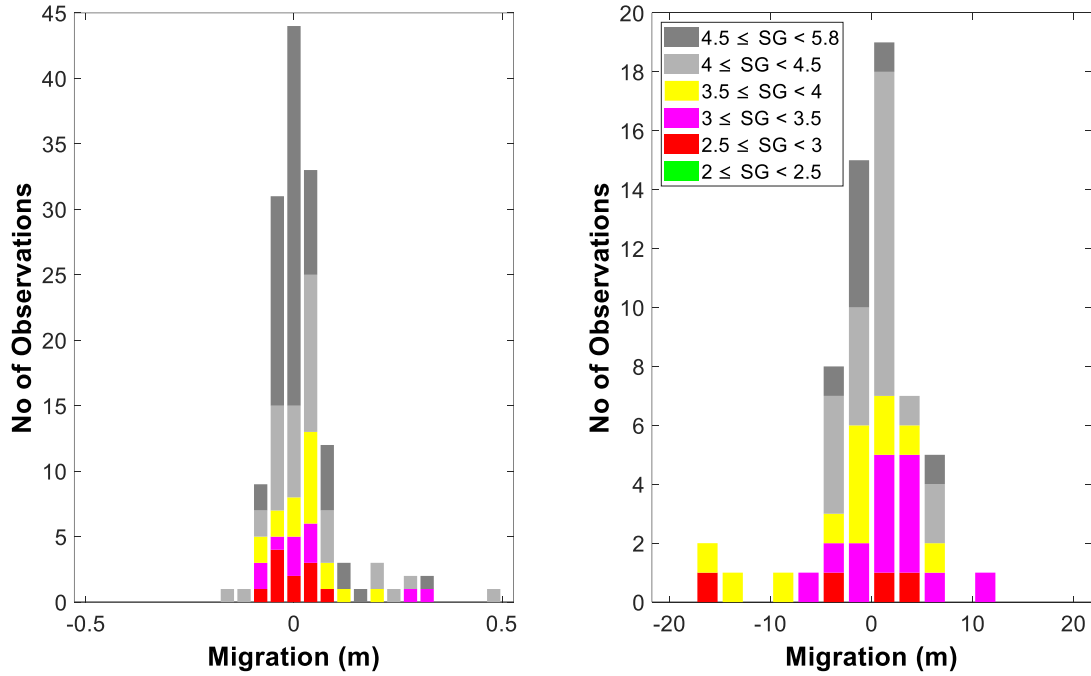


Figure 5.6: Migration distances for munitions in the swash zone. The left and right are the “no motion” and “motion” data, respectively.

The “motion” and “no motion” observations in the swash zone appear contrasting. On one hand, munitions bulk density suggests that denser munitions tend to experience “no motion.” On the other hand, SG seems to have minimal importance in the “motion” munitions, as there were no observable trends between net migration distance and the SG . The discrepancy between SG and migration in the “motion” and “no motion” datasets implies that SG is a key factor in the final determination of a munition experiencing “motion” or “no motion”, but the forcing is a more dominant

driver of migration than the bulk density in munitions that experience significant net migration.

Table 5.4: “No motion and “motion” values and percentages based on the SG ranges (swash).

(a) SG Ranges	$2 \leq SG < 2.5$	$2.5 \leq SG < 3$	$3 \leq SG < 3.5$	$3.5 \leq SG < 4$	$4 \leq SG < 4.5$	$4.5 \leq SG < 5.8$	Total
No motion	0% (0)	7.5% (11)	7.5% (11)	13% (18)	28% (40)	44% (64)	144
Motion	0% (0)	7% (4)	23% (14)	20% (12)	37% (22)	13% (8)	60
(b) Cases	Case01	Case02	Case03	Case04	Case05	Case06	Total
No motion	100% (2)	79% (46)	0% (0)	70% (23)	68% (60)	59% (13)	144
Motion	0% (0)	21% (12)	100% (1)	30% (10)	32% (28)	41% (9)	60
Total	2	58	1	33	88	22	204

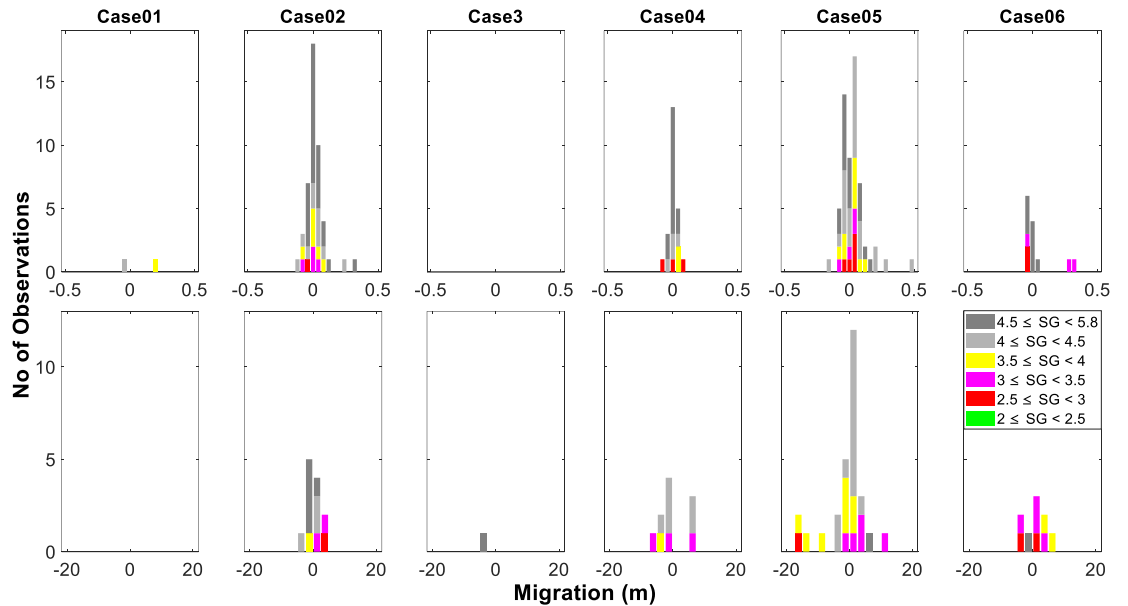


Figure 5.7: Migration distances for munitions in the swash zone separated into cases. The top and bottom rows are the “no motion” and “motion” data for each case, respectively.

The swash zone had the smallest number of munitions observations of all three zones largely because of the migration of many initially proud munitions into the other zones and the relatively smaller area of intermittent swash motions. Case05 had a large number of data points due to the greater number of trials. The observed trend between Case04 and Case05 in the offshore and surf zones was also maintained in the swash zone (Table 5.4b). A similar pattern of (70%, 30%) and (68%, 32%) for “no motion” and “motion” migrations were observed in Case04 and Case05, respectively (Table 5.4b).

The offshore migration of the berm between $x = 80$ m and $x = 90$ m for most cases (Figure 7) explains the inability to locate some of the munitions initially placed in the swash zone of the SG value. Hence, only a few or no data points were observed for some of the cases (Figure 5.7). The few data points observed in Case01 were due to the swash extents being farther away from the shoreline, and hence many deployed munitions in the zone did not experience hydrodynamic forcing. Conversely, the strong forcing combination in Case03 which led to offshore migrations of most munitions initially deployed in the swash explains why (Figure 5.7, Case03) is nearly blank.

As with the surf zone, the SG distributions of both the “no motion” and “motion” net migrations spanned the entire SG range from 2 to 5.8, suggesting the relative importance of hydrodynamics over munitions bulk density.

5.3 Dimensionless numbers and power-law relationships

The object mobility number (θ_m) and the shields number (θ) are two dimensionless numbers that have been related to munitions migration (Cristaudo & Puleo, 2020). The two dimensionless numbers associated with each munition were computed using the equations in section 3.4.2 using the different “ u ” types described in section 3.6.4. The θ_m and θ based on $u_{2\text{percent}}$ were used in this analysis.

The migration distances (“motion”) were plotted against the θ_m and θ (Figure 5.8). A wide scatter in migration is observed in both dimensionless numbers. The critical θ_m is a measure of the relationship between the object diameter and bed roughness (Friedrichs et al., 2018; Rennie et al., 2017) and since a wide range of munitions was deployed, the wide scatter may be expected. The θ embeds the impact of the hydrodynamics (τ_b, u) and the morphology (τ_b, d_{50}) which both impacted munitions behavior stochastically. The wide scatter observed aligns with observations from past studies showing a weak correlation between dimensionless parameters and migration distance (Cristaudo & Puleo, 2020; Friedrichs et al., 2018; Traykovski & Austin, 2017). However, a greater clustering of the less-dense munitions with green symbols ($2 \leq SG < 2.5$) occurred in the $\theta_m = 0$ to 2 and $\theta = 0$ to 5 and correspond with the greatest migration distances implying that the munitions with smaller SG may require weaker overall forcing for migration.

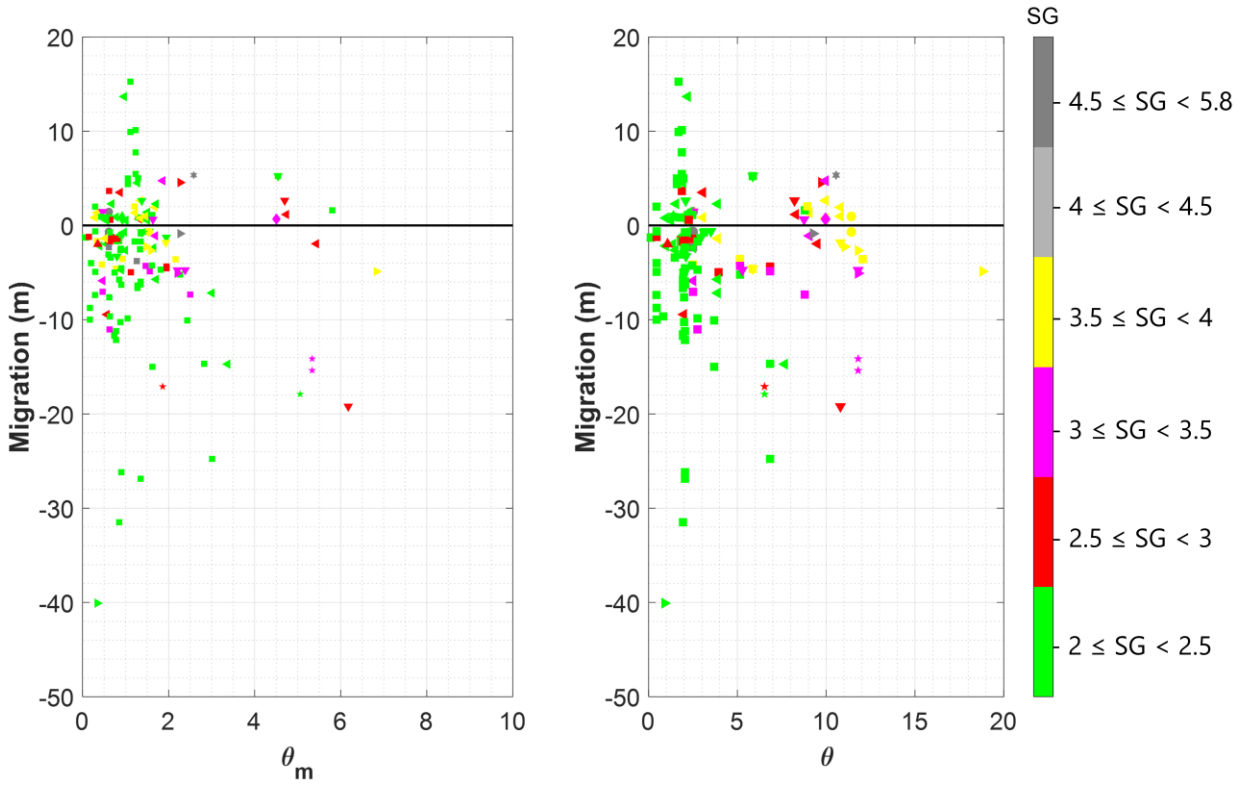
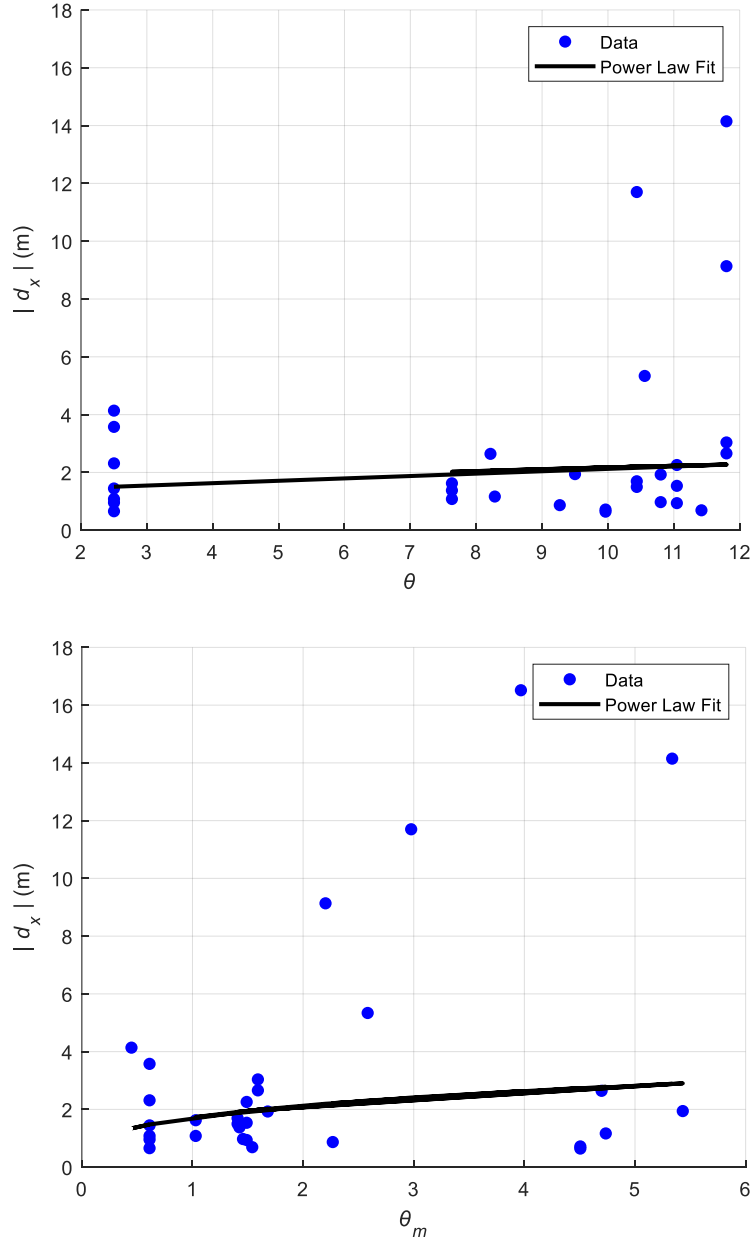


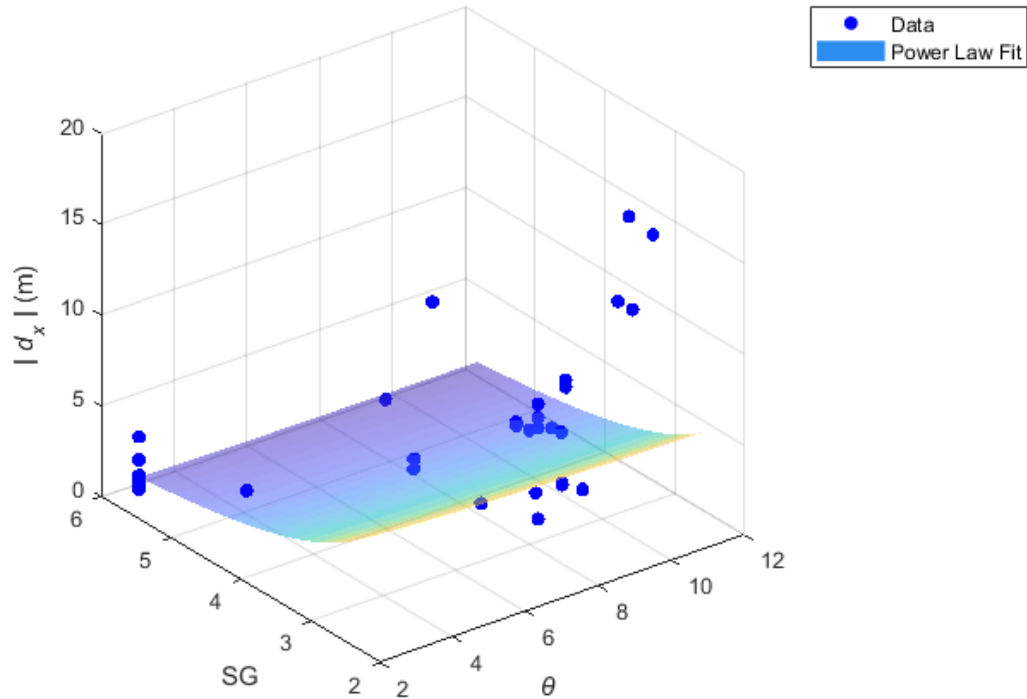
Figure 5.8: Migration as a function of Shields number for all motion observations. Positive and negative values represent onshore- and offshore-directed migrations, respectively. The symbol shapes represent the Cases. Case01 to Case06 are \circ , \square , \triangleright , \triangleleft , ∇ , Δ , respectively.

A prior study attempted to establish a power-law relationship between the absolute munition migration and the θ_m and θ using the nonlinear least squares regression analysis approach but insignificant R^2 values were obtained (Cristaldo & Puleo, 2020). The R^2 improved when the SG was incorporated ($R^2 = 0.27$). This $R^2 = 0.27$ is still low and implies low confidence in the model. Attempts were made to explore the same empirical relationships in all zones and combined, but the results of the analysis were poor. For instance, the swash $|d_x| = a_1 \theta^{b1}$ and $|d_x| = a_1 \theta_m^{b1}$ produced $R^2 = -0.06$ and -0.01 (Figure 5.9) where $|d_x|$ is the absolute migration

distance |Migration|. Negative R^2 can occur when the model does not follow the data trend and fits worse than a horizontal line (Figure 5.9).



Attempts were made to improve the model by incorporating the munitions intrinsic property – the SG , into the equations to produce $|d_x| = a_1\theta^{b_1}SG^{c_1}$ and $|d_x| = a_1\theta_m^{b_1}SG^{c_1}$. The models were slightly improved, resulting in $R^2 = 0.12$ [$a_1=3.286$, $b_1 = -0.089$, $c_1 = -1.667$] and 0.12 [$a_1=3.4898$, $b_1 = -0.142$, $c_1 = -1.883$], respectively (Figure 5.10). These R^2 values are still too low for the model to be robust.



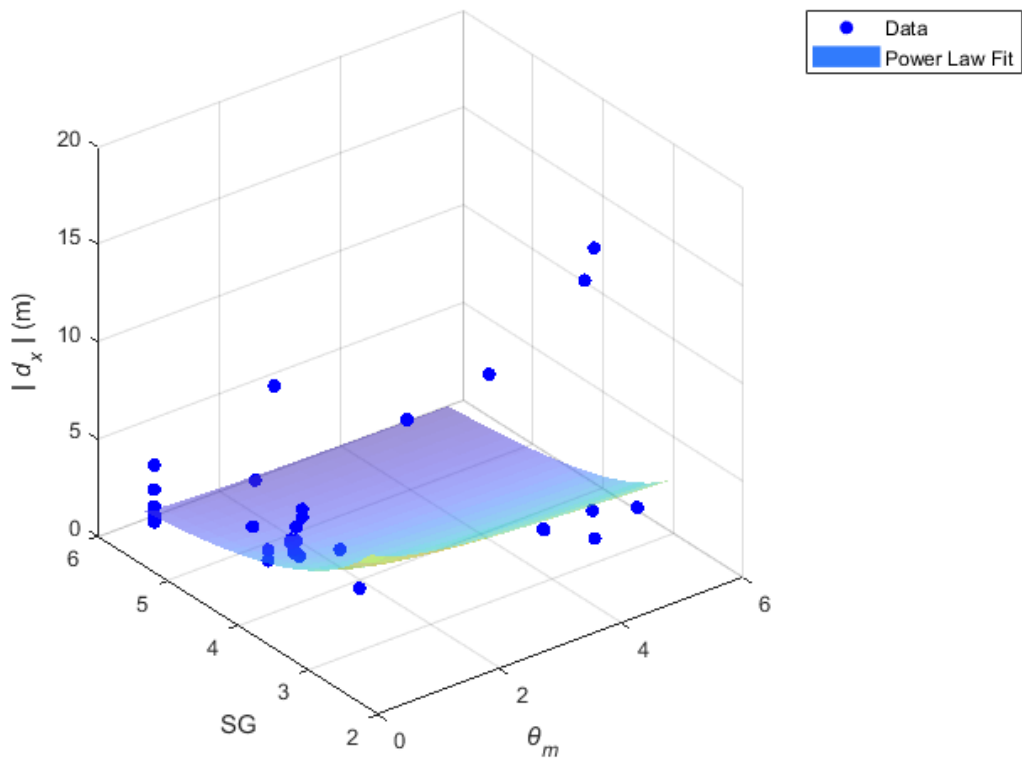


Figure 5.10: Power law fit of (a) $|d_x|$ versus θ, SG and (b) $|d_x|$ versus θ_m, SG in the swash zone.

Several other combinations were attempted but no $R^2 > 0.12$ was obtained which implied that the model barely improved and overall, the dimensionless numbers were insufficient for reliably describing or predicting munitions migration. Much poorer results were obtained for the other zones and across the entire cross-shore combined.

5.4 Near-instantaneous migration observations in the surf zone

5.4.1 Initiation of motion

The IMU data provided near-instantaneous observations of the munition migration in the surf zone. The interpretations of the observations with respect to the hydrodynamics and the beach slope in the vicinity of the munitions give insights into the complex interactions between munitions in the nearshore and the forcing conditions. The initiation of motion times of munitions at the same $x = 82$ m location relative to the start times of the wave maker ($t = 0$ s) for cases with available data are presented in Table 5.5. The munition types are described in the following order: color—munition type, e.g., R81 implies a Red 81 mm projectile (see Figure 3).

Table 5.5: Duration of time before initiation of motion due to the wave forcing relative to $t = 0$ s, the wave maker start time.

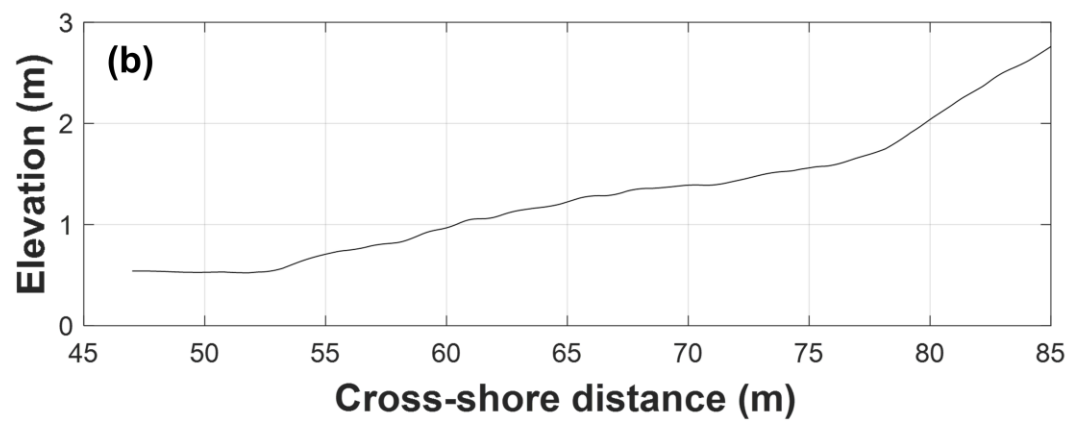
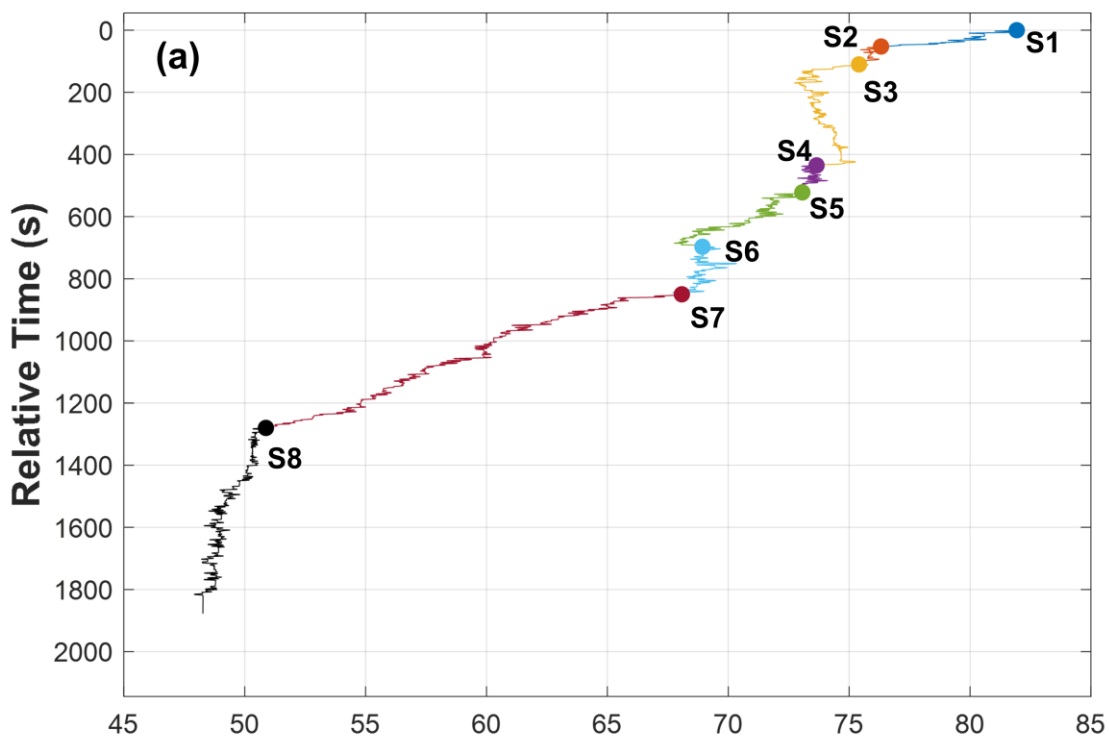
Experiment No	Munition Type, SG, and Initiation of Motion Time (s)		
Case02 Trial01	R81 ($SG = 2.5$) = 22.5	M81 ($SG = 3.0$) = 24.9	S81 ($SG = 4.18$) = 37.6
Case04 Trial01	R81 ($SG = 2.5$) = 87.4	No data	S81 ($SG = 4.18$) = 90.6
Case05 Trial01	M81 ($SG = 3.0$) = 12.1	Y81 ($SG = 3.5$) = 133.9	S81 ($SG = 4.18$) = 183.4
Case06 Trial01	R81 ($SG = 2.5$) = 45.6	No data	S81 ($SG = 4.18$) = 55.7

The wide-ranging time from forcing to “initiation of motion” (Table 5.5) was expected because the hydrodynamics of each case varied (Table 3.1). Across the cases shown, the less-dense instrumented R81 munition ($SG = 2.5$) consistently had shorter “initiation of motion” times than the instrumented S81 munition ($SG = 4.18$). This limited observation suggests that bulk density impacts the initiation of motion as less dense munitions of similar shapes and sizes are mobilized before the denser munitions originating from the same cross-shore position and under the same forcing. Conversely, overall hydrodynamics likely dominate over bulk density for munitions migration in the surf zone (Section 5.2.3) for long-distance migration.

5.4.2 IMU-derived near-instantaneous munition migration

The IMU data of a R81 munition ($SG = 2.5$) during Case02 Trial01 ($h = 2.87$, $H_s = 1.1$ m, $T_p = 6$ s) are presented to show the variability in the migration time history (Figure 5.11) where relative time (RTt) is referenced to a local time when the munition started to move. The overall duration of motion was about 31 min (1870s). The munition trajectory was divided based on observations of change in migration behavior.

Sections are numbered and color-coded (Figure 5.11) and examples include the change from offshore migration to roughly stationary or roughly stationary to offshore migration. The beach profile (Figure 5.11b) and corresponding water level variation within 120 s of change in migration behavior (Figure 5.11c–j) are also shown. Free surface oscillations (η) were taken from the sensor closest to the midpoint of the migration range of the particular section. From relative time RTt = 0 s to RTt = 53 s, the munition migrated 5.61 m offshore (S1; blue) at a mean velocity of 0.11 m/s. Sections S2 (orange), S4 (purple), S6 (cyan), and S8 (black) have relatively similar properties where the munition experienced a series of small onshore/offshore motions, likely mimicking the flow oscillations. Net migrations were S2 (0.91 m), S4 (0.56 m), S6 (0.86 m), and S8 (2.08 m) over durations of 57 s, 87 s, 153 s, and 496 s, respectively. The corresponding cross-shore mean migration velocities range from 0.004 m/s to 0.016 m/s offshore. In S3 (yellow), a rapid offshore migration (2.19 m) was followed by a gradual onshore migration (2.01 m) and another rapid offshore migration (1.56 m) over ~325 s (RTt = 110 s to RTt = 435 s), resulting in net migration of 1.75 m offshore.



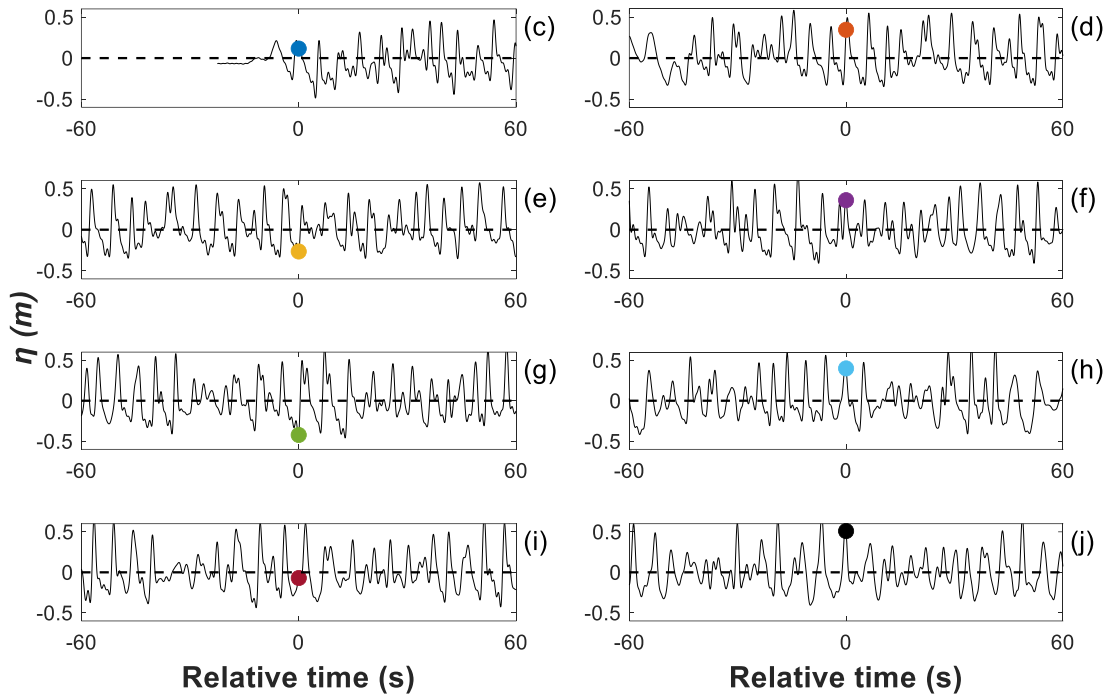


Figure 5.11: (a,b) The migration time history of an R81 ($SG = 2.5$) instrumented surrogate munition in the surf zone. Offshore migration is from right to left. The color changes depict the sectioning of the munition migration trajectory. The corresponding-colored circles indicate the start of each migration section. (b) The beach profile for reference. (c–j) Free surface oscillations (η) 60 s before and after the onset of the S1 to S8 centered around a local RTt = 0 s. The colors correspond with the colors used for S1 to S8 in Figure 5.11a.

Conversely, S5 (green) from RTt = 522 s to RTt = 697 s initially started with onshore/offshore oscillations similar to S4 that led to a short net migration distance, then gradually migrated offshore before rapidly migrating back onshore in the last few seconds. The resulting mean migration velocity was 0.02 m/s. Section S7 (red) from RTt = 850 s to RTt = 1280 s experienced 17.20 m of offshore migration and a corresponding mean migration velocity of 0.04 m/s. These data show that munition migration varies considerably across the profile and with time of forcing.

Local hydrodynamics and bed slopes provide context for some of the tendencies of the behavior. The initiation of motion (S1) may have been triggered by a wave crest just before the start of a wave group, suggesting that the initial motion may not occur under the largest waves in the group. Transitions to S2, S5, S7, and S8 occurred inside wave groups with S2 and S8 initiated near wave crests, while S5 and S7 were initiated near wave troughs (Figure 5.11d,g, i,j). S3, S4, and S6 were initiated towards the end of a wave group with S3 near a trough, while S4 and S6 were near wave crests (Figure 5.11e,f,h). The different hydrodynamic conditions under which the sections were triggered suggest that changes in the behavior of munitions migration and trajectories are not tied solely to peak hydrodynamic conditions. Note that the discrepancies in the positions of the symbol on the waveforms in the subplots are due to the relative distances between the UDM sensors and the munitions locations. The rapid migration observed in S1 was likely aided by the local steep slope (1:8.5) between $x = 76$ m and $x = 82$ m. The observations in S2, S3, S4, and S5 from RTt = 53 s to RTt = 697 s coincide with a gentler beach slope (1:30) that had some portions characterized by local troughs or small negative slopes. Due to the gentle slope, local hydrodynamics might have been more dominant in the three sections, but the gentle slope could have aided the observed onshore migration under skewed waves. In S7 (RTt = 850 s to RTt = 1280 s), the beach slope was steeper (1:17) from $x = 53$ m to $x = 62$ m, and the corresponding response on the munition migration was a burst of offshore migration over a relatively short time where the munition traveled 12 m offshore in 390 s (~890 to ~1280 s). From RTt = 1280 s to RTt = 1776 s, the munition entered the flat slope region from $x = 53$ m to the offshore. The migration speed and distance reduced, suggesting a dominant influence of the slope on the net

migration. In the region, repeated onshore/offshore vacillation suggests that the munition may have been trapped in a local depression or developed a local scour hole, allowing for only restricted horizontal motions. The free surface oscillation observations (Figure 5.11c–j) may suggest more of a cumulative effect of the larger wave groups than the individual waves that led to the S1–S8 observations.

Deployed sensors were fixed in space, whereas the munition migration is Lagrangian. Thus, hydrodynamic statistics (Table 5.6) were calculated for the duration of the identified sections using the sensor located nearest the mean munition location. The local skewness (S_k) and asymmetry (A_S) were quantified from free surface oscillation η (Elgar & Guza, 1986) and expressed as

$$S_k = \frac{\langle \eta^3 \rangle}{\langle \eta^2 \rangle^{3/2}} \quad \text{Equation (5.2)}$$

$$A_S = \frac{\langle H(\eta)^3 \rangle}{\langle \eta^2 \rangle^{3/2}}, \quad \text{Equation (5.3)}$$

where H is the imaginary part of the Hilbert transform and $\langle \rangle$ denotes time averaging.

Table 5.6: Computed hydrodynamic parameters during each section of the migration.

Sections	UDM No	UDM Location (m)	H_s	S_k	A_S
S1	8	77	0.81	0.53	-0.03
S2	8	77	0.92	0.75	-0.60
S3	7	72	0.86	0.75	-0.51
S4	7	72	0.83	0.50	-0.41
S5	7	72	0.90	0.68	-0.29
S6	6	67	0.86	0.58	-0.48
S7	5	57	0.87	0.52	0.05
S8	3	47	0.83	0.79	0.06

An increase in wave non-linearity is denoted by wave skewness becoming more positive and asymmetry becoming more negative. Durations of nearly stationary

motion (S2, S4, S6, and S8) have S_k ranging from 0.5 to 0.79, indicating that there is still moderate to strong onshore skewness; possibly balanced by profile slope. Corresponding asymmetries range from -0.6 to 0.06, indicating moderate asymmetry. The positive asymmetry in A_s may be due to the waveform adjusting as it came off the wave paddle. Offshore migration sections S1, S5, and S7 had S_k from 0.52 to 0.68 and A_s from -0.29 to 0.05. The onshore migration section, S3, had the second largest S_k of 0.75 and A_s of -0.51. These data suggest that wave skewness and asymmetry alone are insufficient to identify munition migration and/or migration direction.

The impact of bulk density on migration distance and duration was explored by comparing the three 81 mm munitions with $SG = 2.5$ (R81), $SG = 3$ (M81), and $SG = 4.18$ (S81) (Case02 Trial01, Figure 5.12). Marked differences were observed between the munitions: 1) The least dense R81 ($SG = 2.5$) had more observations (79) and the largest magnitudes of migration observations. The mean and standard deviation (std) values of the absolute motion distances were 0.53 m and 0.79 m, and 13 of the 14 absolute motion distances greater than 1 m across all three munitions were for R81 observations. 2) The most dense S81 ($SG = 4.18$) had the fewest observations of motion (5) and the distance magnitudes (mean = 0.45, std = 0.29) were the smallest. 3) The moderate density M81 ($SG = 3.0$) experienced moderate motion events (7) and the mean and std values of the absolute motion distances were 0.47 m and 0.76 m. The mean values of the gross motions were R81 = 2.69 m, M81 = 0.92 m, and S81 = 1.03 m, as compared to the mean values of the net motions of R81 = 0.53 m, M81 = 0.47 m, and S81 = 0.45 m. These findings indicate the munitions are likely to oscillate onshore and offshore superimposed on a mean transport direction.

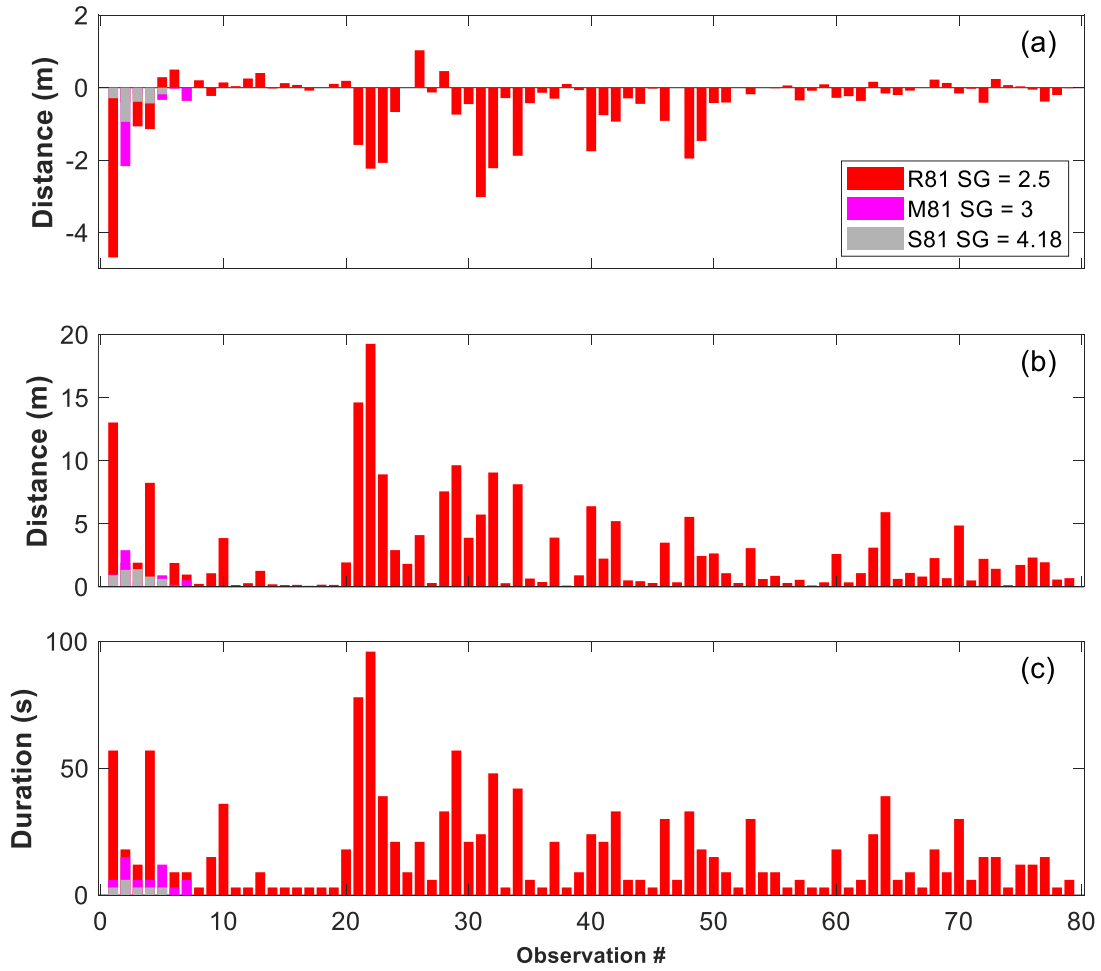


Figure 5.12: Migration distance as a function of observation of a 81 mm projectile with $SG = 2.5$ (R81), $SG = 3.0$ (M81), and $SG = 4.18$ (S81), (a) net migration, (b) gross migration, and (c) duration of the migration expressed in (a). Color coding is relative to Figure 3.11.

Offshore motions for the instrumented 81 mm munitions dominated regardless of SG with 100%, 100%, and 70% (55 of 79) of the R81, M81, and S18 events, respectively, being offshore-directed (a). The corresponding durations of motion (Figure 5.12c) also show that the R81 was the most active, followed by the M81 and

the S81. The most dense munition (S81) experienced the smallest “motion” durations with mean and std values of 3.6 s and 1.4 s, respectively (Figure 5.12c). The offshore dominance matches surf zone observations for the larger dataset (Figure 5.4) and further indicates the importance of beach slope on munitions migration.

5.5 Influence of munitions shape and initial orientation on migration

Munitions of varying bulk densities deployed at stations 8, 9, and 10 in the surf zone of the wave flume (Figure 5.13) were explored. The wave energy progressively increased from station 8 to station 10, implying an increase in wave impacts on the munitions from one station to the next.. Station 8 ($x = 52$) munitions deployment in the cross-shore location focuses on the probable role of shape on object migration. Station 9 ($x = 57$) and station 10 ($x = 62$) explore the roles of shape and initial orientation on object migration (Figure 5.13).

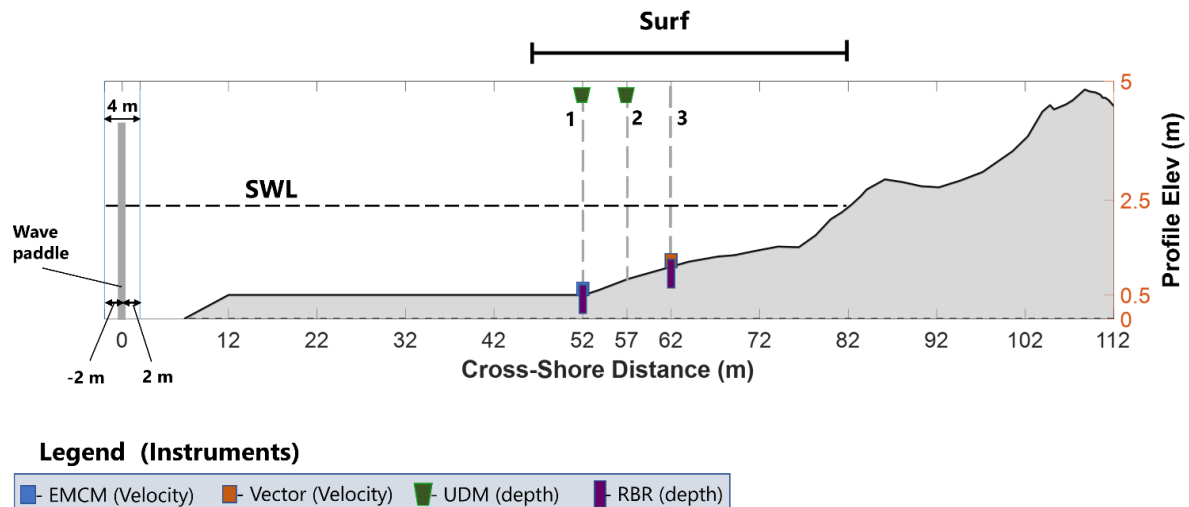


Figure 5.13: The cross-shore locations of stations 8, 9, and 10 in the surf zone of the wave flume.

The net migrations of the munitions at the end of each case were observed. The net migrations are the cumulative migrations obtained by subtracting the pre-trial locations from the final locations of the munition after each case as explained in section 5.2.



Figure 5.14: Munitions deployed at the three stations, Station 8) $x = 52$ m focuses on the influence of shape on migration by comparing cylinders and Rockets; Station 9) $x = 57$ m focuses on the influence of shape and initial orientation on migration by comparing cylinders and spheres; and Station 10) $x = 62$ m focuses on the influence of shape and initial orientation on migration by comparing surrogate 81 projectiles with noses, without noses, and without tails

5.5.1 Station 8 (shape)

The role of shape on munitions migration was explored by pairing canonical cylinders and hydra rockets (RKTs) of similar SG values at three alongshore positions (Figure 5.14a). The SGs of the three pairs of munitions were 2, 2.5, and 3. The CYL and RKT both have a D of 0.07 m but slightly different L of 0.420 m and 0.405 m, respectively (Figure 3.11). The impact of the length is likely negligible in comparison

to the shape impacts. The CYL takes on the symmetric form of a typical cylinder and therefore the center of gravity is closer to the geometric center, regardless of the orientation in space. Hence, the force balance around the object will tend to provide better stability against fluid flow. Conversely, the RKTs have cone-like tips and irregular bases, which tend to impact the center of gravity and the force balance, providing smaller resistance to the fluid flow in comparison to a more symmetric cylinder of similar cross-sectional diameter. Additionally, the shape differences lead to slightly different scour processes around the munitions. The scour buildups around the RKTs are generally more uneven, making it easier for fluid action to move the munition in comparison to the CYLs where scour processes tend to be more even and symmetric around the object. Hence, in nearly all the cases across all SG pairings, the CYL experienced relatively smaller net migrations (Figure 5.15) than the RKTs most likely due to the shape differences. Across SG values, the $SG = 3$ munition pairs recorded smaller net migration distances than the $SG = 2.5$ (Figure 5.15). However, an anomaly is observed in the $SG = 2$ munition pairs where the net migration distances recorded were smaller than the distances recorded in the $SG = 2.5$ and $SG = 3$ munition pairs. Smaller SG values would logically produce larger net migration values but in the case of the $SG = 2$ munition pairs, the net migrations were smaller. The possible reason is that the munitions were light enough to migrate with fluid flow, and therefore migrate onshore with the onshore flow, immediately followed by a relatively equal offshore migration leading to a small net migration at the end of the trial. Munition migrations were also mostly offshore-directed (Figure 5.15), which is consistent with the overall observations of munitions migration in the surf zone (Section 5.2.3).

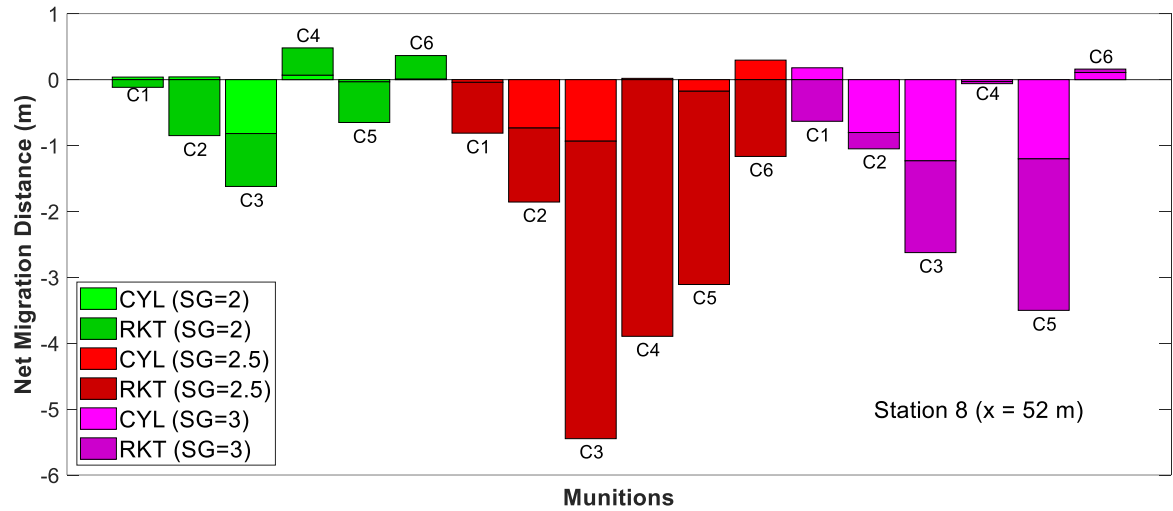


Figure 5.15: The munition pairs versus their net migration at the end of each case from case01 to case06 at station 8.

5.5.2 Station 9 (Shape & orientation)

At station 9, two sets of a sphere and two cylinders oriented streamwise and spanwise of the same SG values were deployed (Figure 5.14b). The SG values were 2.5 and 3.5, respectively. The two categories of SG s, $SG = 2.5$ and the $SG = 3.5$ each contain three munitions- one SPH and two CYLs. One of the CYLs was oriented spanwise and the other streamwise. Hence, the shape and initial orientation are two parameters being varied. Although the grouped munitions have similar SG s, the D of the sphere (0.099 m) is 40% larger than the D of CYL (0.07 m). The length to diameter ratios (L/D) are also different due to the shape difference with values of 1 and 6 respectively for SPH and CYL, respectively (Figure 3.11). The $SG = 2.5$ recorded net migrations mostly greater than 0.5 m while the $SG = 3.5$ were mostly less

than 0.5 m (Figure 5.16), suggesting the role of bulk density on munitions migration. This is also consistent with the observations in station 8 where $SG = 2.5$ experienced greater net migrations than the $SG = 3$ munitions (Figure 5.15), further highlighting the possibility that there is a certain SG threshold below which munitions migrate with fluid flow as observed in the $SG = 2$ munitions in Figure 5.15. Like station 8, most munition migrations were also offshore-directed which is consistent with the overall migration trends in the surf zone.

The shape did not seem to impact the net migration. No definitive trends were observed between the net migrations of the SPHs and CYLs. In terms of initial orientation, no definitive trend was observed in the $SG = 2.5$ and $SG = 3.5$ munitions (Figure 5.16). The inconsistent behavior suggests that initial orientation might play a minor role in munitions net migration, especially in the energetic surf zone.

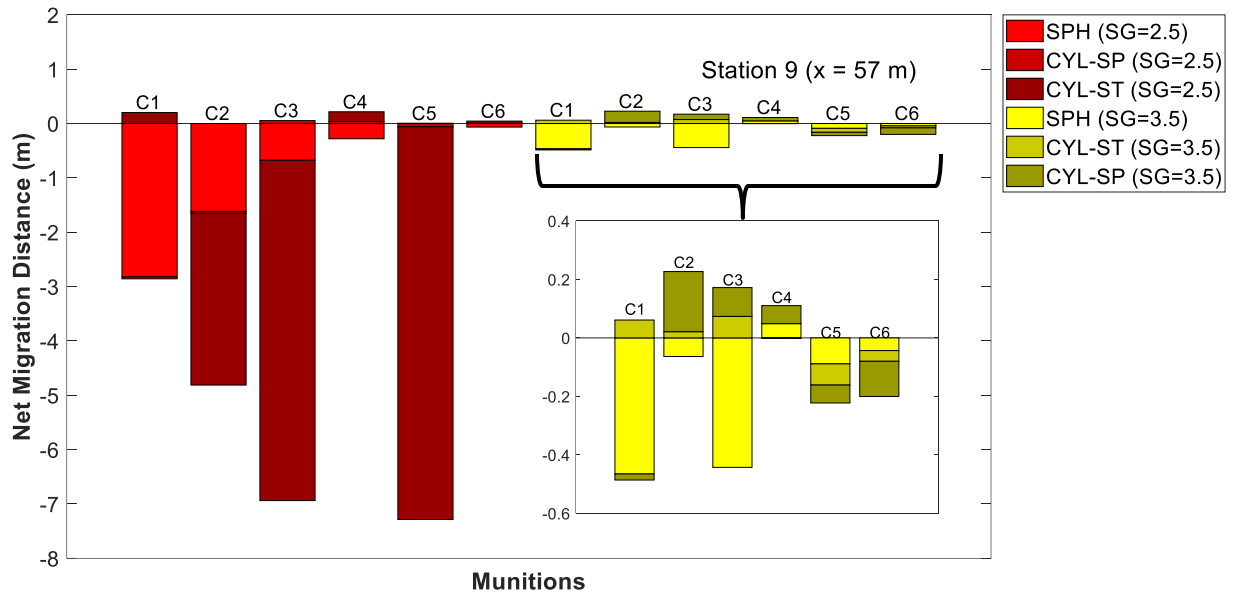


Figure 5.16: The munition pairs versus their net migration at the end of each case from Case01 to Case06 at station 9. SP = spanwise and ST = streamwise.

5.5.3 Station 10 (Shape & initial orientation)

Station 10 also focuses on shape and initial orientation just like station 9, but there is greater wave action and turbulence in this position. Three types of 81 mm projectiles with $SG = 4.18$ were deployed (Figure 5.17). The three munition types are (1) the 81 mm projectile with a pointed cone tip and fin base, (2) the flat-headed 81 projectile with fin base, and (3) the finless cone-tipped 81 mm projectile now code-named 81fin, 81flatTip and 81finless, respectively. The three types of 81 mm mortars exhibited different net migration behaviors. Overall, the munitions had small net migration mostly < 0.5 m except for a few due to the large bulk density, regardless of the shape and initial orientation (Figure 5.17). This suggests that bulk density is a dominant driver of munitions migration. However, the shape seemed to have some influence.

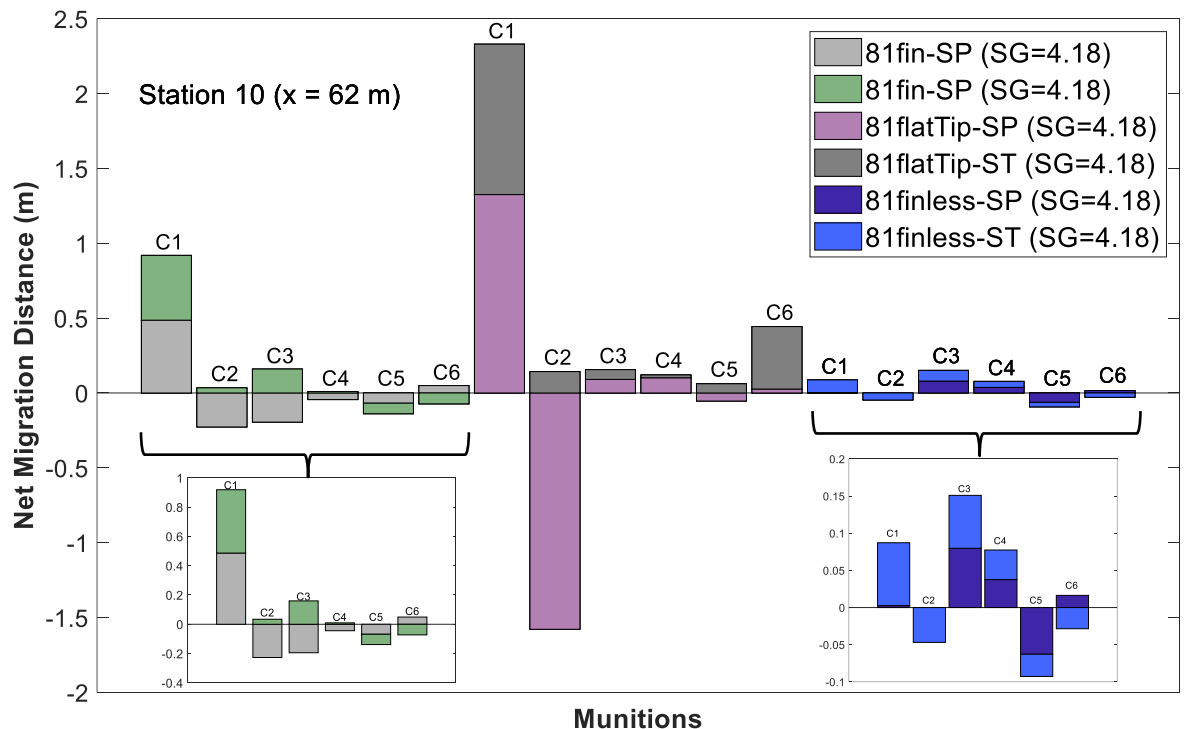


Figure 5.17: The munition pairs versus their net migration at the end of each case from case01 to case06 at station 10. SP = spanwise and ST = streamwise.

The 81flatTips tended to experience a greater net migration than the others and the 81finless the least. The flat nature of the tips of the 81flatTip seemed to provide more symmetry and even distribution of the forces than the others, thereby improving the chances of translational movement. On the other hand, the relatively smaller migration distances recorded in the 81finless could be due to a greater tendency for rotational movement about the base axis as illustrated in Figure 5.18.

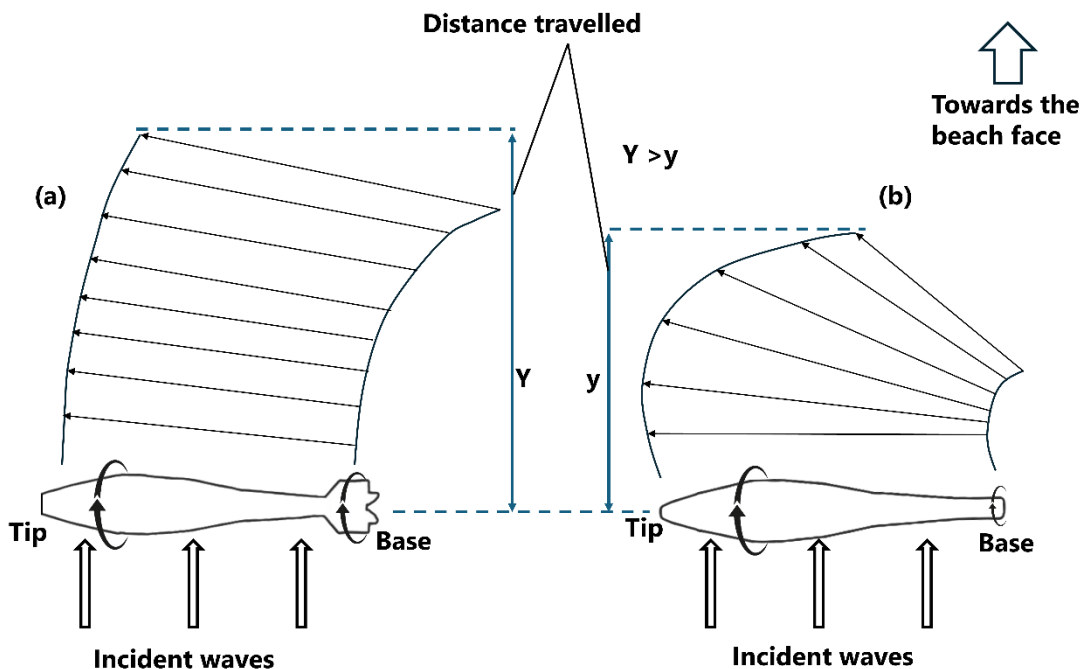


Figure 5.18: Migration dynamics of two 81 mm projectile types, (a) is the flat headed 81 mm projectile with a fin-like base and, (b) the fin-less 81 mm projectile.

Although the sketch is a simplification of how the two 81 mm projectiles respond to a wave impact, it does depict how the tendency to rotate more around an axis (the base) can shorten the translational distance covered. When repeated over

several waves the cumulative effect is likely to compound and result in a large difference in the overall migration distance covered. Hence, the shape has some influence on the net munition migration. Across the different initial orientations, there were no obvious trends in the net migrations as the initially spanwise munitions experienced greater net migration in some cases and smaller in other cases across all 81 mm projectile munition types (Figure 5.17). Initial orientation seems to have negligible impact on munitions net migration in this station and this is likely due to the greater intensity of wave action which tends to dominate over initial orientation.

Based on the observations across all three cross-shore positions, bulk density has been shown to remain as the dominant driver of net migration over shape and initial orientation. Shape may exert some influence, especially when there is a big difference in the symmetry which influences the force balance around the munition. Initial orientation exerts the least impact, especially under high energetic conditions of the surf zone.

Chapter 6

MUNITIONS BURIAL IN RESPONSE TO THE VARIED FORCING CONDITIONS

6.1 Introduction

Numerous studies exist on the burial dynamics of underwater objects within the size range of the munitions under study; scour and burial around short cylinders under oscillatory flows (Cataño-Lopera et al., 2007; Demir & García, 2007; Rennie et al., 2017) and combined flows (Cataño-Lopera et al., 2007; Cataño-lopera & García, 2006; Cataño-Lopera & García, 2007), short cylinders under progressive shoaling waves (Voropayev et al., 2003a), burial and scour around conical frustums under combined flows (Cataño-Lopera et al., 2011), scour and burial of piles and pipelines under combined waves (Sumer et al., 2001; Sumer & Fredsøe, 2001), mine burial and scour under energetic surf conditions (Traykovski et al., 2007), spherical bodies under steady flows and currents (Truelsen et al., 2005), and munitions in the surf and swash zone under waves (Cristaudo & Puleo, 2020). Some studies have also aggregated burial datapoints from different studies mostly under steady flow oscillatory waves (Friedrichs et al., 2016, 2018). There have been many more studies on burial than migration but many of the studies were in the deeper underwater zones with minimal wave transformation processes typical of nearshore environments like wave breaking. This study generated a larger number of burial datapoints than what is obtainable in previous studies across the entire cross-shore. The aggregation of the large datasets

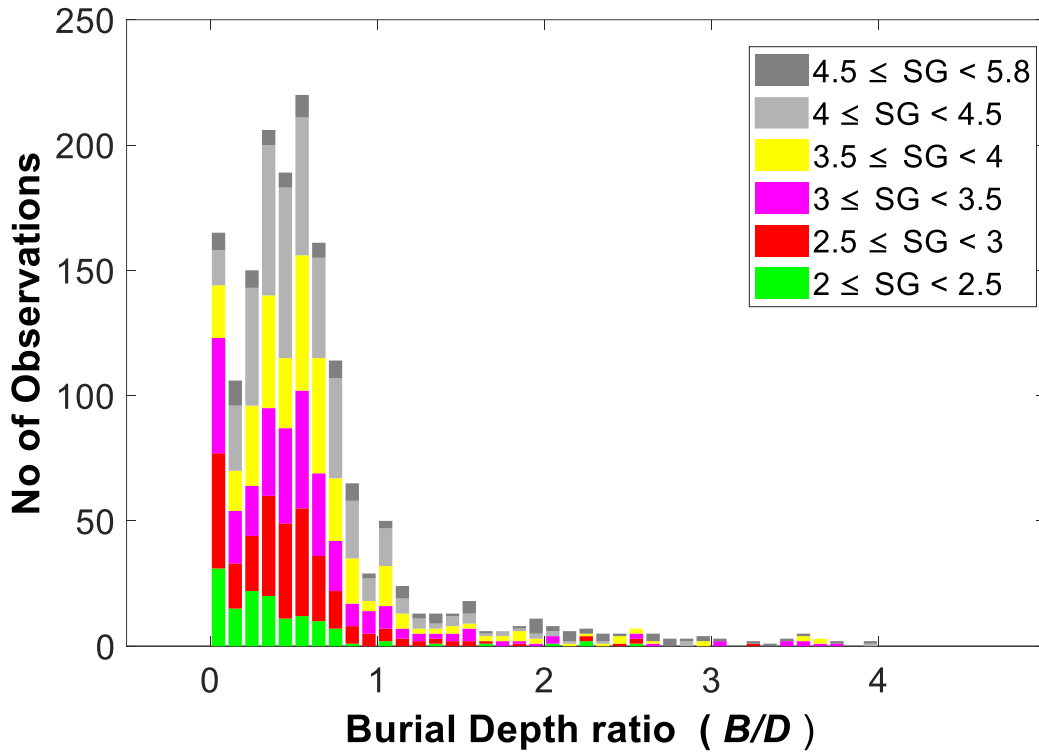
obtained helps provide probabilistic insights into the nature of objects burial in the nearshore.

6.2 Bulk description of munitions burial in the nearshore in response to the controlled forcing conditions

The munitions vary widely in bulk density values (2000 kg/m^3 to 5720 kg/m^3) and in sizes. The lengths of the smallest and largest munitions deployed were 0.20 m and 0.754 m for the 40 mm and 155 mm projectiles, respectively. Hence the burial was normalized by dividing the burial by the cross-sectional diameter of the munition to obtain the dimensionless burial depth ratio (B/D). A B/D of 1 implies that an initially proud munition achieved full burial and values >1 suggest burials greater than the cross-sectional diameters of the munitions. The B/D histograms of the “no motion” munitions were obtained (Figure 6.1). Like the migration analysis, munitions that did not receive any wave action during the experimental runs were excluded from the analysis. Few outlier data with $B/D > 5$ values were also excluded as measurement errors because the majority of them were lost munitions that were later found after several trials and rough estimates of their burial values were added manually. It was also difficult to know which trial hydro condition to associate with such a burial dataset. Overall, 1645 burial observations across the cases from case01 to case06 were recorded.

Figure 6.1 shows that the B/D ranges from 0 to 4.74, where 0 values imply that the munition remained proud after the trial run. Eighty-seven percent (87%; 1439 of 1645) of the B/D values fall within the 0 to 1 range. This suggests that most

initially proud munitions become partially buried or at most become fully buried just below the surface. No clear trends can be observed between the B/D and the SG values as each B/D bin has all SG values represented (Figure 6.1).



observed between the two zones. In the surf zone, no definitive trends were identified between B/D values and bulk density (Figure 6.2b). The SG values of the munitions encompassed the full range from the smallest to the largest SG values, suggesting that far-field processes exert a stronger influence on burial than the bulk density of the munitions.

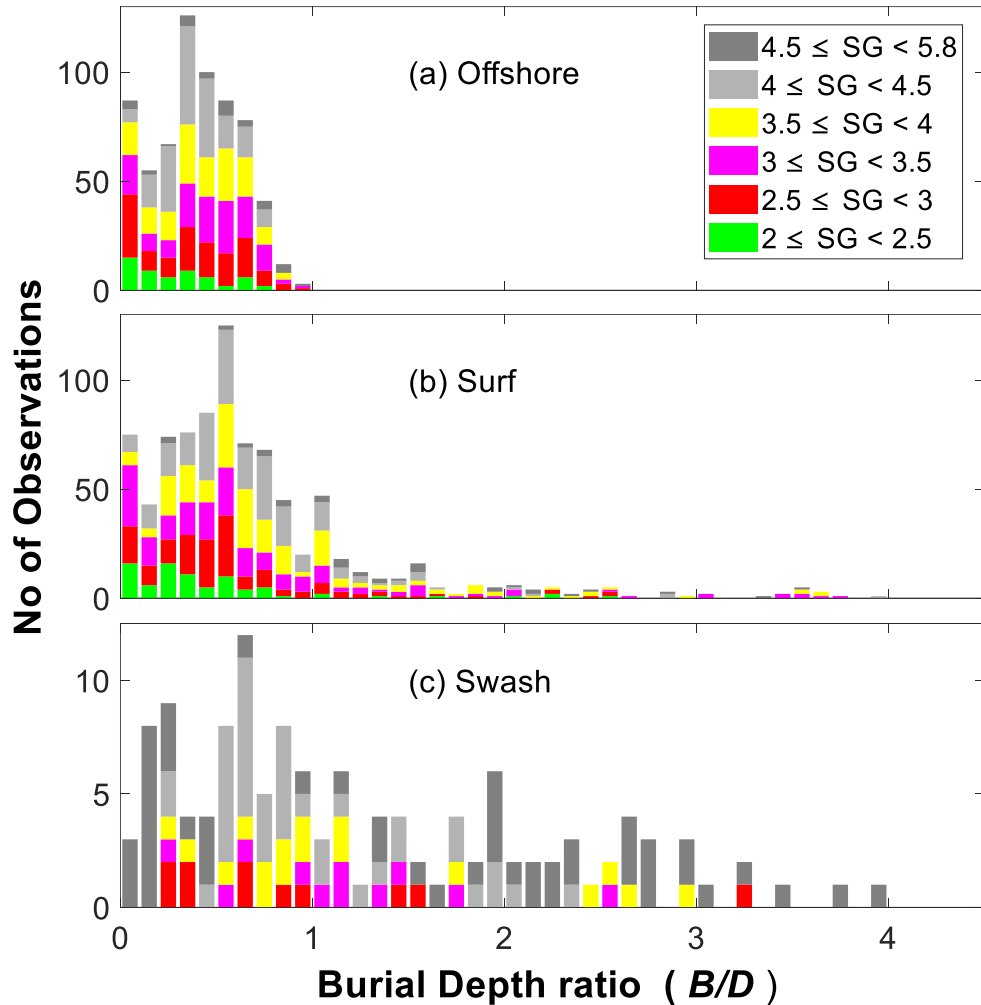


Figure 6.2: The B/D against the number of observations in the (a) offshore, (b) surf, and (c) swash zones.

Conversely, 92% (118 out of 129) of the B/D data points in the swash zone had $SG \geq 3$, indicating the dominance of munitions bulk density over hydrodynamic forces. Relatively fewer burial data points were observed in the swash zone compared to the other two zones. A substantial proportion of the data points involved heavier munitions with $SG > 3$ (Figure 6.2c). The broader context suggests that many of the less-dense munitions initially deployed in the swash zone migrated into the surf zone or further offshore, which explains the relatively lower number of B/D observations in the swash zone.

6.3 Morphodynamics and munitions burial/exposure

The $\Delta B/D$, the change in relative burial depth, was plotted against the normalized profile change between the trials ($\Delta z/D$) and arranged based on cross-shore regions (Figure 6.3). The beach profile changes obtained were from $x = 30$ m onwards to the beach face. There were no Δz measurements to obtain $\Delta z/D$ at the $x = 0$ m to the $x = 30$ m region and therefore, all $\Delta B/D$ in the zone were excluded from the analysis. A total of 1335 burial/exposure data points with their corresponding $\Delta z/D$ were obtained. The discrepancy between this value and the 1645 obtained in section 6.2 was due to the exclusion of data points between $x = 0$ m and $x = 30$ m.

Each panel (Figure 6.3) was split into four quadrants (I, II, III, IV) describing $\Delta B/D$ versus $\Delta z/D$ in terms of burial/exposure and erosion/accretion relationships as

Quadrant I: Munition burial and beach accretion. This condition may be expected as sediment is deposited causing the munition to become covered. The observations of

munitions burial and beach accretion were: offshore zone 110/345 (32%), the surf zone 332/861 (39%), and the swash zone 70/129 (54%).

Quadrant II: Munition burial and beach erosion. This condition may be unexpected since erosion of sediment would be expected to cause munition exhumation. The observations of munitions burial and beach erosion were: offshore zone 113/345 (33%), the surf zone 264/861 (30.5%), and the swash zone 24/129 (18.5%).

Quadrant III: Munition exposure and beach erosion. This condition matches expectations for far-field dominance of erosion leading to exposure. The observations of munitions exposure and beach erosion were: offshore zone 48/345 (14%), surf zone 127/861 (14.5%), and swash zone 24/129 (18.5%).

Quadrant IV: Munition exposure during accretion. This condition is unexpected for a stationary munition when sediment is deposited. The observations of munitions exposure and beach erosion were: offshore zone 74/345 (21%), the surf zone 138/861 (16%), and the swash zone 11/129 (9%). The largest magnitudes of munition were observed in the surf zone, with values in the range of -4 and 4 (Figure 6.3b). Conversely, over 95% of the values in the offshore zone were between -1 and 1 (Figure 6.3a). The “no motion” munitions in the swash zone (Figure 6.3c) were the high-density munitions with *SG* generally greater than 4.

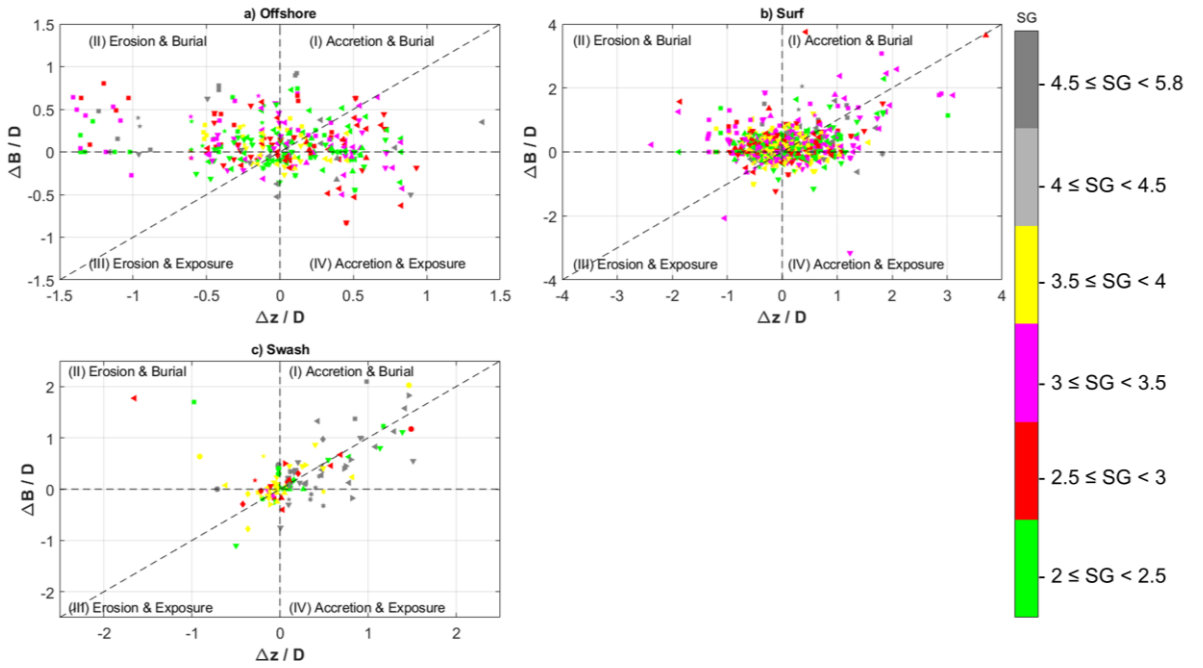


Figure 6.3: a-c) Dimensionless relative burial depth change versus relative profile change for the offshore (a), surf (b), and swash zones (c). The symbols represent the Cases. Case01 to Case06 are \circ , \square , \triangleright , \triangleleft , ∇ , Δ , respectively.

Only weak beach profile change was experienced in the offshore zone (Figure 6.3a), and munition $\Delta B/D$ values were equally small. In the surf zone and to a lesser extent the swash zone where accretion and erosion occurred, the magnitudes of $\Delta B/D$ were relatively larger suggesting that munition burial is affected by morphodynamics (far-field) in addition to the downward vertical movement of the munitions due to self-weight (near-field) and the hydrodynamics-driven force balance on the munitions. For instance, in the swash zone, the impact of SG on burial becomes more obvious as Quadrant I has a higher proportion of silver and dark silver symbols spanning the space (Figure 6.3c) indicating that more dense munitions experience greater burial.

6.4 Dimensionless numbers and empirical relationships

The Keulegan-Carpenter number (KC) and the shields number (θ) are related to objects burial under wave conditions (Sumer & Fredsoe, 2002) and widely applied in the objects burial studies earlier cited at the beginning of this chapter. Burial data (exposure data excluded) were plotted against the KC and θ (Figure 6.4) to identify potential trends. The excluded exposure data are the data points with $B/D < 0$. KC numbers span from approximately 10 to 1000 with burial depth ratios ranging from nearly proud to roughly $B/D = 5$. The dashed lines (Figure 6.4a) represent empirical relationships from a broad data set (Friedrichs et al., 2016) for cylinders (top dashed line) and conical frusta (bottom dashed line) with waves only and well offshore of breaking. Only about 50% (800 of 1589) of the dataset fell between the two dashed lines, further suggesting the difficulty in obtaining empirical relationships between munitions burial and the dimensionless numbers. Prior laboratory results suggest that B/D should increase with KC but this is not always the case (Friedrichs, 2007). The B/D values span the entire parameter space in Figure 6.4b and, hence, the lack of trends between θ and B/D further suggests that probabilistic rather than deterministic models should be used to predict munitions behavior. It is interesting to note that θ values ranged from as small as 0.5 to as large as 20 (Figure 6.4b) suggesting that the forcing on munitions varied widely across the profile and trials.

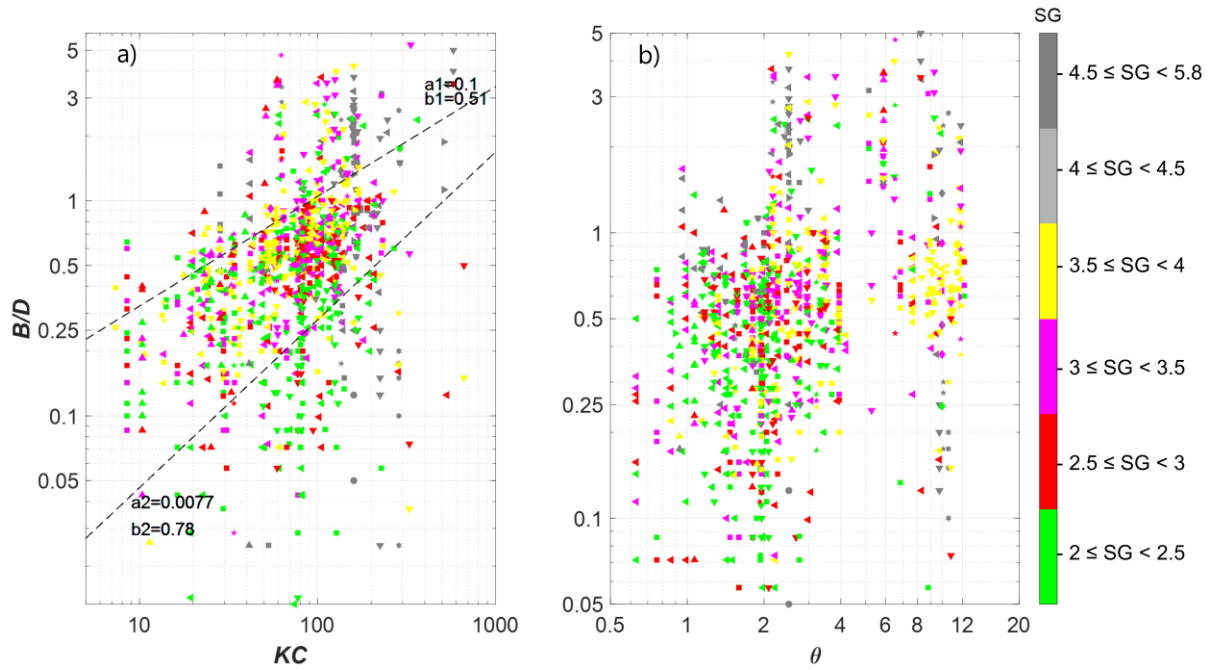


Figure 6.4: Relative burial depth as a function of KC (a) and θ (b).

Attempts were made to create power law relationships between the B/D and the dimensionless numbers KC and θ as demonstrated in previous studies (Cristaudo & Puleo, 2020; Rennie et al., 2017). Individually and collectively, the lack of trends made it impossible to establish any meaningful empirical model.

Chapter 7

DISCUSSION AND CONCLUSION

7.1 Discussion

7.1.1 Migration

Net munitions migration in response to varying hydrodynamics provided aggregated quantification for a wide range of forcing combinations. The 84% “no motion” and 16% “motion” migration observations across the beach profile were subdivided as offshore (94% “no motion”; 6% “motion”), surf zone (80 “no motion”; 20% “motion”), and swash zone (71% “no motion”; 29% “motion”). Previous field studies on munitions mobility in wave-driven and tidal-current-dominated deeper water areas show that most munitions buried and/or remained in place after emplacement (Calantoni et al., 2014; Klammler et al., 2020; Traykovski & Austin, 2017), commensurate with the present study indicating a dominance of no motion. However, when objects migrated, the probability of migration increased towards the shoreline. In the cases where forcing was sufficient for migration, there was a nearly equal chance of onshore or offshore migration in the swash zone, migration in the surf zone tended to be offshore-directed (65%, 157 of 241), while migration was onshore-dominant (65%, 31 of 48) in the offshore zone. The net migration distance varied with the shortest distances observed in the offshore zone and the largest in the surf zone. Similar migration trajectories were found in other studies of munitions migration

where objects in the outer surf zone tended to migrate onshore (Traykovski & Austin, 2017) and those in the swash zone migrated onshore and offshore and were influenced by local slopes (Cristaudo & Puleo, 2020). However, those in the surf zone showed no preferential direction in the study (Cristaudo & Puleo, 2020). The flatter bathymetry and increased depth in the offshore zone may indicate that the wave orbital motion was insufficient to cause the migration of dense munitions. The skewed/asymmetric shape of waves in the intermediate water of the offshore zone coupled with the flat bathymetry may explain why more of the less dense munitions migrated onshore (NAVFAC, 2013). Wave-induced sediment transport, increased wave non-linearity, undertow, and steeper profile slopes in the surf and swash zones may also enhance or hinder munitions migration. The relatively long offshore migration distances in the surf zone may be attributed to the energetic wave shoaling and breaking conditions coupled with steeper slopes.

Swash zone flows are composed of two quasi-unidirectional components: uprush and backwash. Uprush flows originate from bore collapse and may provide enough force to cause onshore motion (against gravity). The munition or object elevation sometimes exceeds the berm elevation and becomes “trapped” in the depression between the berm and the dune. Forcing in this depression was generally not sufficient to cause further migration. In contrast, the munition or object may have migrated a short distance landward during uprush, but the backwash was sufficient (coupled with downslope gravity) to cause offshore migration. The importance of local beach slope to munitions migration was also identified in prior laboratory studies (Cristaudo & Puleo, 2020) and theoretical force balances (Chu, 2023; Cristaudo et al., 2023). The migration of munitions initially located on or close to the berm ($x = 80$ m

and $x = 90$ m) in the swash into the surf zone coincided with the offshore migration of the berm observed in nearly all the cases. The SG of the munitions spanned a wide range, underpinning the dominant role of hydrodynamics and morphodynamics over munitions bulk density in the swash and surf zones. On the other hand, bulk density seemed to dominate over hydrodynamics and morphodynamics (weaker near-bed forcing and flat bathymetry) in the offshore zone.

Across the profile spanning the offshore, surf, and swash zones, munitions bulk density is important for long-distance net migration. In the offshore zone, munitions SG seemed to dominate over hydrodynamics, leading to 94% of munitions not migrating. In the surf zone, 73% of the “no motion” migrations had $SG \geq 3$, implying that there may be an SG threshold separating when munitions in the nearshore migrate or mostly remain in place. The SG threshold for motion/no-motion is likely near $SG = 2.5$, close to the specific gravity of dry sand and matches field observations ($SG < 2$: “motion” and $SG > 3$: “no motion”; Traykovski & Austin, 2017) and prior discussions regarding the importance of SG for migration (Calantoni, 2014; Calantoni et al., 2014). Additionally, the munition relative density $S_m = \rho_m / \rho_s$, where ρ_s is the sediment density, can be used to differentiate between full mobility ($S_m < 1$), partial burial ($S_m \approx 1$), and full burial ($S_m > 1$) (Calantoni, 2018). Similar-shaped S81 ($SG = 4.18$, $S_m = 1.58$) and R81 ($SG = 2.5$, $S_m = 0.94$) deployed in the surf zone (Table 5.5) align with these proposed ranges. At the start of Trial01 of Case02, the S81 ($S_m = 1.58$) initially migrated a short distance of about 3 m offshore within the first 250 s of forcing, and afterward became stationary buried in place. Conversely, a net offshore migration of 33.7 m was observed for the R81 S81 ($S_m = 0.94$) over the forcing duration of Case02 Trial01, with the munition remaining proud. The wide variability

in the migration data (Figure 5.1) spanning the entire range of θ values from 0 to 20 reflects the difficulty associated with representing the stochastic behavior of migration with a deterministic model or dimensionless parameter. Thus, it is believed that a probabilistic model (Palmsten & Penko, 2020) for munitions migration will have better predictive success. For instance, the coupled Delft 3D-UnMES model site demonstration off the coast of a barrier island with an 81 mm mortar of SG 3 produced no migration, 0–5 m migration, and 5 m–50 m migration probabilities of 0.67–0.75, 0.94–0.99, and 0, respectively (Palmsten & Penko, 2020).

7.1.2 Burial

Munitions burial dynamics were governed by local scour (near-field) and far-field morphodynamics. Objects and munitions burial in the offshore zone were largely due to near-field processes owing to the small bed elevation changes. Visual observations when the flume was drained indicated munitions often buried in local scour holes with diameters much larger than the munition diameter. The relative burial depth for near-field processes from prior work tends to be constrained between 0.02 and 2.27 (Cataño-lopera & Marcelo, 2006; Cristaudo & Puleo, 2020; Friedrichs et al., 2018). The slower near-field burial process in this study may explain why B/D in the offshore was generally between 0 and 1. In the surf and swash zones, the burial dynamics were a combination of near- and far-field components; the latter driven by local morphodynamics. In these regions, $\Delta B/D$ was often greater than 2, especially in the surf zone with berm erosion and sand bar formation (Section 4.2). The morphodynamics of surf and swash zones are characterized by sediment transport

gradients (morphodynamics) and bed shear stresses exemplified by estimated θ values of 0.5 to 20. The large θ values imply the potential for enhanced sheet flow conditions (Cristaudo & Puleo, 2020; Lanckriet et al., 2011; Lanckriet & Puleo, 2015; Nielsen & Callaghan, 2003). Active sheet flow coupled with rapid fluid velocities may transport munitions or may allow munitions to become partially or fully buried being carried downward through the sediment slurry.

Simultaneous accretion and munition burials (Figure 6.1; Quadrant I) were the most dominant processes in the swash zone (54%), followed by the surf zone (37%), and lastly the offshore zone (30%). In the swash zone, the impact of bulk density on burial was more obvious as Quadrant I had a higher proportion of buried dense munitions (silver symbols) spanning the parameter space (Figure 6.1c). Attempts made to relate the KC and θ to dimensionless burial or create power law relationships were not successful due to the wide scatter in the dataset (Friedrichs et al., 2018). The present findings are not surprising because, $B/D > 1$ implies a fully buried munition mostly unaffected by direct hydrodynamic action. Hence, KC and θ numbers are unlikely to control the subsequent burial process. Burial Cases with $B/D \gg 1$ (Figures 6.1 and 6.2) must be morphodynamics-driven without an expected relationship to hydrodynamic parameters. Thus, in field settings, predicting munitions burial depth would require knowledge of the initial emplacement condition and time history of hydrodynamic forcing and bed elevation changes.

7.2 Limitations and future work

The wave flume experiment quantified the behavior of munitions and canonical objects in the nearshore in an attempt to make deterministic conclusions.

The controlled nature of the wave flume allowed for the definition of input parameters, easier observation of the complex nearshore processes, and the ability to collect high-resolution data. However, the wave flume is simplified for cross-shore processes even though wave flumes are not exempt from three-dimensionality (Jeon et al., 2018; Kamphuis, 1995). There is always the potential for spatial across-flume (alongshore) variability in wave-driven turbulence and corresponding shear stresses reaching the bed (Yoon & Cox, 2012; Zhou et al., 2017). These variations could lead to misinterpretation of the data from fixed measurements at one location in the alongshore direction. However, natural environments always exhibit three-dimensionality across a wide range of scales and the initial condition of the munition (burial depth, orientation, surface roughness) will never be known. Therefore, it is not anticipated that a deterministic model of munitions migration for the nearshore in a field setting is achievable given the temporal and spatial variability in environmental parameters and the unknown effect that small variations in munitions' initial conditions can have on the munitions response. It is further noted, that munitions' initial conditions are rarely if ever known to the fidelity that would be required for a deterministic model, even in laboratory scenarios. Thus, it is believed that only a probabilistic model for munitions migration (Palmsten & Penko, 2020) would have predictive success.

The study focused on the use of a single sediment type and beach profile. Future large-scale experiments will benefit from the use of different sediment types, and profile types typical of the different beach types in natural environments. For instance, East Coast beaches like Mantoloking beach, New Jersey typically have flatter, sandy profiles with gentler waves while West Coast beaches like San Francisco

beaches have steeper, rockier profiles with more energetic waves due to the different Ocean currents and steeper continental shelf.

7.3 Conclusion

The migration of surrogate munitions and canonical objects was quantified in a large-scale wave flume over a mobile bed. The hydrodynamics consisted of six wave hydrographs of varying wave heights, periods, still water levels, and durations. The cross-shore profile was subdivided into the swash, surf, and offshore zones, where 152 surrogate munitions and canonical objects were deployed. Overall, 2228 migration measurements were recorded. Three instrumented munitions also provided near-instantaneous migration trajectories. Across all zones, 16% and 84% of the migration observations were classified as “motion” (net distance > 0.5 m) and “no motion” (net distance < 0.5 m), respectively. Similarly, the “motion” and “no motion” migration observations in the zones were offshore (6%; 94%), surf (20%; 80%), and swash (29%; 71%). The probability of munitions migration increased with proximity to the shoreline. There was a nearly equal chance of onshore or offshore migration in the swash zone. Migration in the surf zone tended to be off-shore-directed (65%), while migration was onshore-dominant (65%) in the offshore zone.

Bulk density was the more dominant parameter for identifying migration in the off-shore zone than the variations in hydrodynamics, and while the hydrodynamics and local slope were more important for munitions motion in the swash and surf

zones, providing the forcing was sufficient to initiate motion. Bulk density was also found to impact the initiation of motion as inferred from instrumented munitions. Relating overall migration (Lagrangian) to fixed hydrodynamic measurements (Eulerian) was ineffective. Parameters such as the Shields number, object mobility number, wave skewness, and wave asymmetry estimated from the closest measurement location were insufficient to predict deterministically migration due to the observed wide scatter typical of the highly stochastic phenomena. Thus, it is anticipated that deterministic models of migration will struggle to achieve skill given the disparate nature of munitions response even under similar forcing, bulk density, and initial placement characteristics.

The burial dynamics were impacted by munition bulk density and the cross-shore location of the munition. Munitions burial in the offshore zone was governed more by near-field scour processes, while burial in the swash and surf zones resulted from near- and far-field processes. Wide ranges of the Keulegan-Carpenter Number (0 to 1000), and Shields Number (0.5 to 20) were observed suggesting the potential for burial and intense sediment transport. Yet, burial and migration related to these parameters exhibited wide scatter making it impossible to draw empirical relationships with any skill. The wide scatter relates to the numerous and often competing processes leading to burial and migration. It is anticipated that deterministic models of migration and burial will struggle to achieve skill given the disparate nature of munitions response even under similar forcing, bulk density, and initial placement characteristics. The probabilistic approach adopted by this study provided data-driven insights into the likely behavior of munitions in the offshore, surf, and swash regions of the nearshore.

REFERENCES

- Baldock, T. (2019). *Swash Zone Dynamics BT - Encyclopedia of Coastal Science* (C. W. Finkl & C. Makowski, Eds.; pp. 1664–1674). Springer International Publishing. https://doi.org/10.1007/978-3-319-93806-6_404
- Battjes, J. A. (1988). SURF-ZONE DYNAMICS. *Ann. Rev. Fluid Mech.*, 20(1), 257–293. www.annualreviews.org.
- Bosboom, J., & Stive, M. J. F. (2021). *Coastal Dynamics* (Revision n). Delft University of Technology. <https://doi.org/10.5074/T.2021.001>
- Bralower, T., Cornell, S., Fitzgerald, D., Frey, N., Georgiou, I., Hanegan, K. C., Hung, L.-S., Kulp, M., Maygarden, D., Retchless, D., & Yarnal, B. (2021). *Coastal Processes, Hazards, and Society*. The Pennsylvania State University.
- Breslin, S. (2017). *Ordnance Found Washed Up on Outer Banks Beaches as Hurricane Maria Churns Up Sea*. The Weather Channel. <https://weather.com/news/news/outer-banks-beaches-ordnance-found-north-carolina>
- Bruder, B., Cristaudo, D., & Puleo, J. A. (2018). Smart Surrogate Munitions for Nearshore Unexploded Ordnance Mobility / Burial Studies. *IEEE JOURNAL OF OCEANIC ENGINEERING*, 45(1), 1–20. <https://doi.org/10.1109/JOE.2018.2871227>
- Calantoni, J. (2014). *Informal Workshop on Burial and Mobility Modeling of Munitions in the Underwater Environment* (Issue OMB No. 0704-0188). <https://apps.dtic.mil/dtic/tr/fulltext/u2/a627132.pdf>
- Calantoni, J. (2018). *Long Time Series Measurements of Munitions Mobility in the Wave-Current Boundary Layer SERDP Project Number 2320*. National Association of Ordnance Contractors. https://www.naoc.org/_cache/files/b/f/bf9ce668-450c-4abe-85b8-f4d3e424980b/F4E8E00F76C5FE0661B1923B1DDFB4EB.mr-2320-calantoni.pdf
- Calantoni, J., Staples, T., & Sheremet, A. (2014). *Long Time Series Measurements of Munitions Mobility in the Wave-Current Boundary Layer SERDP Project*

Number 2320 Joseph Calantoni REPORT NUMBER (Issue MR2320 Interim Report).

- Carton, G., & Jagusiewicz, A. (2009). Historic Disposal of Munitions in U.S. and European Coastal Waters, How Historic Information Can be Used in Characterizing and Managing Risk. *Marine Technology Society Journal*, 43(4), 16–32.
- Cataño-Lopera, Y. A., Demir, S. T., & García, M. H. (2007). Self-burial of short cylinders under oscillatory flows and combined waves plus currents. *IEEE Journal of Oceanic Engineering*, 32(1), 191–203.
<https://doi.org/10.1109/JOE.2007.890968>
- Cataño-lopera, Y. A., & García, M. H. (2006). Burial of Short Cylinders Induced by Scour under Combined Waves and Currents. *Journal of Waterway, Port, Coastal, and Ocean Engineering*, 132(6), 439–450. <https://doi.org/10.1061/ASCE0733-950X2006132:6439>
- Cataño-Lopera, Y. A., & García, M. H. (2007). Geometry of scour hole around, and the influence of the angle of attack on the burial of finite cylinders under combined flows. *Ocean Engineering*, 34(5–6), 856–869.
<https://doi.org/10.1016/j.oceaneng.2006.05.001>
- Cataño-Lopera, Y. A., Landry, B. J., & García, M. H. (2011). Scour and burial mechanics of conical frustums on a sandy bed under combined flow conditions. *Ocean Engineering*, 38(10), 1256–1268.
<https://doi.org/10.1016/j.oceaneng.2011.05.007>
- Chakrabarti, S. K. (1998). Wave forces on offshore structures. In J. B. Herbich (Ed.), *Handbook of coastal and ocean engineering: Vol. Volume 2* (pp. 1–1125). Gulf Publishing Company.
- Chardón-maldonado, P., Pintado-patiño, J. C., & Puleo, J. A. (2016). Advances in swash-zone research : Small-scale hydrodynamic and sediment transport processes. *Coastal Engineering*, 115, 8–25.
<https://doi.org/10.1016/j.coastaleng.2015.10.008>
- Chu, P. C. (2023). *Coupled Ensemble Seafloor Environment and 6-DOF (CESE6D) Model for Assessing Characteristics of Munitions Underwater and Their Environment*. <https://serdp-estcp.mil/projects/details/c3647185-a430-4096-8e01-a591fa5cb368/mr19-1073-project-overview>
- CNS Systems. (2024). *Tac32 Software for the CNS Clock and the CNS Clock II*. CNS Systems. <https://www.cnssys.com/cnsclock/Tac32Software.php>

- Cristaudo, D., Gross, B. M., & Puleo, J. A. (2023). Momentum Balance Analysis of Spherical Objects and Long-Term Field Observations of Unexploded Ordnance (UXO) in the Swash Zone. *Journal of Marine Science and Engineering*, 11(1). <https://doi.org/10.3390/jmse11010079>
- Cristaudo, D., & Puleo, J. A. (2020). Observation of munitions migration and burial in the swash and breaker zones. *Ocean Engineering*, 205. <https://doi.org/10.1016/j.oceaneng.2020.107322>
- Crosby, B., & Whipple, K. (2004). Essentials of Sediment Transport. In *In Surface Processes and Landscape Evolution. Fall 2004. Massachusetts Institute of Technology: MIT OpenCourseWare*. Massachusetts Institute of Technology.
- Dean, R. G., & Dalrymple, R. A. (2010). *Coastal Processes with Engineering Applications*. Cambridge University Press. <https://doi.org/10.1017/CBO9780511754500>
- Demir, S. T., & García, M. H. (2007). Experimental Studies on Burial of Finite-Length Cylinders under Oscillatory Flow. *Journal of Waterway, Port, Coastal, and Ocean Engineering*, 133(2). <https://doi.org/10.1061/ASCE0733-950X2007133:2117>
- Edwards, C. A. (2001). Grain Size and Sorting in Modern Beach Sands. In *Source: Journal of Coastal Research* (Vol. 17, Issue 1). Winter.
- Elfrink, B., & Baldock, T. (2002). Hydrodynamics and sediment transport in the swash zone : a review and perspectives. *Coastal Engineering*, 45, 149–167. [https://doi.org/10.1016/S0378-3839\(02\)00032-7](https://doi.org/10.1016/S0378-3839(02)00032-7)
- Elgar, S., & Guza, R. T. (1986). Nonlinear model predictions of bispectra of shoaling surface gravity waves. *J. Fluid Mech.*, 167, 1–18.
- Frank, D., Landry, B. J., & Calantoni, J. (2016). *Investigating Munitions Mobility in Oscillatory Flows with Inertial Measurement Units*. <https://doi.org/10.1109/OCEANS.2016.7761158>
- Friedrichs, C. T. (2007). *Reformulation of mine scour equations using observations from MBP field sites*.
- Friedrichs, C. T., Rennie, S. E., & Brandt, A. (2016). Self-burial of objects on sandy beds by scour: A synthesis of observations. *Scour and Erosion - Proceedings of the 8th International Conference on Scour and Erosion, ICSE 2016*, 179–189. <https://doi.org/10.1201/9781315375045-23>

- Friedrichs, C. T., Rennie, S. E., Brandt, A., & Sarah, E. (2018). Simple Parameterized Models for Predicting Mobility , Burial and re-exposure of underwater munitions . SERDP Final Report. *SERDP Final Report MR-2224. Virginia Institute of Marine Science, William & Mary*. <https://doi.org/10.25773/gk95-bb88>
- Garcia, M. H., & Landry, B. J. (2018). *Large-Scale Laboratory Experiments of Incipient Motion, Transport, and Fate of Underwater Munitions under Waves, Currents, and Combined-Flows.*
- Geib, C. (2018). *Tracking Unexploded Munitions Long-buried ordnance lingers on U.S. coasts.* Woods Hole Oceanographic Institution.
<https://www.whoi.edu/oceanus/feature/tracking-uxos/>
- Grasso, F., Michallet, H., Barthélémy, E., & Certain, R. (2009). Physical modeling of intermediate cross-shore beach morphology: Transients and equilibrium states. *Journal of Geophysical Research: Oceans*, 114(9), 1–15.
<https://doi.org/10.1029/2009JC005308>
- Gross, B. M. (2019). *MOBILITY OF UNEXPLODED ORDNANCE USING SPHERICAL SURROGATES IN THE SWASH ZONE.*
- Hsu, T.-J., Tsai, B., Tarazouj, A. S., Chauchat, J., Montella, E. P., & Bonamy, C. (2020). *Novel Eulerian Two-phase Simulations for Burial Dynamics of Munitions Phase I.*
- Hughes, M. G., & Turner, I. (1999). The beach face. . In A. D. Short (Ed.), *Handbook of Beach and Shoreface Morphodynamics* (pp. 119–144). Wiley.
- Hughes, S. A. (1984). *The TMA shallow-water spectrum description and applications (CERC-84-7).*
- Idowu, T., Gangadharan, M., Chapman, E., Stolle, J., Pham van Bang, D., & Puleo, J. (2022). *BEHAVIOR OF VARIABLE DENSITY MUNITIONS UNDER DAM BREAK FORCING.* <https://doi.org/10.9753/icce.v37.management.123>
- Jeon, J., Lee, J. Y., & Kang, S. (2018). Experimental Investigation of Three-Dimensional Flow Structure and Turbulent Flow.pdf. *Water Resources Research*, 54, 3530–3556. <https://doi.org/10.1029/2017WR021582>
- Kamphuis, W. (1995). Comparison of Two-Dimensional and Three-Dimensional Beach Profiles. *Journal of Waterway, Port, Coastal, and Ocean Engineering*, 121(June), 155–161.

- Klammler, H., Shemet, A., & Calantoni, J. (2020). Seafloor Burial of Surrogate Unexploded Ordnance by Wave-Induced Sediment Instability. *IEEE Journal of Oceanic Engineering*, 45(3), 927–936.
<https://doi.org/10.1109/JOE.2019.2919356>
- Komar, P. D. (1998). *Beach Processes and Sedimentation* (R. A. McConnin, Ed.; Second). Prentice Hall.
- Laksanalamai, J., & Kobayashi, N. (2023). Tracking of Small Discrete Objects Submerged in Surf and Swash Zones on Sand Beaches. *Journal of Waterway, Port, Coastal, and Ocean Engineering*, 149(6).
<https://doi.org/10.1061/jwped5.wweng-1987>
- LHE. (2021). *Large scale wave flume*. Laboratoire d'Hydraulique Environnementale (LHE) Est Un Laboratoire de l'Institut d'Ingénierie Civile (IIC) de La Faculté Environnement Naturel, Architectural et Construit (ENAC).
https://lhe.ete.inrs.ca/wp-content/uploads/2020/04/LHE_Flyer_2020.pdf
- LHE-INRS. (2024). *LHE overview*. LHE INRS Centre Eau Terre Environnement.
<https://lhe.ete.inrs.ca/about/>
- Liu, X., & Qiu, T. (2019). *INTERIM REPORT Three-dimensional Computational Modeling of Turbulent Flow Field, Bed Morphodynamics and Liquefaction Adjacent to Munitions*. <https://apps.dtic.mil/sti/trecms/pdf/AD1169169.pdf>
- Luccio, P. A., Voropayev, S. I., Fernando, H. J. S., Boyer, D. L., & Houston, W. N. (1998). The motion of cobbles in the swash zone on an impermeable slope. *Coastal Engineering*, 33(1), 41–60. [https://doi.org/10.1016/S0378-3839\(98\)00003-9](https://doi.org/10.1016/S0378-3839(98)00003-9)
- Macdonald, J., Knopman, D., Lockwood, J. R., Cecchine, G., & Willis, H. (2004). *Ordnance: A Critical Review of Risk Assessment Methods (No. MR-1674)*.
- Masselink, G., & Puleo, J. A. (2006). Swash-zone morphodynamics. *Continental Shelf Research*, 26, 661–680. <https://doi.org/10.1016/j.csr.2006.01.015>
- NAVFAC. (2013). *Hydrodynamic mobility analysis of UXO Transport Andrew Bay Adak, Alaska*. Department of Navy.
- Nielsen, P. (2009). *Coastal and estuarine processes* (Vol. 29). World Scientific Publishing Company.
- NOAA. (2019). *WAVEWATCH III Development*. National Oceanic and Atmospheric Administration. https://www.weather.gov/sti/coastalact_ww3

- Nortek. (2024a). *Vector - 4000 m*. Nortek.
- Nortek. (2024b). *Vectrino Profiler*. Nortek.
- Osborne, P. D. (2019). Cross-Shore Variation of Grain Size on Beaches. In C. W. Finkl & C. Makowski (Eds.), *Encyclopedia of Coastal Science* (pp. 666–672). Springer International Publishing. https://doi.org/10.1007/978-3-319-93806-6_105
- Palmsten, M. L., & Penko, A. M. (2020). *Probabilistic Environmental Modeling System for Munitions Mobility SERDP Project Number MR-2733* (Issue September). <https://apps.dtic.mil/sti/pdfs/AD1173678.pdf>
- Parry, W. (2018). *A century after WWI, munitions still making way onto beaches*. AP NEWS. <https://apnews.com/article/cca295bd3bb547ec96b79c561c134ff0>
- Penko, A. (2021). *Munitions Response Library for Site Management*. SERDP MR21-5207. <https://serdp-estcp.mil/projects/details/fc62c019-c1de-46f5-9542-5a1d785fc910/mr21-5207-project-overview>
- Pontiki, M., Puleo, J. A., Bond, H., Wengrove, M., Feagin, R. A., Hsu, T. J., & Huff, T. (2023). Geomorphic Response of a Coastal Berm to Storm Surge and the Importance of Sheet Flow Dynamics. *Journal of Geophysical Research: Earth Surface*, 128(10). <https://doi.org/10.1029/2022JF006948>
- Pratt, W. K. (1991). *Digital Image Processing*. John Wiley & Sons.
- Puleo, J. A., & Calantoni, J. (2023). *SERDP Workshop on UXO Mobility, Burial, and Exposure Processes: Discussion for a Demonstration Project*. <https://apps.dtic.mil/sti/citations/trecms/AD1209608>
- Puleo, J. A., & Cristaudo, D. (2020). Quantification of Hydrodynamic Forcing and Burial, Exposure and Mobility of Munitions on the Beach Face SERDP Project MR-2503. In *Strategic Environmental Research and Development Program (SERDP): Vol. MR-2503*.
- Puleo, J. A., Holland, K. T., Slinn, D. N., Smith, E., & Webb, B. M. (2003). NUMERICAL MODELLING OF SWASH ZONE HYDRODYNAMICS. In *Coastal Engineering 2002* (pp. 968–979). WORLD SCIENTIFIC. https://doi.org/doi:10.1142/9789812791306_0082
- Puleo, J., Beach, R. A., Holman, R. A., & Allen, J. S. (2000). Swash zone sediment suspension and transport and the importance of bore-generated turbulence. *Journal of Geophysical Research*, 105, 17021–17044.

- Randall, K. (2015, August 3). *A Real Ticking Time Bomb Recent reports of unexploded bombs and other military ordnance washing up on the Florida coast could pose serious threats*. Texas A&M Today. <https://shorturl.at/aqxD6>
- Rennie, S. (2017). *Underwater Munitions Expert System to Predict Mobility and Burial* (Issue (MR-2227)).
- Rennie, S., Brandt, A., & Ligo, J. G. (2019). *Underwater Munitions Expert System for Remediation Guidance Prototype Underwater Munitions Expert System: Demonstration and User Guide*.
- Rennie, S. E., Brandt, A., & Friedrichs, C. T. (2017). Initiation of motion and scour burial of objects underwater. *Ocean Engineering*, 131(March 2016), 282–294. <https://doi.org/10.1016/j.oceaneng.2016.12.029>
- SedExpNet. (2024). *Acoustic Doppler Velocimeter (ADV)*. Sediment Experimentalists Network.
- SERDP. (2010). *Munitions in the Underwater Environment : State of the Science and Knowledge Gaps* (Issue June). <https://apps.dtic.mil/sti/citations/ADA571686>
- Sumer, B. M., & Fredsøe, J. (2001). SCOUR AROUND PILE IN COMBINED WAVES AND CURRENT. In *JOURNAL OF HYDRAULIC ENGINEERING*.
- Sumer, B. M., & Fredsoe, J. (2002). *The Mechanics of Scour in the Marine Environment* (Adv. S. on Ocean Eng, Vol. 17). World Scientific Publishing Company. [https://doi.org/https://doi.org/10.1142/4942](https://doi.org/10.1142/4942)
- Sumer, B. M., Truelsen, C., Sichmann, T., & Fredsøe, J. (2001). Onset of scour below pipelines and self-burial. In *Coastal Engineering* (Vol. 42). www.elsevier.comrlocatercoastaleng
- Svendsen, I. A., Madsen, P. A., & Hansen, J. B. (1978). WAVE CHARACTERISTICS IN THE SURF ZONE. *Proceedings of the 16th Conference on Coastal Engineering*, Pp. 520 – 539.
- Traykovski, P., & Austin, T. (2017). *Continuous Monitoring of Mobility, Burial and Re-exposure of Underwater Munitions in Energetic Near-Shore Environments* (Issue SERDP Project MR-2319). <https://apps.dtic.mil/sti/pdfs/AD1029969.pdf>
- Traykovski, P., & Jaffre, F. (2020). *FINAL REPORT Rapid Response Surveys of Mobility, Burial and Re-exposure of Underwater Munitions in Energetic Surf-Zone Environments and Object Monitoring Technology Development Distribution Statement A*.

- Trimble Geospatial. (2024). *Trimble S5 Total Station*. Trimble Geospatial.
https://trl.trimble.com/docushare/dsweb/Get/Document-751932/022516-153H_TrimbleS5_Specsheet_USL_0524_LR_SEC.pdf
- Tsai, B., Hsu, T., Lee, S., Pontiki, M., Puleo, J. A., & Wengrove, M. E. (2024). Large Eddy Simulation of Cross-Shore Hydrodynamics Under Random Waves in the Inner Surf and Swash Zones. *Journal of Geophysical Research: Oceans*, 129(9). <https://doi.org/10.1029/2024JC021194>
- US Army RDECOM. (2001). *Off-shore disposal of chemical agents and weapons conducted by the United States*.
- USACE. (2003). Chapter II-4. Surf Zone Hydrodynamics. In *Coastal Engineering Manual: Vol. (Part II)* (EM 1110-2-1100). US Army Corps of Engineers.
- Valeport. (2024). *MODEL 802 - Electromagnetic Current Flow Sensors*. Valeport.
- Van Rijn, L. C., Tonnon, P. K., Sánchez-Arcilla, A., Cáceres, I., & Grüne, J. (2011). Scaling laws for beach and dune erosion processes. *Coastal Engineering*, 58(7), 623–636. <https://doi.org/10.1016/j.coastaleng.2011.01.008>
- Voropayev, S. I., Testik, F. Y., Fernando, H. J. S., & Boyer, D. L. (2003a). Burial and scour around short cylinder under progressive shoaling waves. *Ocean Engineering*, 30(13), 1647–1667. [https://doi.org/10.1016/S0029-8018\(02\)00146-4](https://doi.org/10.1016/S0029-8018(02)00146-4)
- Voropayev, S. I., Testik, F. Y., Fernando, H. J. S., & Boyer, D. L. (2003b). Morphodynamics and cobbles behavior in and near the surf zone. *Ocean Engineering*, 30(14), 1741–1764. [https://doi.org/10.1016/S0029-8018\(03\)00013-1](https://doi.org/10.1016/S0029-8018(03)00013-1)
- Wengrove, M., & Garcia-Medina, G. (2022). *Munition Mobility in Mixed Grain (Sand, Gravel, Cobble) Environments*. <https://serdp-estcp.mil/projects/details/b1a86abb-8542-484b-bf70-8f131462e6e2/mr21-1333-project-overview#:~:text=Results,likely%20due%20to%20bed%20friction>.
- Wilkinson, I. (2017). *Chemical Weapon Munitions Dumped at Sea: An Interactive Map*. James Martin Center for Nonproliferation Studies, Monterey, CA 93940 USA. <https://nonproliferation.org/chemical-weapon-munitions-dumped-at-sea/>
- Wright, L. D., & Short, A. D. (1984). Morphodynamic variability of surf zones and beaches: a synthesis. *Marine Geology*, 56(1–4), 93–118.

WW3DG. (2016). *User manual and system documentation of WAVEWATCH III® version 5.16.Tech. Note 329*, NOAA/NWS/NCEP/MMAB. The WAVEWATCH III® Development Group.
<https://polar.ncep.noaa.gov/waves/wavewatch/manual.v5.16.pdf>

Yoon, H. D., & Cox, D. T. (2012). Cross-shore variation of intermittent sediment suspension and turbulence induced by depth-limited wave breaking. *Continental Shelf Research*, 47, 93–106. <https://doi.org/10.1016/j.csr.2012.07.001>

Zhou, Z., Hsu, T.-J., Cox, D., & Liu, X. (2017). Large-eddy simulation of wave-breaking induced turbulent coherent structures and suspended sediment transport on a barred beach. *J. Geophys. Res. Oceans*, 122, 207–235.
<https://doi.org/10.1002/2016JC011884>

Appendix A

DESCRIPTION OF TERMS IN THE AGGREGATED MUNITIONS TABLE

The column descriptions in the order of their appearance in the Munitions Table.

No	Column titles	Description	Symbol	Unit
1	'Munitions'	154 munitions were deployed at the start of the experiment. NB. Some munitions were undetectable due to excessive burial during the experiment.	See deployment	
2	'Location'	Zone munition is located e.g. offshore, surf, swash		
3	'SpecificGravity'	The ratio of the bulk density of the object to that of water	SG	-
4	'BulkDensity'	Mass per unit bulk volume of the munition	BD	kg/m ³
5	'Orientation'	Orientation of the munition with respect to fluid flow. E.g. Spanwise or Streamwise or NA. Streamwise – Munition is oriented parallel to fluid flow Spanwise – Munition is oriented perpendicular to the flow NA – For spherical munitions and BLUs		
6	'MunX'	Cross-shore position (<i>x</i>) of munition before a trial. In some Cases where data were not taken until two trials later after the flume was drained, the last known location was used.		'm'
7	'MunZ'	Vertical position (<i>z</i>) of the munition at MunX		'm'
8	'Diameter'	The cross-sectional diameter of the munition	D	'm'
9	'Length'	The length of the munition	L	'm'
10	'h'	Water depth at the location of the munition at MunX		'm'
11	'LocBefore'	Last known location of a munition before a trial		'm'
12	'Loc_lastT'	Location of a munition at the last trial before the current trial. 'Loc_lastT' = 'LocBefore' when munitions location data were taken in the prior trial.		'm'
13	'LocAfter'	Location of a munition after a trial		'm'
14	'ProfileChange'	Profile elevation after a trial minus the pretrial profile at a munition's location MunX		'm'
15	'ProfileChangeDim'	Relative profile change = Profile change / munition diameter		-
16	'Migration'	Location after – LocBefore		'm'
17	'Migration_T2T'	LocAfter – Loc_lastT		'm'
18	'Cum_Migration'	LocAfter – Initial location of munition before the start of the experiment.		'm'
19	'Burial_Initial'	Initial burial status of munition before the start of the experiment. Typically 0 for proud munitions		'm'
20	'Burial_lastT'	Burial status of munition after the prior trial		'm'
21	'Burial_Final'	Burial status of munition after a trial. -ve because		'm'
22	'DimBurial'	(-1) x Burial_Final / Munition Diameter (Normalized burial depth.)		
23	'BurialDepthChange'	(Burial_Final - Burial_lastT) x (-1)	B	'm'
24	'BurialDepthChange_Ratio'	BurialDepthChange / Munition Diameter	B/D	-

25	'Cum_BurialDepthChange_Ratio'	Burial_Final – Initial burial at the start of the Case		'_'
26	'waveheight'	Offshore wave height for generating the wave spectrum		'm'
27	'Duration'	Duration of the wave spectrum based on 300 waves		's'
28	'waveperiod'	Offshore wave period for generating the wave spectrum		's'
29	'NearestUDM'	Location of closest UDM sensor		
30	'UDMDistance'	Distance between a munition and the closest UDM sensor		'm'
31	'UDMStddev'	Standard deviation of the UDM time series value		'm'
32	'Hydrostation'	Station from which velocity data were taken		
33	'HydroDistance'	Distance between a munition and the closest hydrodynamic sensor		'm'
34	'Urms'	Root mean square velocity		'm/s'
35	'UrmsOnshore'	Root mean square velocity of the onshore-directed portion of the waves		'm/s'
36	'UrmsOffshore'	Root mean square velocity of the offshore-directed portion of the waves		'm/s'
37	'U2percent'	The 2 percent exceedance of the velocity time series		'm/s'
38	'Uonshore2p'	The 2 percent exceedance for the onshore-directed portion of the velocity time series		'm/s'
39	'Uoffshore2p'	The two percent exceedance for the offshore-directed portion of the velocity time series		'm/s'
40	'U_meantotal'	Mean of the velocity of the velocity time series		'm/s'
41	'U_meanwet'	Mean of the velocity time series when the ground was wet (changes for swash zone or where there is intermittent wetting and drying due to waves)		'm/s'
42	'Hrms'	The root mean square wave height based on the UDM data at each station		'm'
43	'Hs'	The top 1/3 of the wave height based on the UDM data at each station		'm'
44	'KCnumberU2p'	The KC number using Eq.1 where U is the U2percent		
45	'KCnumberOnshore'	The KC number using Eq.1 where U is the Uonshore2p		
46	'KCnumberOffshore'	The KC number using Eq.1 where U is the UOffshore2p		
47	'KCnumberUmeanwet'	The KC number using Eq.1 where U is the U_meanwet		
48	'ObjectMobilityNo_U2p'	The θ_m using Eq.2 where U is the U2percent		
49	'ObjectMobilityNo_Onshore'	The θ_m number using Eq.2 where U is the Uonshore2p		
50	'ObjectMobilityNo_Offshore'	The θ_m number using Eq.2 where U is the UOffshore2p		
51	'ObjectMobilityNo_Umeanwet'	The θ_m number using Eq.2 where U is the U_meanwet		
52	'Tao_b_U2p'	The bed shear stress τ_b where U is the U2percent		'N/m ² '
53	'Tao_b_UOnshore2p'	The bed shear stress τ_b where U is the Uonshore2p		'N/m ² '
54	'Tao_b_UOffshore2p'	The bed shear stress τ_b where U is the UOffshore2p		'N/m ² '
55	'Tao_b_Urms'	The bed shear stress τ_b where U is the Urms		'N/m ² '
56	'Tao_b_Umeanwet'	The bed shear stress τ_b where U is the U_meanwet		'N/m ² '
57	'ShieldsU2p'	The θ using Eq.3 where U is the U2percent		
58	'ShieldsUOnshore2p'	The θ number using Eq.3 where U is the Uonshore2p		
59	'ShieldsUOffshore2p'	The θ number using Eq.3 where U is the UOffshore2p		
60	'ShieldsUrms'	The θ number using Eq.3 where U is the Urms		
61	'ShieldsUmeanwet'	The θ number using Eq.3 where U is the U_meanwet		

ProQuest Number: 31770280

INFORMATION TO ALL USERS

The quality and completeness of this reproduction is dependent on the quality
and completeness of the copy made available to ProQuest.



Distributed by

ProQuest LLC a part of Clarivate (2025).

Copyright of the Dissertation is held by the Author unless otherwise noted.

This work is protected against unauthorized copying under Title 17,
United States Code and other applicable copyright laws.

This work may be used in accordance with the terms of the Creative Commons license
or other rights statement, as indicated in the copyright statement or in the metadata
associated with this work. Unless otherwise specified in the copyright statement
or the metadata, all rights are reserved by the copyright holder.

ProQuest LLC
789 East Eisenhower Parkway
Ann Arbor, MI 48108 USA